PHOTONIC STRUCTURES AND DEVICES MOLDED ON SOFT POLYMER MATERIALS

Cary Aaron Tippets

A dissertation submitted to the faculty of the University of North Carolina at Chapel Hill in partial fulfillment of the requirements for the degree of Doctor of Philosophy in the Department of Applied Physical Sciences in the College of Arts and Sciences.

Chapel Hill
2017

Approved by:

Rene Lopez

Edward Samulski

Michael Falvo

Daphne Klosta

Sergei Sheiko

ABSTRACT

Cary Aaron Tippets: Biomimetic Structures and Shape Active Polymers
(Under the direction of Rene Lopez)

Polymer materials are ubiquitous, relatively cheap, easy to process, and functionalize, making them interesting for many applications, in particular for optical systems that are traditionally fabricated from rigid and expensive materials. Polymer properties can be exploited to modulate the optical response of photonic structures. In this dissertation, I will discuss the fabrication and demonstration of several applications of soft polymers in the field of optics. Soft polymers can be used to fabricate structures with optical effects inaccessible using a single optical element created from standard materials. First, I employed a biomimetic approach to produce structural color similar to the bright blue of the Morpho Butterfly. Second, I used shape active polymers to reversibly modulate the height of an optical grating through heat. Lastly, I developed a varifocal polymer lens for an augmented reality system.

Structural Color, as opposed to pigmented color, is the result of light interacting with structures with geometrical length scales comparable with the wavelength of visible light. There are many examples of structural color found in nature, from the various colors of the jewel beetles to the vibrant blue of the kingfisher bird. This structural effect can typically be identified by the iridescent nature of the coloration. I will discuss my approach toward biomimicry of the unique photonic structure found on the surface of the Morpho butterfly wings. This sub-micron sized structure is a ridge which in cross-sectional view resembles a tree, with a thin "trunk" and

many periodic "branches" that produce a multilayer interference effect, strongly reflecting a brilliant blue color over a wide angular range.

Biomimicry of the Morpho butterfly nanostructure has been attempted but the angular insensitivity has never been fully shown in a man-made replica. I will discuss the importance of the inherent randomness found within the Morpho structures that causes light to spread over such a large range. Here in, I will show two different fabrication approaches to integrate microstructure randomness and the consequence of such variations on the angular response. In structures that were fabricated using interference lithography a quasi-randomness (incomplete randomization) is induced through drying. Angular measurements show that a two-lobe reflection, much alike that produced by the true butterfly wing, is produced in angular space and is attributable to this quasi-random nanostructure. However, periodicity needs to be fully destroyed in order to overcome diffraction. To do this a direct-write lithography system was built and used to produce completely non-periodic structures. The results showed a more pronounced a two-lobe reflection at oblique angles. Finite-difference time-domain (FDTD) simulations were employed to understand this reflection signature and to determine effect of other geometric features. From these simulations a photonic structure, capable of spreading light in similar fashion to the butterfly, and that can be fabricated with standard microfabrication techniques is proposed.

In connection to the use of polymers in diffractive structures, I will discuss my work with shape active polymers. Shape memory polymers offer a unique approach for application that demand multipurpose parts and have been utilized as heart stents and actuators. The applicability of these shape memory polymers as optical elements is demonstrated by examining the optical response of a shape shifting diffraction grating. As the height of the diffraction grating is

reversibly changed the intensity of diffracted light is modulated. This constitutes a simple device realization that nevertheless illustrates the materials and optical issues that arise from the application of shape memory polymer in more complex photonic shapes will lead to the optical systems with versatile components.

Finally, the use of elastomeric polymers as shape active lens will be explored. Varifocal lenses have shown the potential to solve an inherent problem in virtual and augmented reality headsets. In augmented and virtual reality headsets, the human eye will focus on the screen several inches from the face but images for both eyes are off set in order cause the users eyes to converge at a certain angle, imitating distance. In the real-world focus and vergence are in sync but these headsets encounter what is known as vergence–accommodation conflict and it is the source of major user discomfort. Vergence–accommodation conflict prevents the wide spread adoption of these potentially impactful technologies. I will present my work in developing a varifocal half silvered mirror for use in an augmented reality system. The system was validated by a perception test that showed users having increased success when the system was properly focused

To Carla, Thanks for walking to the end of the road with me.

Now let's play some games.

system up and running. Your ability to focus a laser still amazes me. You are a fantastic scientist and I wish you the best in your graduate work.

Finally, I would like to thank my family, without your support I would have never made it through this crazy endeavor. To my parents who literally never let a week pass without telling me "the only good PhD is a done PhD", for 6 years…Thanks for the encouragement and you were right the whole time. To my children who deprived me of sleep but lit up every single day for me, helping me to keep life in perspective. And to my wife, Carla, you are my rock and my favorite person. Thanks for supporting me and helping me to stay the course.

TABLE OF CONTENTS

LIST OF FIGURES

LIST OF ABBREVIATIONS AND SYMBOLS

1D	1 dimensional
2D	2 dimensional
3D	3 dimensional
AFM	Atomic force microscopy
AR	augmented reality
CVD	chemical vapor deposition
DMA	Dynamic mechanical analysis
DSC	Differential Scanning Calorimetry
Ebeam	electron beam lithography
FDTD	finite difference time domain
FOV	field of view
NED	near eye display
LPCVD	low pressure chemical vapor deposition
IL	Interference lithography
M. *rhetenor*	Morpho rhetenor
Nm	nanometer
PDMS	Polydimethylsiloxane
PET	Polyethylene terephthalate
PECVD	plasma enhanced chemical vapor deposition
PFPE	perfluoropolyether
POA	polyoctylene adipate
RSM	reversible shape memory
SEM	scanning electron microscope
SMP	Shape memory polymer
T_m	melting temperature
T_p	Partial melting temperature
VAC	vergence-accommodation conflict

VR	virtual reality
θ	Incident angle
ϕ	reflected or scattered angle
δ	height of grating
λ	wavelength

Chapter 1

Introduction

1.1 Introduction

Polymers have already found their way into a multitude of technological areas and have the potential to increase the functionality of a great variety of components. Soft polymers in particular could add useful functionality to optical systems by allowing control of the optical response. Standard optical elements are typically crafted from hard materials, while these faithfully serve a single purpose, multi-functional polymer optics that could provide cheap, replicable, and on demand photonic structures. I will discuss the application of soft polymers in order to access or enhance an optical response, and how this can be used in widely different areas (or for different purposes). The first part of this dissertation focuses on structural colors inspired by the Morpho butterfly wing structure. I will review various photonic biological models found in nature, in terms of their unique nanostructures that are the sources of their remarkably brilliant colors. In particular, I will discuss the Morpho *rhetenor* butterfly. Secondly, I will present a brief discussion on shape memory effects in materials, with particular emphasis in the shape memory effect that arises from polymers. Shape memory polymers offer a simple manner by which to manipulate photonic shapes, thus controlling the optical response.

Finally, I will discuss a fundamental limitation in current augmented reality headsets, which produces a mismatch in the human visual system. This limitation, along with several others, can be address by the use of elastomeric polymer lenses Therefore, in the following sections of this introductory chapter, I address the background of each of the components of this three-pronged dissertation on applications of soft polymers in optical structures.

1.2 Biomimicry: Structural color and taking inspiration from nature

Biomimicry is the process by which methods and designs from nature are replicated or used as inspiration to solve complex real world problems. Scientist often seek to replicate the natural model and then improve upon it. Classic examples of biomimicry, such as the supposed story of how the Wright brother took inspiration from pigeons to develop their flight machine [1] or more recently on the development of Velcro, which was inspired by the surface of burrs [2], illustrate the impact biomimicry can have on the innovative process. A peculiar occurrence in nature is that of structural color, displayed on a variety of animals and plant spices, it is characteristically vibrant and exhibits several other unique optical attributes. These optical properties could be exploited and make it an attractive target for biomimicry. However, it should be noted that biomimicry of these optical properties requires that the structures responsible for these phenomena be crafted from a material, or materials, with a single refractive index (or a system that can be approximated as such). Fabricating such structures from hard materials has been done using natural templates, but soft polymers provide the opportunity to use different fabrication routes, while satisfying the optical requirements.

1.2.1 Structural Color in Nature

Scientists fascination with structural color reaches back to the inception of the study of optics, when Robert Hooke and Sir Isaac Newton studied the coloration of the peacock feather and observed that the reflected light is" tinged… in a most curious manner". [3,4] Within the last several decades scientists have become increasingly interested in understanding and explaining the source of structural color exhibited by different animals, insects and plants.[5–8] Structural color in nature can often be identified by a strong metallic or iridescent appearance. Structural color, as opposed to pigmented color, is the result of nanostructures found on the biological surface, which interfere with the incident light and reflects only a specific limited range of electromagnetic wavelengths. The simplest example of structural color is thin film interference, when an incident light is reflected by each boundary of the film. The thickness of the thin film will dictate the wavelength of light that undergoes constructive interference when reflected. This in effect gives the perception of color when light is incident on the film. Everyday examples of this can be seen on the surface of a bubble or oil spreading out over the surface of water.
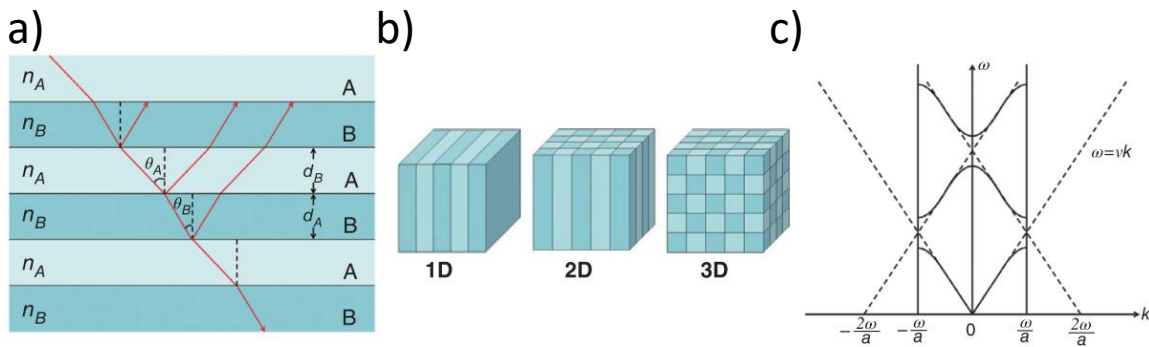
Figure 1.1 Sources of structural color. A multilayer structure, with alternating layers of high and low index materials (a). Reflects a preferential wavelength depending on the layer thickness and incident angle. (b) shows 1D ,2D, and 3D crystalline structures that produce photonic effects.(c) Band dispersion diagram of a 1D photonic crystal.[8]

All structural color found in nature, can be simplified down to a multilayer or crystalline structure with dimensions on the scale of the visible wavelength of light. Shown in Figure 2.1a, when light impinges on a multilayer photonic stack of periodic layers that alternate between materials of high and low refractive indices, only certain wavelengths will undergo constructive interference, when reflected. Reflected wavelengths can be controlled by thickness of these alternating layers and the respective refractive indices. For multilayer stacks the apparent color will change as the observation angle changes, producing the iridescent property. Likewise, with any photonic crystal, from a 1 dimensional (1D) multilayer to a two-dimensional (2D) or three-dimensional (3D) spatially periodic photonic crystal, similar physics can be observed. 2D and 3D photonic structures optical behavior is comparable to crystalline solids. The contrasting periodic refractive indices give rise to a photonic band gap in similar fashion that crystalline solids give rise to an electronic band gap though the lattice arrangement of ions.

Examples of structural colors due to multilayer reflection can be found on beetles[9–11], birds[12], tarantulas[13] and butterflies[5,14], as well as other animals[15–17]. While multilayer reflection is the most common source of structural color in nature, there are many examples of structural colors due to a 3D crystalline structure. [18] For example, the chameleon's color
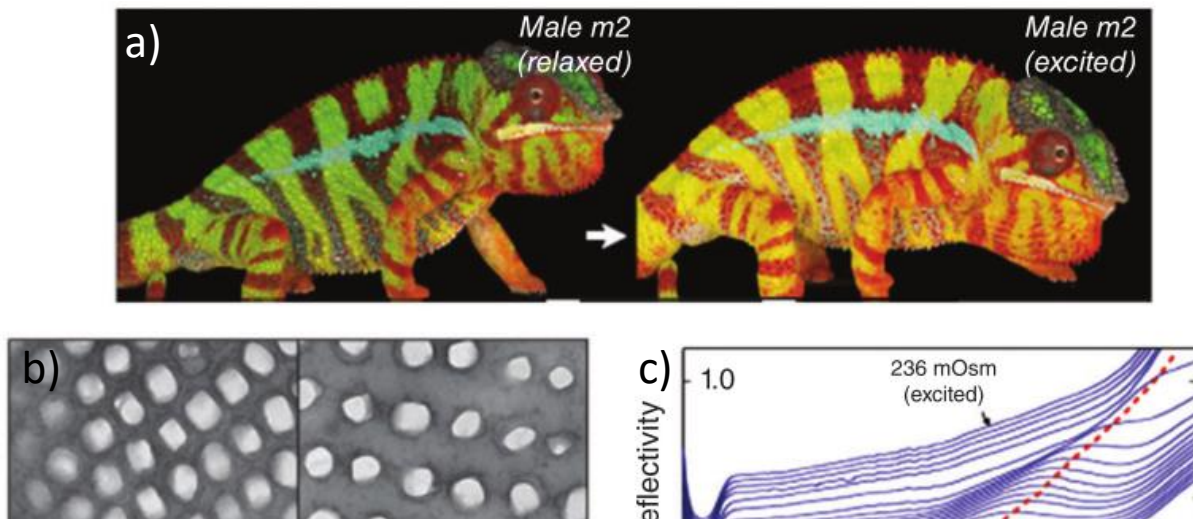
Figure 1.2 Reversible color change in the skin of a male panther chameleon from relaxed to excited state (a). (b) TEM images of the lattice of guanine nanocrystals in S-iridophores from the same individual in a relaxed (left panel) and excited (right panel) state. Scale bar, 200 nm. (c) Reflectivity of a chameleon skin sample with white skin osmolarity from 236 to 1416 mOsm.[19]

changing ability was recently shown to be the result of crystal structures in its skin, shown in Figure 1.2. When the chameleon feels threatened or aroused the nanostructured layer of skin will contract, changing the spacing between the nanoparticles and thus the color reflected.[19] Additionally the chameleon has a deeper skin layer that is embedded with rod-like nanoparticles that reflects infrared light, aiding the reptile in staying cool.[19]

The underlying mechanism of structural color found in nature can be understood with simple physical principles however, the structures themselves vary in complexity As the photonic structures increase in complexity, the optical response acquires unique characteristics. [13,20,21] Take for example the blue tarantula, shown in Figure 1.3, the ultrastructure consists of multilayers wrapping around the hair, combined with sub cylindrical multilayers intertwined with the underlying multilayers. This complexity results in a nearly non-iridescent color while still maintaining short and long range order.[22] Another fascinating example of structural color is that of the *Morpho* butterfly genus. The optical behavior of the *Morpho* butterfly genus has piqued the interest of researchers due to its high intensity, color purity, and unique angular response. The *Morpho* butterflies color is the results of a distinct nanostructure on the surface of their wings.
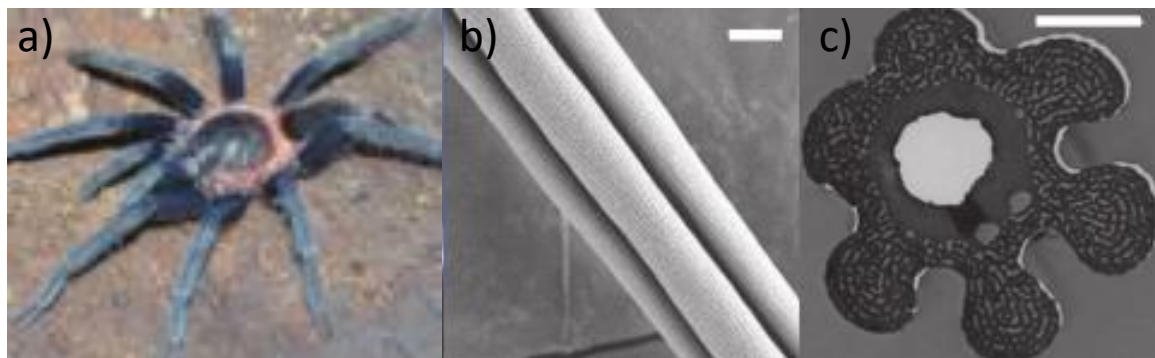
Figure 1.3 The blue tarantula and its nanostructure. Shown in (a) the Ischnocolinae tarantula. (b) and (c) show SEM and TEM micrographs of the spiders nanostructure. [13]

1.2.2 Structural color of the Morpho Butterflies

Although the colors and patterns of the different *Morpho* subspecies differ, the underlying nanostructures are quite similar. From the bluish white of the M. *sulkowskyi* to the dull blue of the M. *peleides*, each butterfly has ridges with tree like structures on the surface of the scales on their wings.[23] In particular, the *M. rhetenor* subspecies is known for its amazing blue color, shown in Figure 1.4(a–d). The thousands of overlapping scales combine to reflect over 60% of incident blue light. Over the last several decades *M. rhetenor* has been studied in detail, and the source of its optical behavior is now well understood.[24–27]
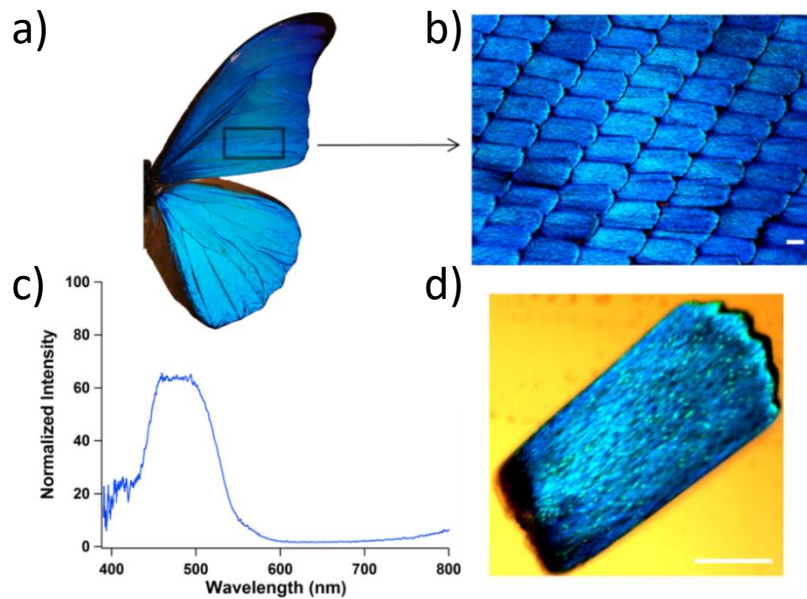
Figure 1.4 Images of Morpho rhetenor butterfly show the various structures found on its wings. a) A photograph of one half of the butterfly. b) Optical micrograph of the wing's tilted scales. c) An individual scale with grating-like structures visible. d) Reflection spectrum of the Morpho wing, with an intensity peak between 460 and 500 nm. Scale bars: 50 μm
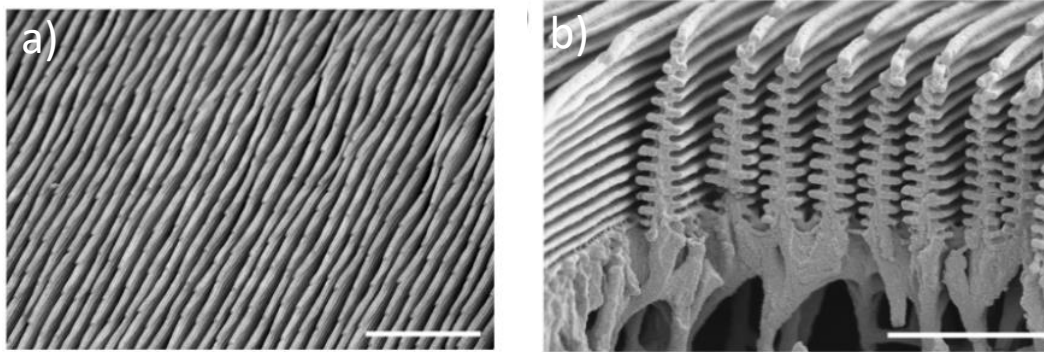
Figure 1.5 Scanning electron micrographs of Morpho rhetenor scales. (a) Quasi-parallel rows with varying heights and periods. b) The cross-section of the Morpho ultrastructures, showing alternating lamellae. Scale bars: a) 5 μm, b) 2 μm

1.2.3 Physics of the structural color of the Morpho butterfly

The nanostructures responsible for this brilliant color are quasi periodic ridges (Figure 1.5a) whose cross-sections resemble pine trees made of chitin (Figure 1.5a). A schematic of the nanostructure is shown in Figure 1.6, with each of the optically relevant geometrical parameters labeled. The "pine-tree" branches (lamellae) on either side of each tree are vertically offset (a), thus producing an asymmetric structure. Each pine-tree ridge randomly varies in height (h) and lateral spacing from its neighbors (b). A well as a tree "trunk" that has a slight taper (t). This hierarchical arrangement is often referred to as an "ultrastructure". The alternating lamellae-and-air stack of the ultrastructure gives rise to a multilayer interference effect, which regulates the wavelength of reflected light.[5,21,25,28–30] The spacing between each lamellae (d) dicatate that the structure will relfect blue light and the index of the chitin will determine the effective intesity of the reflection. Chitin has an index of refraction of 1.55, producing a large contrast between the lamellae and the air. The color purity across a wide range of viewing angles is enabled by the quasi-periodicity of the structures, which causes the light to spread.[23]

Diffraction effects are smeared out due to irregularity in the height of the ultrastructures and the asymmetry of each individual tree.[28,31,32] The irregularity of the structures thus allows each ridge to contribute separately to the overall optical effect.
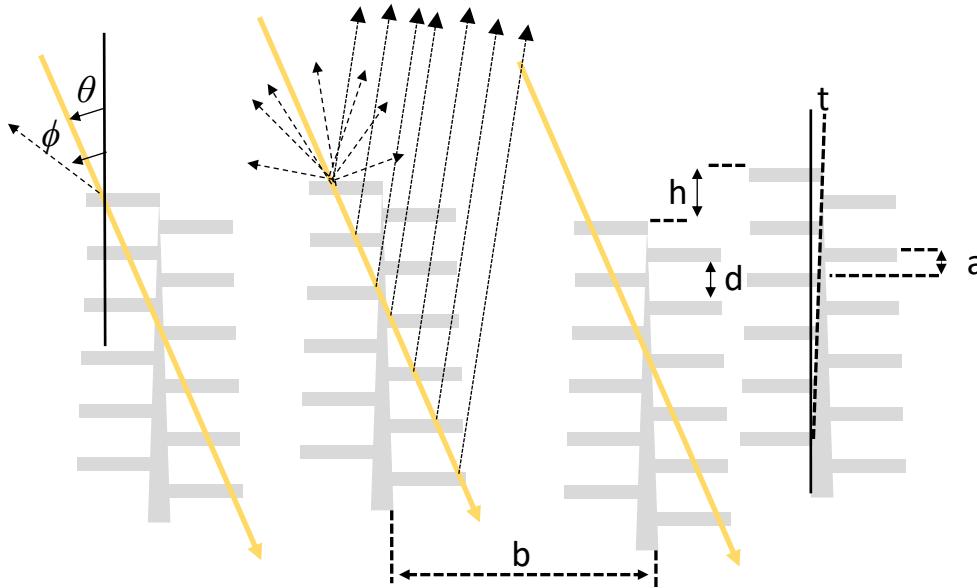
Figure 1.6 Morpho nanostructure schematic. There are several important geometrical parameters that are responsible for the unique optical response of the Morpho butterfly. The irregular spacing between ridges (b), and variation in height (h) along each ridge eliminate diffraction. The multilayer lamellae- air stack preferentially reflects the blue wavelengths based on the distance between lamellae (d). The "trunk" taper and asymmetric offset of the branches on each side of the ridges, give rise to the characteristic two lobe reflection. This unique reflection is best characterized by looking at the angle of reflections ϕ for each incident angle θ.

1.2.4 Optical Properties of the Morpho butterfly: double angle measurement

The *M. rhetenor*'s ability to spread light is difficult to visualize when observing the butterfly. Yoshioka and Kinoshita, presented the angular spread of light from various Morpho subspecies, by placing a single wing/scale in front of reflective paper with a small hole for the incident light to come through.[26] Shown in Figure 1.7, the M. *rhetenor*'s reflection is compared to the M. *didus*, here it can be clearly seen just how effectively the butterfly nanostructures are able to spread the reflective light over a wide angular range. Additionally, Figure 1.7 demonstrates the

angular insensitivity of the reflected wavelengths. Careful inspection of the photographs would reveal a high intensity lobe all around the hole used to let incident light pass, with very little light being specularly reflected. However, this effect is hard to quantify in this simple experiment. Kambe et al. showed that measuring the incident angle (θ) vs scattering angle (ϕ) can provide an informative physical description of the angular color response.[33] M. *rhetenor* has been shown to actually exhibit a two-lobe back reflection in angular space. The θ - ϕ measurement will be explored in further detail in section 2.4.5 and description of the M. *rhetenor's* angular reflection will be discussed in section 2.5.1.

Figure 1.7 Angular reflection of a Morpho wing. (a) M. *rhetnor* (b) M. *didius* (c) experimental set up [26]
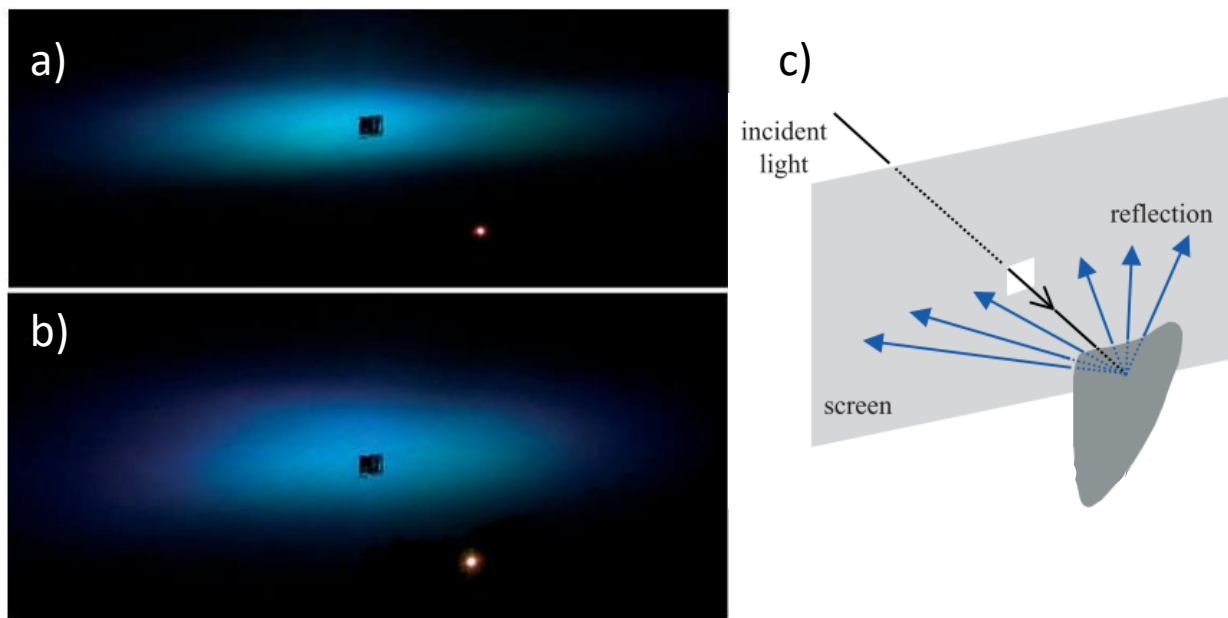
1.3 The Shape Memory Effect

The shape memory effect, is often associated with a class of so called 'smart' materials that have the potential to find applications across a whole swath of industries, from aerospace, to

biomedical and optics. Shape memory materials are those that have the ability to 'memorize' a

certain permanent shape (macroscopic or microscopic) and be fixed into a secondary (temporary)

shape through an applied external stimulus. This process can then be reversed through the

application of the same stimulus, thus the material 'remembers' the original shape. Shape

memory optics could be particularly attractive application for these materials. A single optical

element capable of multiple photonic shapes, would dramatically increase the functionality

without increasing complexity of a given system. One of the first reports of the shape memory

effect came in 1941, from L.B Vernon who claimed his methacrylic acid ester resin had an

'elastic memory', for dental applications.[34,35] The most advanced applications of the shape

memory effect come from the use of shape memory alloys, which typically occur in materials

with two stable crystalline structure. Each crystalline structure is thermodynamically favorable at

different temperature and a transition can be observed through the application of heat. AuCd was

the first reported shape memory alloy in 1951, but since then researchers have discovered a

plethora of materials that exhibit this effect. Draw backs of shape memory alloys include non-

tunable transition temperature, high cost, high stiffness and limited recoverable strain (~8%).[35]

These limitations gave the proper motivation for researches to develop alternative materials.

Polymers provided the pathway to overcome many of the limitations of shape memory alloys,

namely cost, and the ability to tune stiffness, recoverable strain and transition temperature.

1.3.1 Shape Memory Polymers

Shape Memory Polymers (SMPs) are a group of polymers that have the ability to switch

between one or more programed shapes. Research into SMPs, began to gain steam in the 1980's

and has quickly advanced, with SMPs finding their way into applications including stents, self-

folding structures, and smart clothing.[36,37] SMP and composites have been shown to

responsive to external stimulus of heat, sound, light, and electricity.[38–41] By far the most common type of SMPs are semi crystalline polymers that can transition between shapes via heat. These SMPs, as illustrated in Figure 1.8, are first crossed-linked (physically or covalently) into a permanent (primary) shape. Once cross linked, the polymer can be heated above the crystallite melting temperature (T_m) and molded, stretched or compressed into a secondary shape. The polymer is then quickly quenched, which freezes the crystallites into a secondary shape. When desired, the SMP can be heated above its T_m and it will revert to its original permeant shape. SMPs have been used in several applications were a single programing event is viable, such as stents.[37] However, a major limitation to SMPs is that without application of external constraints most shape memory processes are irreversible.[42–44] In most applications, a reversible processes would be needed for SMP products to be utilized as an optical element.
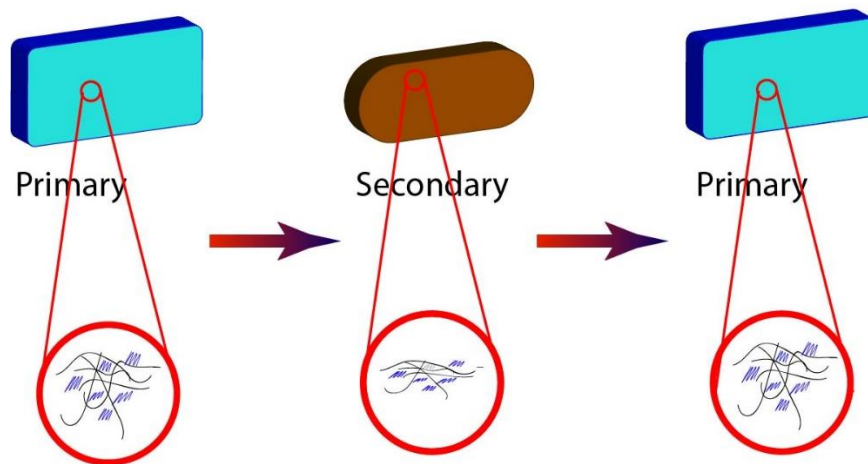
Figure 1.8 Shape memory Programing process

1.3.2 Reversible Shape Memory Polymers

Reversible shape memory (RSM), in which the shape can be actively tuned, was recently reported and shown to be able to reliably switch between its permeant and secondary

shape.[40,45,46] These processes require no external forces and do not need to undergo reprograming in between actuation. This hands-free functionality is the results of the interaction between the crosslinked polymer chains and the crystalline scaffold. When the polymer is heated to any temperature below its melting point (T_m), a crystalline scaffold remains. The crystalline scaffold provides a latent crystalline template, and the programmed shape is recovered upon cooling due to self-seeded crystallization along kinetically preferred pathways to replicate the scaffold. This reversibility can be controlled by tuning the chemical crosslinking density and the partial melting temperature. For poly(octylene adipate) bulk reversibility as high as 75% has been reported.[45]

1.3.3 Length Scales: From Macro to Micro to Nano

Almost all reported results of SMP actuation are on the scale of > 1 mm. Within the last decade micron and sub-micron SMP have been reported.[47–50] Zhao et al., showed the formation of micron and submicron wrinkles on the surface of pre-deformed SMP substrate coated with a thin gold film. After heating, the substrates returned to their primary shapes which induced sub-micron wrinkling. They were able to control the pattern and size of wrinkling depending on how the process of setting the secondary shape. RSM sub micron features were reported by Turner et al., they were able to show the change in contact angle as the height of different sub-micron shapes were varied.[51] SMPs have shown adequate ability to work on micron and sub-micron lengths scales but the optical response of RSM structures have not been studied. An RSM optical grating is an initial step in validating RSM polymers as suitable materials for truly multifunctional SMP optical elements.

1.4 Augmented Reality

Augmented reality (AR) is the overlaying of computer-generated images onto the real world in real time. In contrast, virtual reality (VR) is a completely immersive technology that closes off the user from the surrounding world and all images are computer-generated. Augmented reality has the potential to impact every industry and academic field, from engineering to computer science, architecture and the arts. The user base could be unlimited. However, in order to fully take advantage of the vast potential of augmented reality, there are several fundamental limitations in near eye displays (NED) used for AR and VR that need to be overcome. These limitation include limited field of view, low angular resolution and fixed accommodation.[52] Typically addressing just one of these limitations requires tradeoff in the others. Interchanging elastomeric polymer lenses in place of the traditional glass lenses, used in these systems, is one approach to improve on all of these limitations.

1.4.1 Vergence and Accommodation in the Eye

In order to understand the limitations of current NED it is important to review how the human eye focuses at varying distances. When the human eye attempts to focus on a near object, the lens of the eye will bend to bring into focus the light from the object. Likewise, when light comes from an object at a further distance, the eye lens must again bend to bring the object into focus. This process is called accommodation and is shown in Figure 1.9. Before accommodation can occur, the human eyes must rotate inward to converge so that the images coming from both eyes overlap, this process is called vergence. When objects are at a far distance the eyes will be parallel, as the distance between the eyes is small compared to the distance of the object. Likewise, when the object is close the eyes must rotate acutely until the images converge. An example of vergence is shown in Figure 1.9.

14

Accommodation

Far Object

Near Object

Cornea

Convergence

Far Object

Near Object
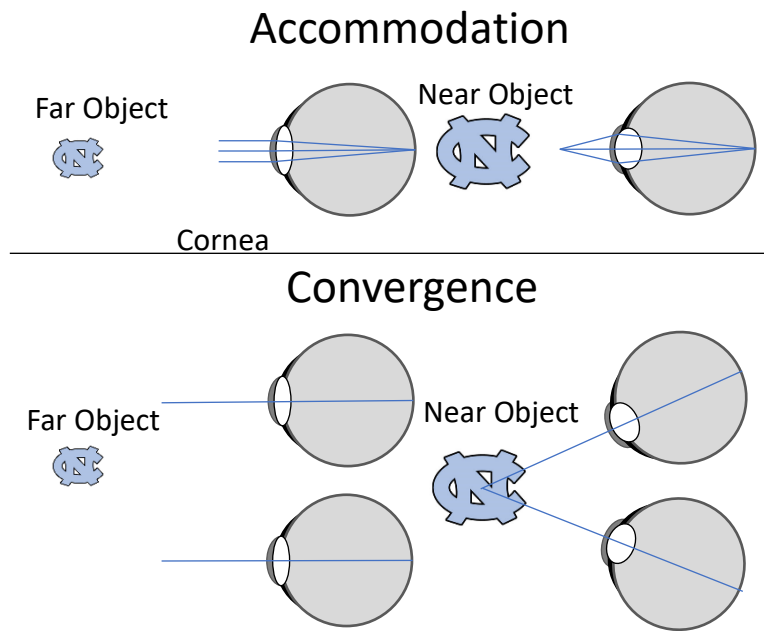
Figure 1.9 Vergence and Accommodation

1.4.2 Vergence-Accommodation conflict in AR and VR

Vergence and accommodation happen nearly instantaneously, and go relatively unnoticed during in everyday life. However, in basic AR and VR systems the content display is positioned approximately three inches from the viewer's eye. This presents a conflict between vergence and accommodation, as the lens of the eye will be focused on the light coming from the screen. Yet the eyes will converge on an object at any distance in the given field of view. This is often referenced as vergence-accommodation conflict and is the source of major discomfort for AR users. An example of viewing real world objects and NEDs, is shown in Figure 1.10. One way that companies and researchers have tried to address this issue, is by placing a single lens in between the user and the screen. At a focal length of 1 to 2m, as light coming from this distance tends to provide the most comfort possible over all distances. However, the need to fully address this issue remains, before wide spread adoption of this technology is possible. Elastomeric polymers allow for a new approach to overcoming this frustrating limitation. Elastomeric lenses

would provide on demand accommodative cues, possibly eliminating VAC in AR systems all

together.
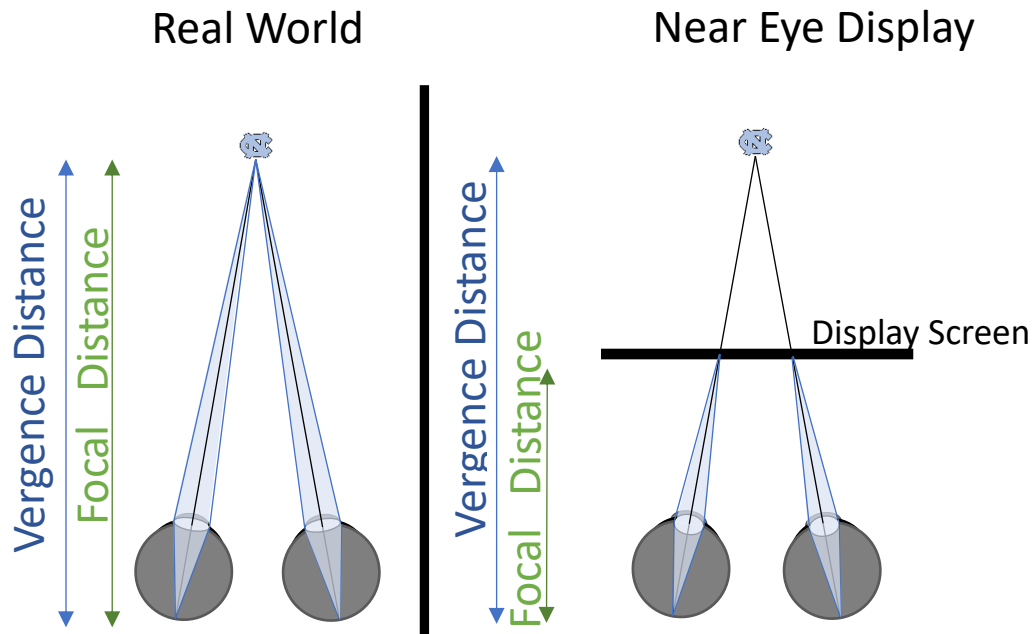
Figure 1.10 Real world and near eye display vergence and accommodation. With a real world object the vergence and focal distances are the same. In a near eye display system, the vergence and focal distance differ, causing visual discomfort for the user.

REFERENCES

[1]   Howard F 1988 *Wilbur and Orville: A Biography of the Wright Brothers* (New York: Ballantine Books)

[2]   Suddath C 2110 A Brief History of: Velcro *Time*

[3]   Hooke R 1665 *Micrographia, xxxvi. Of Peacoks, Ducks, and other Feathers of changeable colours.* (London)

[4]   Newton I 1704 *Opticks* (William Innys at the West-End of St. Paul's, London)

[5]   Kinoshita S and Yoshioka S 2005 Structural colors in nature: the role of regularity and irregularity in the structure. *Chemphyschem* **6** 1442–59

[6]   Vukusic P 2011 Structural colour: elusive iridescence strategies brought to light. *Curr. Biol.* **21** R187-9

[7]   Parker A R 2000 515 Million Years of Structural Colour *J. Opt. A Pure Appl. Opt.* **2** R15–28

[8]   Fu Y, Tippets C A, Donev E U and Lopez R 2016 Structural colors: from natural to artificial systems *Wiley Interdiscip. Rev. Nanomedicine Nanobiotechnology* **8** 758–75

[9]   Schenk F, Wilts B D and Stavenga D G 2013 The Japanese jewel beetle: a painter's challenge. *Bioinspir. Biomim.* **8** 45002

[10]   Anderson T F and Richards A G 1942 An Electron Microscope Study of Some Structural Colors of Insects *J. Appl. Phys.* **13** 748–58

[11]   Durrer H and Villiger W 1972 Schillerfarben von Euchroma gigantea (L.): (Coleoptera: Buprestidae): Elektronenmikroskopische untersuchung der elytra *Int. J. Insect Morphol. Embryol.* **1** 233–40

[12]   Stavenga D G, Leertouwer H L, Marshall N J and Osorio D 2011 Dramatic colour changes in a bird of paradise caused by uniquely structured breast feather barbules. *Proc. Biol. Sci.* **278** 2098–104

[13]   Hsiung B-K, Deheyn D D, Shawkey M D and Blackledge T A 2015 Blue reflectance in tarantulas is evolutionarily conserved despite nanostructural diversity *Sci. Adv.* **1** e1500709–e1500709

[14]   Ghiradella H 1991 Light and color on the wing: structural colors in butterflies and moths. *Appl. Opt.* **30** 3492–500

[15]   Search H, Journals C, Contact A, Iopscience M, Appl P and Address I P 2000 515 million years of structural colour **15**

[16]   Fu Y, Tippets C A, Donev E U and Lopez R 2016 Structural colors: from natural to artificial systems *Wiley Interdiscip. Rev. Nanomedicine Nanobiotechnology* n/a-n/a

[17]   McPhedran R C and Parker A R 2015 Biomimetics: Lessons on optics from nature's school *Phys. Today* **68** 32–7

[18]   Simonis P and Vigneron J P 2011 Structural color produced by a three-dimensional photonic polycrystal in the scales of a longhorn beetle: Pseudomyagrus waterhousei (Coleoptera: Cerambicidae) *Phys. Rev. E* **83** 11908

[19]   Teyssier J, Saenko S V., van der Marel D and Milinkovitch M C 2015 Photonic crystals cause active colour change in chameleons *Nat. Commun.* **6** 6368

[20]   Caveney S 1971 Cuticle Reflectivity and Optical Activity in Scarab Beetles: The Role of Uric Acid *Proc. R. Soc. London. Ser. B. Biol. Sci.* **178** 205 LP-225

[21]   Smith G S 2009 Structural color of Morpho butterflies *Am. J. Phys.* **77** 1010

[22]   Hsiung B-K, Deheyn D D, Shawkey M D and Blackledge T A 2015 Blue reflectance in tarantulas is evolutionarily conserved despite nanostructural diversity *Sci. Adv.* **1** e1500709–e1500709

[23]   Kinoshita S, Yoshioka S and Miyazaki J 2008 Physics of structural colors *Reports Prog. Phys.* **71** 76401

[24]   Vukusic P and Sambles J R 2003 Photonic structures in biology. *Nature* **424** 852–5

[25]   Zhu D, Kinoshita S, Cai D and Cole J 2009 Investigation of structural colors in Morpho butterflies using the nonstandard-finite-difference time-domain method: Effects of alternately stacked shelves and ridge density *Phys. Rev. E* **80** 51924

[26]   Yoshioka S and Kinoshita S 2004 Wavelength-selective and anisotropic light-diffusing scale on the wing of the Morpho butterfly. *Proc. Biol. Sci.* **271** 581–7

[27]   Lee R T and Smith G S 2009 Detailed electromagnetic simulation for the structural color of butterfly wings. *Appl. Opt.* **48** 4177–90

[28]   Siddique R H, Diewald S, Leuthold J and Hölscher H 2013 Theoretical and experimental analysis of the structural pattern responsible for the iridescence of Morpho butterflies *Opt. Express* **21** 14351–61

[29]   Steindorfer M a, Schmidt V, Belegratis M, Stadlober B and Krenn J R 2012 Detailed simulation of structural color generation inspired by the Morpho butterfly. *Opt. Express* **20** 21485–94

[30]   Banerjee S, Cole J B and Yatagai T 2007 Colour characterization of a Morpho butterfly wing-scale using a high accuracy nonstandard finite-difference time-domain method. *Micron* **38** 97–103

[31]   Kinoshita S, Yoshioka S and Kawagoe K 2002 Mechanisms of structural colour in the Morpho butterfly: cooperation of regularity and irregularity in an iridescent scale. *Proc. Biol. Sci.* **269** 1417–21

[32]   Johansen V E 2014 Optical role of randomness for structured surfaces. *Appl. Opt.* **53** 2405–15

[33]   Kambe M, Zhu D and Kinoshita S 2011 Origin of retroreflection from a wing of the morpho butterfly *J. Phys. Soc. Japan* **80** 1–10

[34]   Vernon L B and Vernon H M 1941 Producing Molded Articles such as Dentures from Thermoplastic Synthetic Resins US Pat. 2234993

[35]   Liu C, Qin H and Mather P T 2007 Review of progress in shape-memory polymers *J. Mater. Chem.* **17** 1543

[36]   Ratna D and Karger-Kocsis J 2008 Recent advances in shape memory polymers and composites: A review *J. Mater. Sci.* **43** 254–69

[37]   Yakacki C M, Shandas R, Lanning C, Rech B, Eckstein A and Gall K 2007 Unconstrained recovery characterization of shape-memory polymer networks for cardiovascular applications *Biomaterials* **28** 2255–63

[38]   Havens E, Snyder E a. and Tong T H 2005 Light-activated shape memory *SPIE 5762, Smart Structures and Materials 2005: Industrial and Commercial Applications of Smart Structures Technologies* vol 5762, ed E V. White pp 48–55

[39]   Xie T 2010 Tunable polymer multi-shape memory effect. *Nature* **464** 267–70

[40]   Behl M, Razzaq M Y and Lendlein A 2010 Multifunctional shape-memory polymers. *Adv. Mater.* **22** 3388–410

[41]   Liu Y, Lv H, Lan X, Leng J and Du S 2009 Review of electro-active shape-memory polymer composite *Compos. Sci. Technol.* **69** 2064–8

[42]   Chung T, Romo-Uribe A and Mather P T 2008 Two-way reversible shape memory in a semicrystalline network *Macromolecules* **41** 184–92

[43]   Pandini S, Passera S, Messori M, Paderni K, Toselli M, Gianoncelli A, Bontempi E and Ricc T 2012 Two-way reversible shape memory behaviour of crosslinked poly(??-caprolactone) *Polymer (Guildf).* **53** 1915–24

[44]   Westbrook K K, Mather P T, Parakh V, Dunn M L, Ge Q, Lee B M and Qi H J 2011 Two-way reversible shape memory effects in a free-standing polymer composite *Smart Mater. Struct.* **20** 65010

[45]   Zhou J, Turner S A, Brosnan S M, Li Q, Carrillo J Y, Nykypanchuk D, Gang O, Ashby V S, Dobrynin A V and Sheiko S S 2014 Shapeshifting: Reversible Shape Memory in Semicrystalline Elastomers ⊥

[46]   Meng Y, Jiang J and Anthamatten M 2015 Shape actuation via internal stress-induced crystallization of dual-cure networks *ACS Macro Lett.* **4** 115–8

[47]   Altebaeumer T, Gotsmann B, Pozidis H, Knoll A and Duerig U 2008 Nanoscale shape-memory function in highly cross-linked polymers *Nano Lett.* **8** 4398–403

[48]   Bae W G, Choi J H and Suh K Y 2013 Pitch-tunable size reduction patterning with a temperature-memory polymer *Small* **9** 193–8

[49]   Wang Z, Hansen C, Ge Q, Maruf S H, Ahn D U, Qi H J and Ding Y 2011 Programmable, pattern-memorizing polymer surface *Adv. Mater.* **23** 3669–73

[50]   Zhao Y, Huang W M and Fu Y Q 2011 Formation of micro/nano-scale wrinkling patterns atop shape memory polymers *J. Micromechanics Microengineering* **21** 67007

[51]   Turner S a, Zhou J, Sheiko S S and Ashby V S 2014 Switchable Micropatterned Surface Topographies Mediated by Reversible Shape Memory. *ACS Appl. Mater. Interfaces*

[52]   Kruijff E, Swan J E and Feiner S 2010 Perceptual issues in augmented reality revisited *2010 IEEE International Symposium on Mixed and Augmented Reality* (IEEE) pp 3–12

Chapter 2

Biomimetic Photonic Structures and their Angular Reflection

2.1 Introduction

Several optical characteristics of the M. *rhetenor* make it an attractive model to understand and emulate. The reflected color is nearly angular independent, until viewed at oblique angles and the nanostructure has a large specific surface area that is open to the environment, making it very sensitive to the surrounding medium. In this chapter I will discuss my initial approach to fabricating biomimetic Morpho nanostructures and the introduction of randomness through controlled drying. As will be shown, the introduction of randomness is crucial to begin to approach the optical qualities of the butterfly wings.

2.2 Possible Applications of Biomimetic Butterfly Structures

Artificial photonic structures inspired by the *Morpho* butterfly could exploit its unique optical properties for a variety of applications[1,2] *Morpho*-mimetic and simplified nanostructures have been explored for use as high-sensitivity gas,[3–5]chemical,[6] and

temperature sensors.[7,8] Further advances may allow for tunable structural color to find application in high precision- and broad-color gamut displays, waveguides, non-duplicable security labels and camouflage technology. In order for these applications to possess similar optical sensitivity, *Morpho*-inspired nanostructures must retain the *Morpho* butterfly's optical and morphological features.

2.3 Review of Bioinspired butterfly structures

The complex shape of the *Morpho* nanostructure is a challenge for any potential fabrication. Alternative approaches to produce structural color include rigid and polymeric multilayers[9,10] or self-assembled colloidal films.[11–13] While these methods can produce non-diffractive colors observable near normal incidence, intense diffractive colors with strong angular dependence are observed outside of this narrow angular range. Angle dependence in the reflection spectra of multilayer stacks and colloidal films has been overcome by applying lessons from the *Morpho* butterfly, utilizing variations in height and periodicity to produce structural randomization.[14–16] However, multilayer stacks fail to reproduce the large specific surface area and angular response of the butterfly, limiting the possible applications, such as sensors that require a large surface area to elicit a wavelength response while interacting with gases or liquids.

Attempting to replicate the exact structure of the butterfly, some researchers have used the butterfly wings as a biological template for direct molding.[7,17–21] This approach accurately reproduces the exact shape of the ultrastructure and the optical response can be tuned by changing the composition or thickness of a deposited coating on top of the butterfly structures. However, the need for the natural template limits the applicability of any such device. Ultrastructures that exhibit optical effects similar to the butterfly's optical response have been

demonstrated by direct ion beam writing[22] and e-beam lithography,[5,23,24]but these methods are limited in scale and avoid the diffraction effects of periodic structures by studying the optics of a few structures. Recently Zhang et al. showed a new approach to fabricating Morpho-like biomimetic structures by the use of ebeam lithography. Zhang used a multilayer stack of polymethyl methacrylate and Lift-Off resist, after ebeam exposure the multilayers were dissolved via alternating development of the layers. Siddique *et al*. demonstrated a photolithography method that allows for large-area fabrication and broad angular response for blue light, but the fabrication method does not allow for the introduction of randomness similar to the butterfly to break the periodicity.[25]

I will show the fabrication and optical characterization of periodic and quasi-periodic ultrastructures made of perfluropolyether (PFPE). The polymer material allows for the introduction of randomness, in order to optically decouple the individual ridges. Both periodic and quasi-periodic versions of the artificial butterfly structures differ substantially in their angular response but have similar normal-reflection spectra, which peak in the region of the real butterfly's color.

2.4 Experimental Methods

2.4.1 PFPE synthesis

1g (1 mmol) perfluoropolyether (PFPE) (Solvay Solexis) was dissolved in 50 mL dry methylene chloride. Triethylamine (2 mmol, 0.2 g) was dropwise added to the solution at 0 °C. 2-Isocyanatoethyl methacrylate (2.1 mmol, 0.33 g) (TCI America) was added to the solution and stirred overnight at room temperature. The solution was filtered, and remaining solvent was removed by rotary evaporation. The product was purified by washing with toluene,

centrifugation and then drying *in vacuo* at room temperature.180 MPa PFPE was made by mixing 1k PFPE with 1,1,5,5-tetrahydroperfluoro-1,5 pentanediol dimethacrylate monomer at a ratio of 1:3. The solution was then mixed with 2% w/v of photointiator 2,2-diethoxyacetophenone.

2.4.2 Fabrication of hard master

Fabrication steps of the hard master are shown in Figure 2.1 and was first reported by Aryal et al.[26]. First a multilayer stack of Silicon Nitride (Si_3N_4) and Silicon Dioxide (SiO_2) pairs were deposited by low pressure chemical vapor deposition (LPCVD). Si_3N_4/SiO_2 was chosen for several reasons, first Si_3N_4 and SiO_2 have been widely used for decades and have been studied and well understood. Second, the intent of this project was always to use standard microfabrication techniques that would allow for large area fabrication and provided less inertia to scale up. The multilayer stack was then coated with a positive photoresist (Shipley 1811, Microchem) using a spin coater and exposed using an in house interference lithography system. The exposed sample is then developed in a basic solution (MF-319, Microchem) and the exposed areas are washed away. Subsequently a grating remains, and is placed in a physical vapor deposition (PVD) system to deposit a mask material. In this case a KJ Lesker PVD 75 system was used to deposit ~ 100nm of chromium (Cr). The sample was then placed in an acetone bath and sonicated for several minutes to lift-off the photoresist grating. The remaining Cr line will act as mask for dry etching. Samples were dry etch with a Alcatel AMS 100 Deep Reactive Ion Etcher, using Argon ion bombardment to mill the exposed multilayer stack. A constant flow of C_4F_8 was used as means to both increase the resistance of the Cr mask and to control the taper of the etch. For a standard etch 150 sccm of Argon and 17 sccm of C4F8 was flowed through the system as 1400W was applied to ionize the gas and 75W was applied to the sample to direct the

ions to the sample surface. A multilayer stack of five pairs of Si_3N_4/SiO_2 typically required 12 minutes to etch. After dry etching the remaining Cr was removed with a Cr etchant, and the samples were dipped into a 10% hydrofluoric acid (HF) bath to selectively etch the SiO_2 layers. The 10% HF would etch approximately 3nm/s, and were typically etch for 40 seconds, to produce 120nm branches.
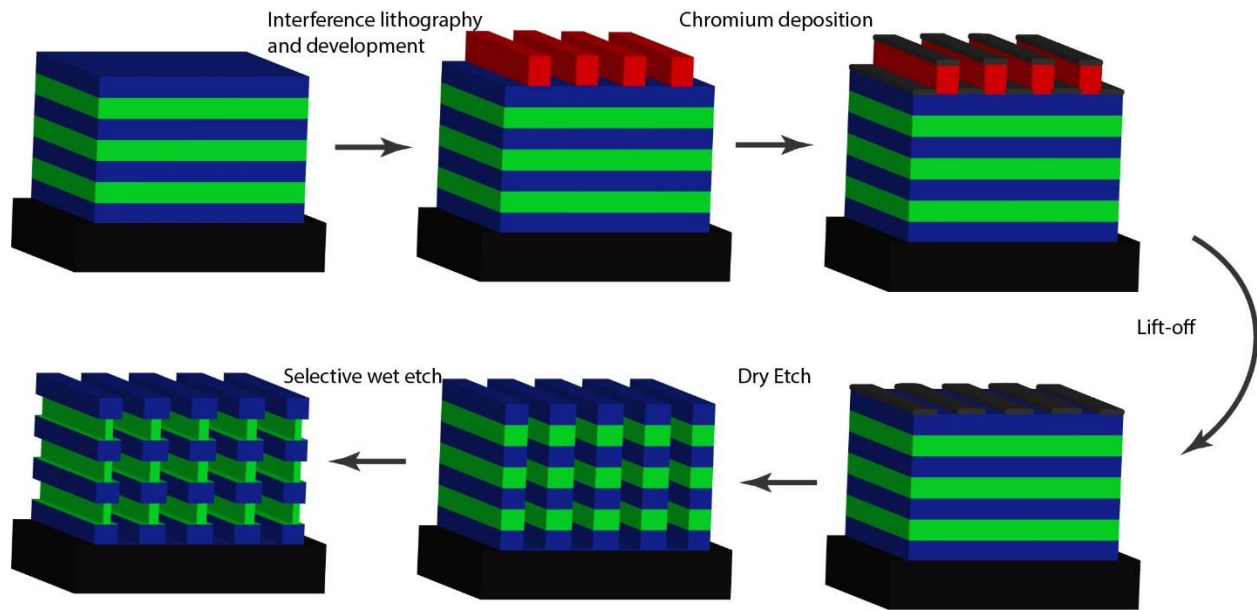
Figure 2.1 Hard Master Fabrication. A multilayer stack of Si_3N_4/SiO_2 is deposited by LPCVD. Interference lithography is used to expose periodic lines across the surface of the sample. Cr was deposited onto the substrate and a liftoff step leaves Cr lines as a dry etch mask. Argon milling results in multilayer ridges, which are subsequently wet etch in HF to create the "branches" of the tree.

2.4.3 Interference Lithography and development

Interference lithography (IL), is a photolithography technique that uses an interference pattern to expose a periodic pattern on a photoresist film. At the sample surface, two coherent light sources cross paths and, undergo constructive and destructive interference, producing a periodic pattern of maximum and minimum intensities. This interference pattern is then used to

expose the photoresist thin film, either a positive or negative resist, and is subsequently washed

in a suitable developer. The exposed or unexposed areas are washed away depending on the

resist choice. This pattern can then be used as a dry and wet etch mask, or as a mask for metal

deposition and lift off.

The advantage to using interference lithography over other photolithographic techniques

is the ability to expose wide areas with no loss of focus. Additionally, IL allows for the freedom

to create high density features with periodicities that can be easily changed by a simple change in

the set up. The most important feature to produce an interference pattern for lithography, is a

coherent and monochromic light source. A uniform wavefront is typically produced by

collimating the point light source. The beam is then split and the separate beams follow similar

path lengths before being directed toward the sample by mirrors, a prism, diffraction grating, or a

Lloyds mirror. A broadband source is possible to use however the use of a band pass filter or

diffraction grating would be required.

Figure 2.2 shows the general approach used to produce interference patterns used for the

biomimetic structures in this chapter. A 375 nm source laser is used, the beam is passed through

a pin hole to clean up the beam and then passed through a beam splitter. The two beams pass

through an additional pin hole to ensure that the expanded beam is, as uniform as possible. Then

the beam is   allowed to expand till it

can cover the   entire substrate area.
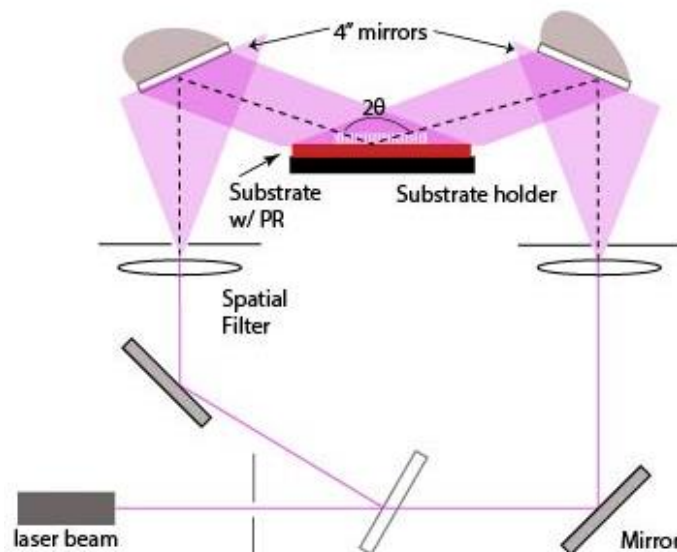
Figure 2.2 Interference lithography set up.

This set up was optimized, to allow for exposure of 2.5 cm^2 areas. The beams are then reflected off two large rotating mirrors. As discussed previously, the angle of reflection determines the periodicity of the pattern, the minimum repeating length is determined by the wavelength of the light source. The samples are then developed and dried. The duty cycle of these patterns can be controlled by varying the exposure and development times.
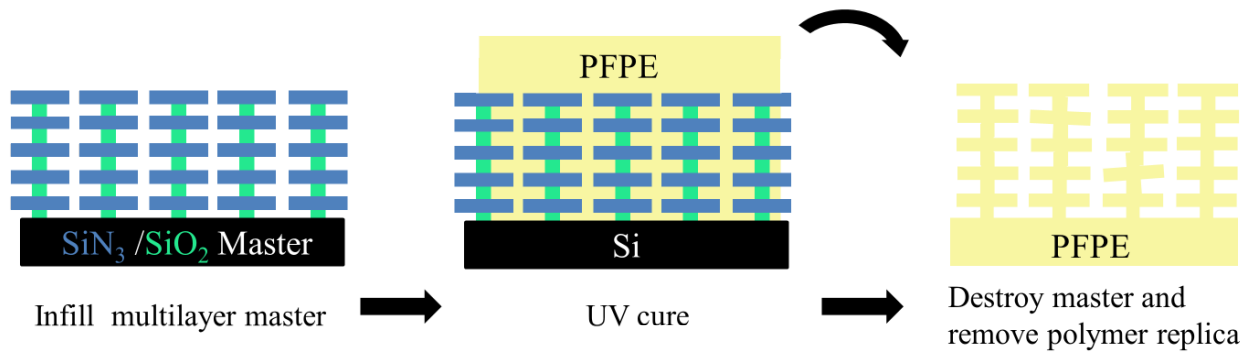
Figure 2.3 Polymer replica process for Morpho-inspired ultrastructures. a) The SiO_2 and Si_3N_4 master is infilled with PFPE and cross-linked under UV radiation. The master is then etched away in a hydrofluoric acid bath and the resulting PFPE replica is separated from the remaining Si substrate, followed by supercritical drying or air drying

2.4.4 Fabrication of PFPE structures

A PFPE solution was poured over the Si_3N_4/SiO_2 nanostructured hard master, and degassed in a desiccator for 30 minutes. The polymer was cross-linked under 365 nm light for 5 min in a nitrogen atmosphere. The cross-linked PFPE and hard master were then placed in 48% HF acid solution for several hours until the hard master was completely destroyed. Periodic-tree samples were kept submerged in water, and then transferred to a water-ethanol solution, gradually increasing the concentration until the sample was submerged in a 100%-ethanol bath. Subsequently, the sample was transferred to a Tousimis Semidri PVT-3 critical point dryer and immersed in liquid CO_2. After supercritical drying, the sample was separated from the remaining Si substrate of the hard master. For the quasi-periodic nanostructures, the sample was immediately removed from the acid solution and cleaned in deionized water. The PFPE replica and Si substrate were separated and the PFPE replica allowed to dry in air. PFPE replica process is shown in Figure 2.3.

2.4.5 θ-ϕ measurements

To fully appreciate *M. rhetenor*'s ability to spread light, incident vs reflected angle (θ-ϕ) measurements were performed for each wavelength. θ-ϕ measurements have been shown to present an informative description of the angular wavelength dependence of reflected light.[27] Angular optical measurements were taken for incident and reflected beams both ranging from $10°$ to $170°$ with a resolution of $2°$. The incident angle was changed by adjusting the sample angle using a rotary stage, while a second rotary stage, rotated $160°$ about each incident angle, and controlled the angle of collection. An unpolarized halogen light source with a 2-mm-diameter spot size was used to illuminate the sample and a Princeton Instruments Spectra Pro 2300i spectrograph with a Pixis 400 CCD, collected the visible spectrum for each angle. Samples were aligned, such that ridges ran vertical to the plane of the sample.
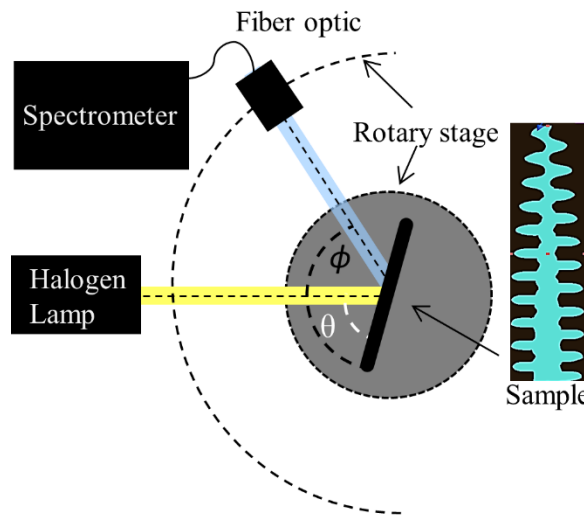
Figure 2.4 The θ-ϕ experimental setup. For incident angle (θ, white) a spectrum is taken for each reflection angle (ϕ, black) from $10°$ to $170°$; θ and ϕ are measured from the sample's plane. Note: When $\phi = \theta$, no data could be collected due to a limitation in the experimental setup.

A schematic of the θ-ϕ measurement setup is presented in Figure 2.4. The *M. rhetenor* butterfly specimen was ordered from ButterflyUtopia.com.

2.4.6 Normal-incidence reflection measurements

A halogen lamp was used to illuminate the sample surface. Reflection measurements were taken at normal incidence and collected with a 20x objective with a 0.4 numerical aperture resulting in a collection cone of 46°. Spectra were normalized using reflected light from an aluminum-coated mirror. Reflected light was analyzed with an Ocean Optics USB4000 spectrometer.

2.4.7 FDTD simulations

Finite-difference time-domain (FDTD) computer simulations were performed using the commercial software package FDTD Solutions (ver. 8.12.501 by Lumerical Solutions, Inc.) on a single workstation with two octa-core 2.0-GHz processors and 64 GB memory. Each set of 2-D simulations consisted of nested sweeps of the illumination parameters: incident angle ($\theta = 20$–$160°$, $\Delta\theta = 2°$), electric-field polarization (transverse electric and transverse magnetic, TE and TM), and wavelength (one or more values within $\lambda = 400$–520 nm). The largest sets contained close to 1000 individual simulations and ran for about 24 hours, including far-field post-processing. The scattering object(s), i.e. one or more *Morpho*-like (Figure 2.5c) or *Morpho*-mimetic (Figures 2.7 and 2.11(a, e, i)) "trees" in vacuum (Figure 2c) or on a substrate of the same refractive index, were placed inside a 2-D computational domain (20 x 2 μm^2) surrounded by absorbing boundaries of 80 uniaxial perfectly matched layers (UPML). The domain was meshed globally with a non-uniform conformal mesh, while a smaller rectangular region containing the scatterer(s) was meshed locally at uniform 5-nm increments in both directions. A total-field/scattered-field (TF/SF) source region spanning the inside of the overriding local mesh injected a monochromatic plain wave down from ~50 nm above the scatterer(s). With the incident electromagnetic field removed by the output boundaries of the TF/SF source, only the

near-zone fields scattered by the object(s) were collected by a horizontal line monitor placed ~100 nm above the object(s) and cutting across the full domain and side UPML boundaries. The time-dependent near fields collected by the monitor were first Fourier-transformed into frequency space, and then transformed to the far (radiation) zone (here: 1 m away from the origin in the upper hemisphere) at different scattering angles ($\phi = 20–160°$, $\Delta\phi = 1°$). At each wavelength of interest, the squares of the magnitudes of the complex electric far fields for TE and TM incident polarizations were added together, and the resulting far-field "intensity" ($|\tilde{E}_{far}|^2$) was plotted on a ϕ-vs-θ color-scaled image as a function of scattering and incident angles.

2.5 Results and Discussion

2.5.1 Morpho Butterfly θ-ϕ measurements

A double-angle measurement of a M. rhetenor wing, was taken for each wavelength and compiled into a video shown at this link. The video shows that short wavelengths spread over large angles, while the peak-intensity wavelengths concentrate the reflected (scattered) light into the two-lobe feature. Figure 2.5a shows the θ-ϕ angular measurement at 460 nm for the *M. rhetenor*. At short wavelengths (400-430 nm), the light is spread out over a large range of incident and reflected angles. For wavelengths larger than 430 nm, the intensity pattern begins to coalesce within smaller angular ranges and forms the high-intensity two-lobe pattern, as shown previously.[28] The intensity of the patterns peaks between 460 and 500 nm and then begins to dissipate. FDTD simulations (Figure 2.5b) of a single *Morpho* ultrastructure qualitatively reproduce this pattern, with angular position and general shape of the central peak similar to those found experimentally. The concentric ring features in the FDTD θ-ϕ pattern are the only difference between the simulation and the real butterfly. Testing variations in the structure (not shown), we noticed that those rings are much more dependent on the ultrastructure's geometrical

31

aspects than are the bright lobes, thus the real butterfly, with its millions of non-identical ridges

must average out the rings effectively. Overall, the simulation indicates that each ultrastructure

row on the scales of the butterfly contributes incoherently to the optical signature without

undergoing significant interference with neighboring ultrastructures.[29] This θ-ϕ pattern

illustrates the challenge of artificial reproduction of the *Morpho* color characteristics,

highlighting the need for decoupling the ultrastructures while simultaneously maintaining

parallel nanofabrication.
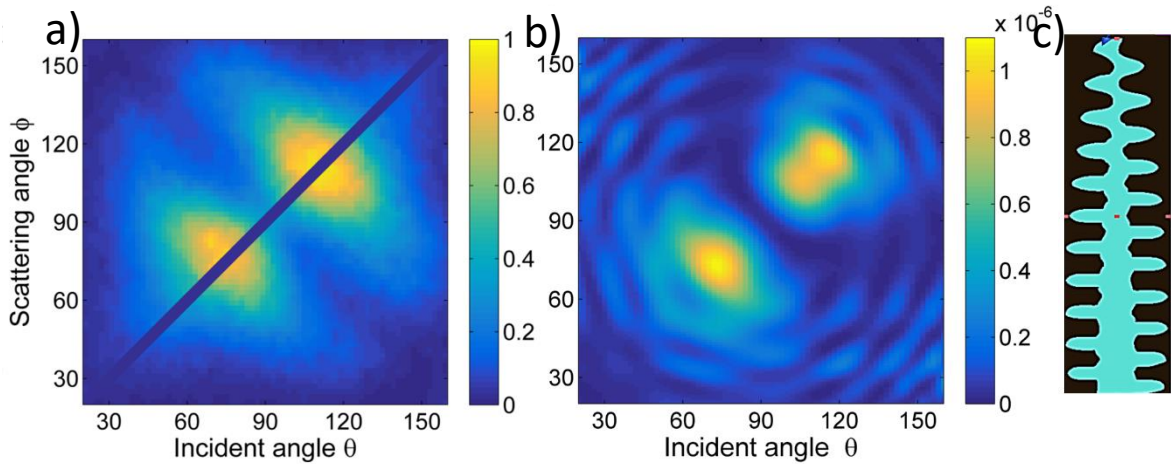
Figure 2.5 Experimental and simulated θ-ϕ of the Morpho rhetenor. (a) The θ-ϕ sweep at 460 nm of the M. rhetenor wing shows regions of strong back-reflection peaking in intensity between 460 and 480 nm. (b) Two-dimensional (2-D) FDTD simulations of far-field electric-field intensity scattered from the cross-sectional model of a single M. rhetenor ridge, with a similar peak position of the two-lobe optical signature. (c) Simulated Morpho "tree", based on previously reported cross-sectional model. [28]

2.5.2 Biomimetic Periodic Nanostructure
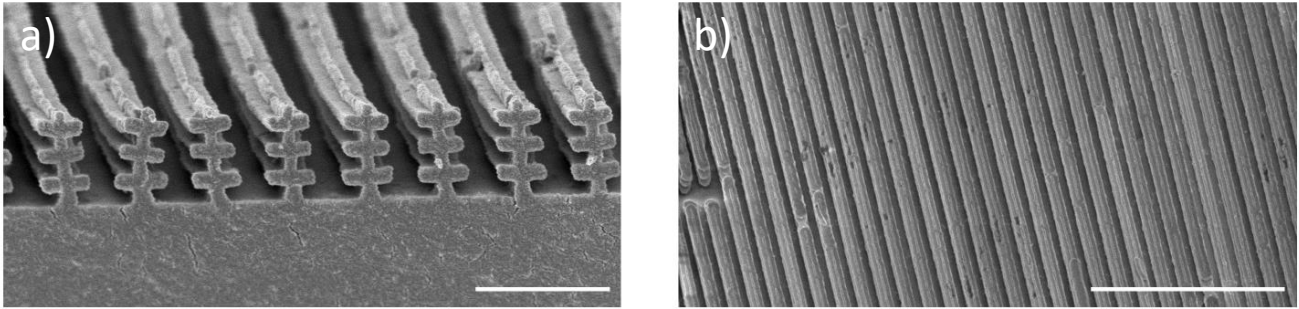
Figure 2.6 SEM of periodic nanostructures. a) The cross-section of super critically dried periodic polymer ultrastructures. b) The aerial view of the periodic replica ridges. Scale bars: b) 1 um and c) 5 um

Initially the biomimetic structures were fabricated as shown in Figure 2.3, and then super critically dried in order to maintain the periodicity. Figure 2.6(a and b) shows the resultant nanostructures after supercritical drying. These vertical nanostructures reflect blue-green light that peaks at ~510 nm for normal incidence (Figure 2.7a). Reflection measurements were taken at normal incidence and collected with a 20x microscope objective with a full angular collection of 46°. Visual inspection of the sample shows the blue and green colors arise mostly from angles close to the specular reflection (Figure 2.7a inset). θ-ϕ angular measurements (Figure 2.7(c,e,g)) show very strong specular reflection (diagonal form top left to bottom right), but also significant diffraction consistent with the sample periodicity, resulting in well-defined arcs in the lower-left and upper-right regions of the θ-ϕ plane. The θ-ϕ angular measurements reveal three main reflection signatures dependent on wavelength. For short wavelengths (400-440 nm), two high-intensity narrow spots appear along the specular reflection line (Figure 2.7c). For longer wavelengths, the spots expand toward the sample's normal until they merge (Figure 2.7e). The light intensity then further concentrates around the sample's normal (Figure 2.7g). This angular response is reproduced fairly well by the 2-D FDTD simulations using a finitely periodic array of nine identical ultrastructures based on a SEM cross-section image of the sample (Figure 2b).

Figure 2.7(d,f,h) show the FDTD simulations at different wavelengths illustrating the three

observed regimes. The origin of this angular dependence can be explained by realizing that, in

the specular reflection region, the dominant contribution is the multilayer nature of the

ultrastructures, which, given their dimensions,
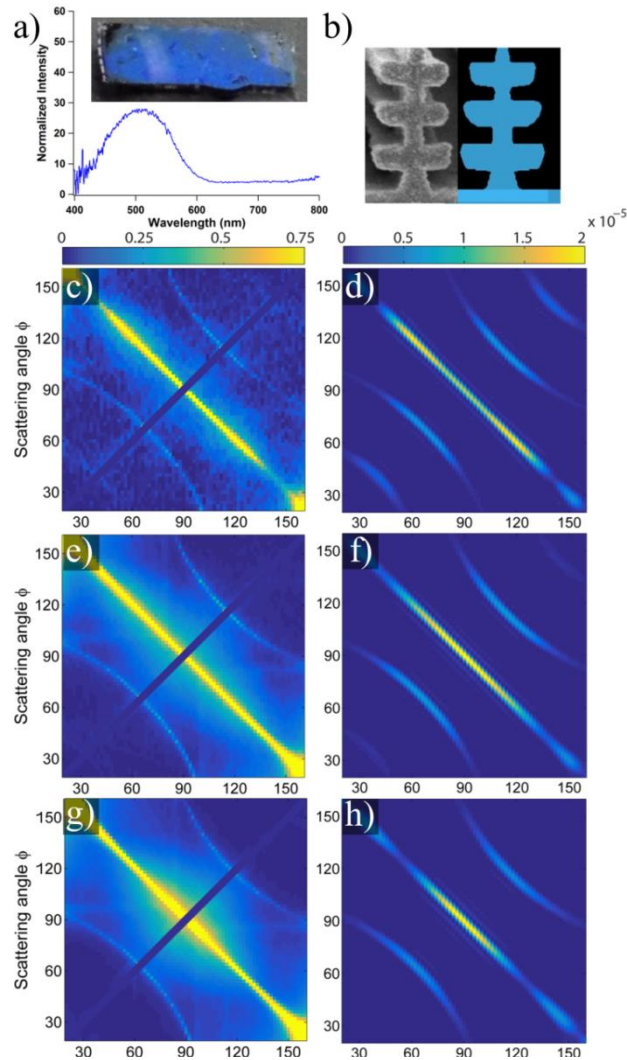
Figure 2.7 Experimental and simulated θ-ϕ of periodic nanostructures. a) Reflection spectrum of periodic Morpho-mimetic periodic polymer nanostructures. Inset: Photograph of PFPE replica specular reflection taken under ambient light. b) SEM cross section of a single ultrastructure and the symmetrized version used for FDTD simulations. θ-ϕ measurements of the periodic nanostructures for wavelengths 430, 470 and 520 nm (c,e,g) and FDTD simulations of nine three-branch nanostructures spaced laterally by 575 nm (d,f,h). Note: When $\phi = \theta$, no data could be collected due to a limitation in the experimental setup.

will have an enhanced reflection for longer wavelengths at normal incidence and will require incident angles farther from the normal for shorter wavelengths.[28]

Consistent with the measurement, the FDTD simulation shows the diffraction arcs are weaker in intensity compared to the specular intensity and their position in the θ-ϕ plane is equally well predicted. While these vertical trees are a simplified model of the butterfly, they successfully reproduce its color. However, due to their strict periodicity, they do not closely reproduce the angular optical response of the natural butterfly. In order to approach it, the strict periodicity needs to be broken.

2.5.3 Quasi-periodic nanostructures

Randomness and asymmetry in the *Morpho* butterfly ultrastructure have been shown to be important for its angular optical signature.[30,31] By altering the periodicity of the nanostructures, the specularly reflected and diffracted light can be scattered instead. Quasi-periodic nanostructures were fabricated in a similar fashion as the periodic trees described in Figure 2.3. However, on removal from the acid solution, the PFPE replica was separated from the remaining silicon substrate and air dried, rather than super critically dried. Figure 2.8(a-c) shows representative SEM images of the *Morpho*-mimetic structures. Aerial SEM images of the sample (Figure 2.8(b,c)), taken at a 45° tilt, show that the polymer ultrastructures have randomly leaned onto each other, forming a quasi-periodic pattern. Structure randomization occurred due to capillary forces during the air-drying process. The cross-section (Figure 2.8a) shows the tapered tree-like structures consisting of five lamellae of PFPE forming multilayer stacks with the surrounding air. While this quasi-randomness differs from that seen on the *M. rhetenor*, which is truly uncorrelated, the quasi-randomness produced by capillary forces affects both the

height and period of each ultrastructure, which have been shown to be important for producing a *Morpho*-mimetic optical response.[29,32,33] Visually, the randomized geometry of this sample resulted in a very weak specular reflection but enhanced blue-green color for angles off the mirror observation line (i.e., diagonal from top left to bottom right in the θ-ϕ plot).
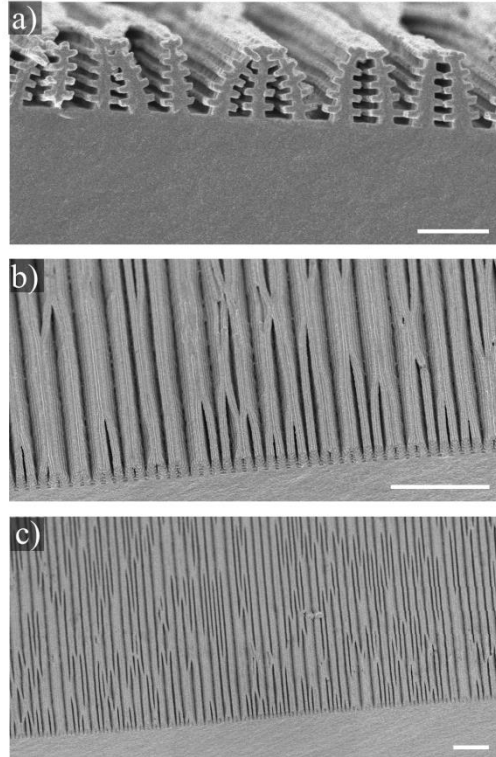
Figure 2.3. SEM micrographs of qausi-periodic structures. a) SEM cross-section of the polymeric ultrastructures, with ridges of ultrastructures leaning onto each other after air drying, mainly forming groupings of two and three trees. (b-c) Aerial SEM images of the replica ridges taken at a 45° tilt for two different magnifications. Ridges bend and stick to each other, introducing randomness to the overall periodicity of the sample. Scale bars: (a) 1 um (b,c) 5 um

2.5.3.1 Randomness via drying

Comparison of drying samples in air or on a hot plate showed no significant difference in being able to control how the sample dried and the resultant randomized structures. Instead effects on the wettability of the sample due to minor changes in the nanostructures and the

mechanical properties of the PFPE had the greatest effect. Overall it was difficult to fully control the randomization of the surface structures via this method and a different approach is needed to control the optical response.

2.5.3.2 Optical Results of Quasi periodic nanostructures

Figure 2.9a shows the normal-incidence reflection spectrum of the quasi-periodic PFPE structures, with the reflected intensity peaking around 550 nm; a digital photograph of the sample's surface is shown in Figure 2.9d. The angular distribution of the randomized PFPE ultrastructures was measured using the θ-ϕ setup described in section 2.4.5.
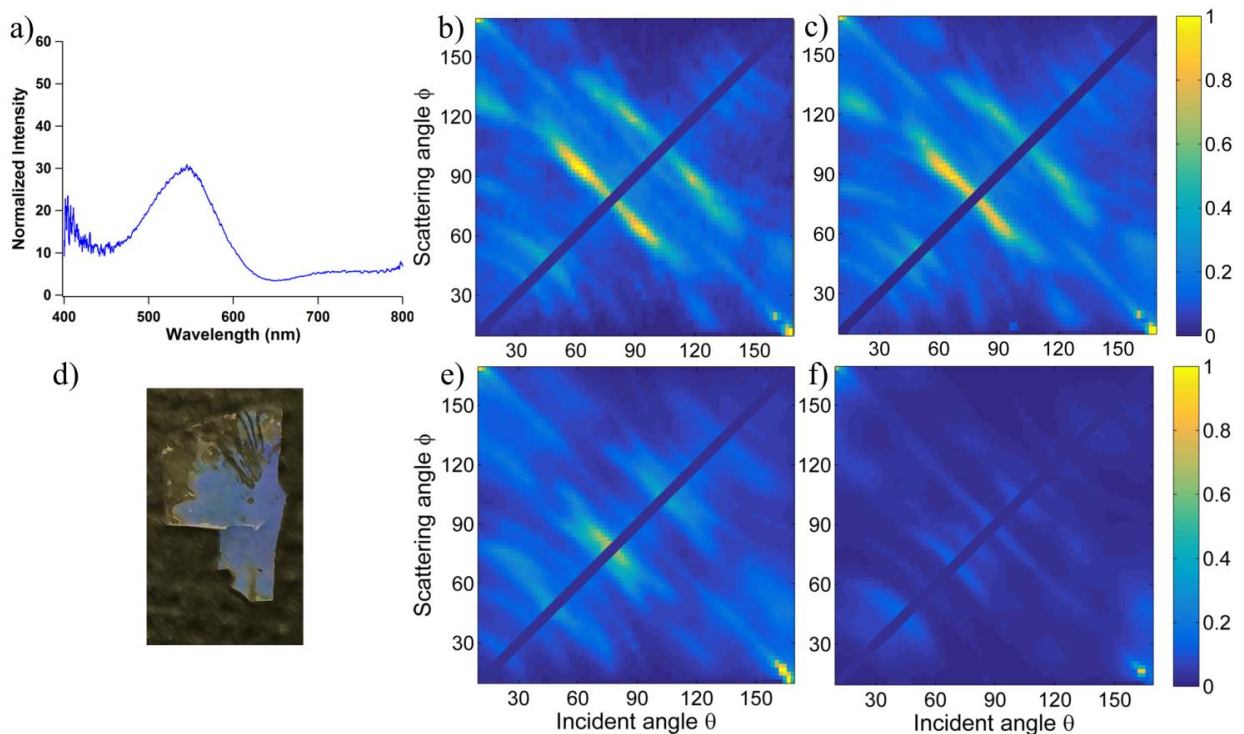
Figure 2.9 Optical analysis of quasi-periodic sample. a) Reflection spectrum of quasi-periodic PFPE sample. θ-ϕ data for the "artificial butterfly" sample, taken at various wavelengths. The unique angular response of the quasi-periodic sample is shown for wavelengths b) 460 nm and c) 480 nm. d) A photograph of a quasi-periodic sample, taken under ambient light at $\phi = 90°$, demonstrating the color seen within the two-lobe angular region. Beyond 480 nm, the pattern begins to dissipate but first concentrates about 15° away from normal incidence as seen for e) 525 nm. The pattern intensity decreases until only diffraction lines are visible at f) 600 nm. Note: When $\phi = \theta$, no data could be collected due to a limitation in the experimental setup

Figure 2.9(b,c,e,f) show θ-ϕ measurements at wavelengths of 460, 480, 520 and 600 nm, respectively. For the shorter wavelengths, the reflected signal is dominated by high-intensity regions "sandwiching" the mirror line. The features appear two-lobed and do not match the curving and location of the typical diffraction arcs expected for the nominal period (cf. Figure 2.7 for the strictly periodic case). At longer wavelengths, the pattern coalesces by first concentrating around $\pm15°$ away from normal incidence before mostly dissipating.

2.5.3.3 Importance of Absorption

Visual inspection of the quasi periodic biomimetic samples would show a strong back reflected blue-green color, but what is often neglected or ignored throughout literature on biomimetic structural color is the importance of absorption. Absorption plays two roles for perceived color in biological models. First, almost all wavelengths that are not reflected by the nanostructure are absorbed, eliminating chances for the light to be reflected back toward the observer, and thus muddling the perceived color. Second, the additional contrast allows the color to appear richer and purer, to the humane eye. On the Morpho butterfly the absorption layer is positioned within 10 µm bellow the nanostructures.

Recently absorption has been the focus of structural color in biomimetic polystyrene (PS) photonic crystals to enhance perceived color.[34] For the biomimetic samples in this chapter and in chapter 3, a coating of carbon black paste was applied to the back of the sample. Before application of the paste, the blue color of the samples was apparent but saturated. Diffraction also appeared stronger due to reflections off the backside of the PFPE. After application of the reflected color appeared stronger and diffraction was dependent only on the surface structures. Proximity of the absorbing layer has been shown to be important to improving contrast and the

appearance of the reflected color.[34] Samples in this study varied in thickness but typically were 2-4 mm thick. Sample thickness was not reduced more, as thinner samples tended to curl after etching away the hard master. Color contrast could be improved by incorporating carbon black particles into the PFPE mixture before cross linking.

2.5.4 Origin of the Optical Signature

Further analysis reveals that the optical signature is a product of the quasi-random periodicity formed when the ultrastructures collapse together during air drying. Figure 2.10a highlights the various groupings seen on the surface of the quasi-periodic samples. Nanostructures randomly switch leaning direction against their neighbors and form groups of two, three or four rows. To determine the dominant quasi-periodic structure, diffraction curves (1st, 2nd, 3rd and 4th order) were calculated for grating periodicities of 1, 2, 3 and 4 times the nominal fabrication period (575 nm). These curves are overlaid on the reflection data for a wavelength of 460 nm in Figure 2.10b. The double-period first-order diffraction arc aligns well with the angular pattern but the arcs from other grating orders seem close enough to possibly contribute, in particular because the overall lobe feature clearly curves the opposite way with respect to the simple diffraction arc. While the angular pattern appears to be a result of quasi-periodicity, it is important to note that the unique angular pattern peaks in intensity around 480 nm, after which the intensity continually dissipates. So, while faint and broad diffraction arcs are visible, the quasi-random structures disrupt the short-range order, such that only blue-green light is reflected. FDTD simulations of the two dominant periods, i.e. two and three rows stuck together, were performed based on SEM cross-sections of the quasi-periodic sample.
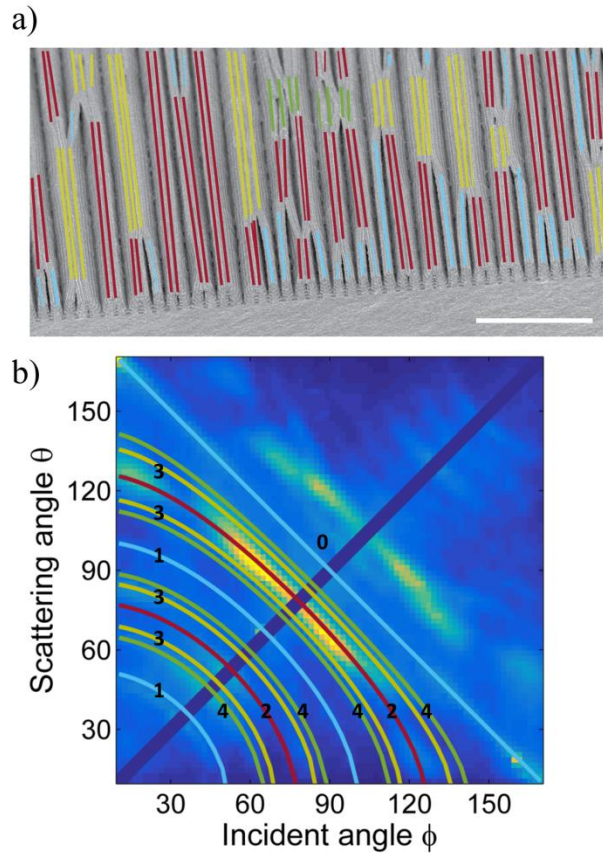
Figure 2.10 Underlying order. SEM of quasi-periodic surface with lines marking where various combinations contribute. Groupings of two ridges (red) appear to be the most common with groupings of one (blue), three (yellow) and four (green) ridges also visible. This results in periods of 2, 3 and 4 times the nominal period of 575 nm throughout the sample's surface. b) θ-ϕ map at 460 nm overlaid with calculated diffraction curves of the 1st, 2nd, 3rd and 4th order of the various periods found on the sample's surface: as-fabricated period (blue, 1), double period (red, 2) triple period (yellow, 3) and quadruple period (green, 4). The high-intensity lobes align predominantly with the double and triple periods.   Scale bar: 5 um

2.5.4 FDTD Simulations

In the simulations, the outlines of the trees were made symmetric, as shown in Figure 2.11(a,e,i). Rows of nine, five, and five structures were used, respectively, for single (Figure 2.11a), double (Figure 2.11e), and triple (Figure 2.11i) tree groupings. The resultant θ-ϕ

40

maps for wavelengths of 460 nm, 480 nm, and 520 nm are shown in the remainder of Figure 2.11. One immediate observation is that contributions from the single period, which shows strong zero-order (i.e., specular reflection) and first-order diffraction, seem to be completely absent in the experimental measurements. In contrast, the simulations of the double-tree structure predict high-intensity lobes somewhat reminiscent of the angular distribution of the experimental measurements, as already suggested by the calculated location of the diffraction arc (Figure 2.10b). The FDTD simulations show that the arcs are of high intensity near their centers and lose intensity at longer wavelengths, whereas the experimental measurements depict elongated lobes that are more intense toward each end rather than in the middle. The simulations of the triple-tree groupings seem to correspond to location of some of the weaker diffractive features observed in the experiment, but the intensity difference indicates that the periodic order is fragmented, yet not completely destroyed. Therefore, no grouping alone explains the experimental observations, but combinations of double- and triple-tree structures—varying locally across the sample in their precise *three-dimensional* geometry—are most likely responsible for the signature inward-curving lobes (Figures 2.9(b, c) and 2.10b) in the experimental optical response of the quasi-periodic "polymer butterfly".
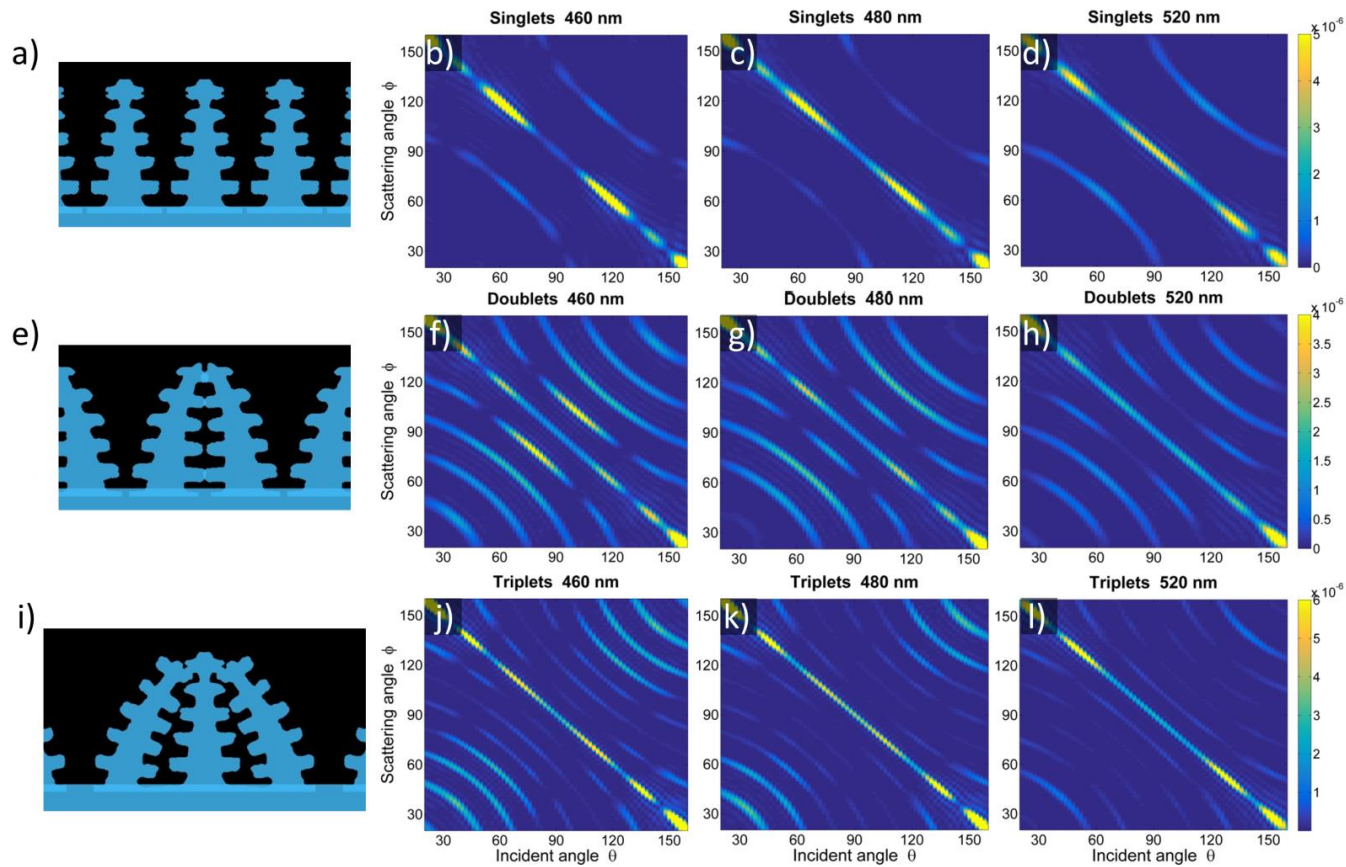
Figure 2.11 FDTD simulations of nine (singlets) or five (doublets and triplets) symmetric units of representative structure groupings found on the quasi-periodic sample. Schematics of the simulated trees are shown for single trees (a), double trees (e) and triple trees (i). Doublets and triplets were based on SEM cross-sections but symmetrized to simplify the model. θ-φ scattered intensity data were simulated and compiled for wavelengths of 460 nm, 480 nm, and 520 nm for each ultrastructure configuration: singlets (b-d), doublets (f-h), and triplets (j-l). A combination of the doublet and triplet simulation (with the exclusion of the nominal period diffraction and specular reflection, not seen experimentally) would explain the unique θ-φ two lobe signature observed for the quasi-periodic sample.

2.6 Conclusion

The *M. rhetenor* butterfly's structural color was angularly characterized over the visible wavelength range to establish its spectral and angular response characteristics. The butterfly exhibited a unique two-lobe pattern in the θ-ϕ angular space. Nanostructures on the surface of the butterfly's wing are the origin of its optical properties; in particular, the inherent randomness in the photonic structures produces the unique angular signature.

Periodic and quasi-periodic *Morpho*-mimetic nanostructures were produced using microfabrication and soft-polymer replication techniques. These samples were physically and optically characterized in order to explore the relationship between the angular optical signature and randomization in the nanostructures. Both the periodic and quasi-periodic samples exhibited similar normal-incidence reflection spectra but differed dramatically in their angular optical responses. Periodic samples were shown to have angular dependence dominated by high-intensity specular and diffraction lines, while the quasi-periodic sample produced a two-lobe angular reflection pattern with minimal specular reflection. The measured angular signature of the reflected light of the quasi-periodic ridge ultrastructures followed closely the calculated diffraction lines for the double and triple periodic groupings found on the sample's surface. FDTD simulations offered further evidence that this response results from the quasi-random periodicity of the fabricated nanostructures. This result shows the importance of randomization in the *Morpho* butterfly ultrastructures for producing its unique angular response, especially the randomization in the period of ultrastructure ridges. Furthermore, the introduction of relatively minor randomization in the polymer samples produced a reflection distribution with a similar two-lobe reflection to that of the *M. rhetenor*, highlighting the sensitivity of the angular response

to the underlying order of the surface structures. Deliberate introduction of strongly randomized

features would allow for more precise control of the angular response

REFERENCES

[1]   Kumar R, Smith S, Mcneilan J, Keeton M, Sanders J, Talamo A, Bowman C and Xie Y Butterfly wing-Inspired Nanotechnology *The Nanobiotechnology Handbook* ed Y Xie (Boca Taon: CRC Press) pp 203–22

[2]   Zhang W, Gu J, Liu Q, Su H, Fan T and Zhang D 2014 Butterfly effects: novel functional materials inspired from the wings scales *Phys. Chem. Chem. Phys.* **16** 19767–80

[3]   Wang F, Meng Z, Xue F, Xue M, Lu W, Chen W, Wang Q and Wang Y 2014 Responsive photonic crystal for the sensing of environmental pollutants *Trends Environ. Anal. Chem.* **3**–**4** 1–6

[4]   Han Z, Niu S, Yang M, Mu Z, Li B, Zhang J, Ye J and Ren L 2014 Unparalleled sensitivity of photonic structures in butterfly wings *RSC Adv.* **4** 45214–9

[5]   Potyrailo R a., Bonam R K, Hartley J G, Starkey T a., Vukusic P, Vasudev M, Bunning T, Naik R R, Tang Z, Palacios M a., Larsen M, Le Tarte L a., Grande J C, Zhong S and Deng T 2015 Towards outperforming conventional sensor arrays with fabricated individual photonic vapour sensors inspired by Morpho butterflies *Nat. Commun.* **6** 7959

[6]   Yang X, Peng Z, Zuo H, Shi T and Liao G 2011 Using hierarchy architecture of Morpho butterfly scales for chemical sensing: Experiment and modeling *Sensors Actuators A Phys.* **167** 367–73

[7]   Lu T, Zhu S, Ma J, Lin J, Wang W, Pan H, Tian F, Zhang W and Zhang D 2015 Bioinspired Thermoresponsive Photonic Polymers with Hierarchical Structures and Their Unique Properties *Macromol. Rapid Commun.* **36** 1722–8

[8]   Pris A D, Utturkar Y, Surman C, Morris W G, Vert A, Zalyubovskiy S, Deng T, Ghiradella H T and Potyrailo R a. 2012 Towards high-speed imaging of infrared photons with bio-inspired nanoarchitectures *Nat. Photonics* **6** 195–200

[9]   Sveinbjörnsson B R, Weitekamp R a, Miyake G M, Xia Y, Atwater H a and Grubbs R H 2012 Rapid self-assembly of brush block copolymers to photonic crystals. *Proc. Natl. Acad. Sci. U. S. A.* **109** 14332–6

[10]   Miyake G M, Weitekamp R a, Piunova V a and Grubbs R H 2012 Synthesis of isocyanate-based brush block copolymers and their rapid self-assembly to infrared-reflecting photonic crystals. *J. Am. Chem. Soc.* **134** 14249–54

[11]   Fudouzi H and Sawada T 2006 Photonic rubber sheets with tunable color by elastic deformation. *Langmuir* **22** 1365–8

[12]   Ito T, Katsura C, Sugimoto H, Nakanishi E and Inomata K 2013 Strain-responsive structural colored elastomers by fixing colloidal crystal assembly. *Langmuir* **29** 13951–7

[13]   Kim S-H, Lee S Y, Yang S-M and Yi G-R 2011 Self-assembled colloidal structures for photonics *NPG Asia Mater.* **3** 25–33

[14]   Saito A, Miyamura Y, Ishikawa Y, Murase J, Akai-Kasaya M and Kuwahara Y 2009 Reproduction, mass production, and control of the Morpho butterfly's blue *Advanced*

Fabrication Technologies for Micro/Nano Optics and Photonics II vol 7205, ed T J Suleski, W V. Schoenfeld and J J Wang p 720506

[15]   Song B, Eom S C and Shin J H 2014 Disorder and broad-angle iridescence from Morpho-inspired structures. *Opt. Express* **22** 19386–400

[16]   Zhang Y, Dong B, Chen A, Liu X, Shi L and Zi J 2015 Using Cuttlefish Ink as an Additive to Produce -Non-iridescent Structural Colors of High Color Visibility *Adv. Mater.* **27** 4719–24

[17]   Huang J, Wang X and Wang Z L 2006 Controlled replication of butterfly wings for achieving tunable photonic properties. *Nano Lett.* **6** 2325–31

[18]   Kang S-H, Tai T-Y and Fang T-H 2010 Replication of butterfly wing microstructures using molding lithography *Curr. Appl. Phys.* **10** 625–30

[19]   Knez M, Nielsch K and Niinistö L 2007 Synthesis and Surface Engineering of Complex Nanostructures by Atomic Layer Deposition *Adv. Mater.* **19** 3425–38

[20]   Liu F, Liu Y, Huang L, Hu X, Dong B, Shi W, Xie Y and Ye X 2011 Replication of homologous optical and hydrophobic features by templating wings of butterflies Morpho menelaus *Opt. Commun.* **284** 2376–81

[21]   Lu T, Zhu S, Chen Z, Wang W, Zhang W and Zhang D 2016 Hierarchical photonic structured stimuli-responsive materials as high-performance colorimetric sensors *Nanoscale* **8** 10316–22

[22]   Watanabe K, Hoshino T, Kanda K, Haruyama Y, Kaito T and Matsui S 2005 Optical measurement and fabrication from a Morpho-butterfly-scale quasistructure by focused ion beam chemical vapor deposition *J. Vac. Sci. Technol. B Microelectron. Nanom. Struct.* **23** 570

[23]   Siddique R H, Diewald S, Leuthold J and Hölscher H 2013 Theoretical and experimental analysis of the structural pattern responsible for the iridescence of Morpho butterflies *Opt. Express* **21** 14351–61

[24]   Zhang S, Chen Y, Lu B, Liu J, Shao J and Xu C 2016 Lithographically generated 3D Lamella layers and its structural color *Nanoscale*

[25]   Siddique R H, Faisal A, Hünig R, Bartels C, Wacker I, Lemmer U and Hölscher H 2014 Utilizing laser interference lithography to fabricate hierarchical optical active nanostructures inspired by the blue Morpho butterfly *SPIE* vol 9187, ed R Liang and J A Shaw p 91870E

[26]   Aryal M, Ko D-H, Tumbleston J R, Gadisa A, Samulski E T and Lopez R 2012 Large area nanofabrication of butterfly wing's three dimensional ultrastructures *J. Vac. Sci. Technol. B Microelectron. Nanom. Struct.* **30** 61802

[27]   Kambe M, Zhu D and Kinoshita S 2011 Origin of retroreflection from a wing of the morpho butterfly *J. Phys. Soc. Japan* **80** 1–10

[28]   Okada N, Zhu D, Cai D, Cole J B, Kambe M and Kinoshita S 2012 Rendering Morpho

butterflies based on high accuracy nano-optical simulation *J. Opt.* **42** 25–36

[29]   Saito A, Yonezawa M, Murase J, Juodkazis S, Mizeikis V, Akai-Kasaya M and Kuwahara Y 2011 Numerical analysis on the optical role of nano-randomness on the Morpho butterfly's scale. *J. Nanosci. Nanotechnol.* **11** 2785–92

[30]   Kinoshita S, Yoshioka S and Miyazaki J 2008 Physics of structural colors *Reports Prog. Phys.* **71** 76401

[31]   Chung K, Yu S, Heo C-J, Shim J W, Yang S-M, Han M G, Lee H-S, Jin Y, Lee S Y, Park N and Shin J H 2012 Flexible, angle-independent, structural color reflectors inspired by morpho butterfly wings. *Adv. Mater.* **24** 2375–9

[32]   Saito A, Ishikawa Y, Miyamura Y, Akai-Kasaya M and Kuwahara Y 2007 Optimization of reproduced Morpho -blue coloration *SPIE Proceedings* vol 6767, ed H H Du and H Fudouzi p 676706

[33]   Boulenguez J, Berthier S and Leroy F 2012 Multiple scaled disorder in the photonic structure of Morpho rhetenor butterfly *Appl. Phys. A* **106** 1005–11

[34]   Forster J D, Noh H, Liew S F, Saranathan V, Schreck C F, Yang L, Park J C, Prum R O, Mochrie S G J, O'Hern C S, Cao H and Dufresne E R 2010 Biomimetic isotropic nanostructures for structural coloration *Adv. Mater.* **22** 2939

Chapter 3

Controlled Randomness through Direct Write Lithography and Surface Modification

3.1 Introduction

Periodic Morpho-like nanostructures were able to demonstrate enhanced reflection of specific wavelengths, similar to the butterfly. However, the angular reflection was dominated by the diffraction due to the strict periodicity of the structures. Introduction of randomness through capillary forces during drying, was able to partially destroy the periodicity of the structures, but the underlying order forced a certain amount of periodicity to remain. In order to obtain, an angular reflection similar to M. *rhentor* the strict periodicity needs to be removed from the biomimetic surface.

An interesting consequence of the integrated randomness found amongst the many periodic features in the ultrastructures of Morpho butterfly, is the angular spreading of light over a wide. The several random geometric features include differences in periodicity, height between ridges, random height changes along the structure ridges, the taper of the nanostructures and the

varying length of the branches.[1–4] Each of these can contribute to the overall characteristics of how the light spreads, the most informative way to measure and visualize these characteristics is the θ–φ measurement [5,6]. From here it can be effectively determined just how well the light for each visible wavelength is spread in angular space.

In this chapter, the effect of the various geometrical parameters of the biomimetic ultrastructure on the angular distribution of light is investigated. Typically, the two lobe θ–φ reflection is attributed to the asymmetrical off set of the Morpho ultrastructure.[1,6,7] Simulations have shown this to be a major contributor.[6,8–11] However, I will show that the two-lobe effect can be reproduced with the introduction of a symmetrical ultrastructure and that introduction of random spacing between each line can eliminate diffraction all together. While the staggered branches of the ultrastructure produce a two lobes refection close to the specular. Simulations show that careful manipulation of the geometries can imitate the angular spread without adding to the complexity of the fabrication process.

3.2 Previous attempts to randomize

There have been many attempts at biomimicry of the Morpho ultrastructure.[12] Investigation into the effects of various of different geometric features of been done via simulation[8–10,13,14] and experimentally[9,15–19]. In most cases, researchers attempted to mimic a single geometric feature without randomness, while other have sought to incorporate several random features found on the butterfly.[19].

3.3 Maskless Lithography

Maskless lithography is the direct use of focused radiation instead of projecting from or transmitting through a photomask. Although Interference lithography (IL) provides a large area

of exposure, with relatively short exposure times. IL is limited to producing only periodic structures. An alternative maskless lithographic approach is direct write lithography (DWL). Electron beam (ebeam) lithography is a well-known variant of DWL, and has been used for the most successful randomization efforts for biomimetic butterfly structures. However, ebeam lithography is plagued by slow through put and small areas of exposure. The need to directly control periodicity and duty cycle without dramatically increasing through put time required that an in house direct write laser lithography system be built. Direct write lithography uses a focused light source to write individual features of various sizes and spacing. Either the laser or the sample are moved via a two-axis raster system.

3.4 Experimental methods

3.4.1 Direct write lithography with nano stepper control

The direct write lithography system was built for under $6000. And consists of two major portions, the optical stack and the sample translation stack. The optical stack consists of a ccd camera to monitor the laser focus, 50/50 beam splitter, fiber optic input and collimation optics, and a 40x objective to focus the beam. The sample translation stack consists of   a Newport M426 optical stage to ensure the laser line remain straight along the sample and a JR Servo 8911 HV motor, which in controlled by an ardunio uno. On top of the optical stage is a Newport nanostepper stage (MFA-PPD) to control the spacing between each line and is controlled by a Newport ESP3000 controller. The sample stage with leveling knobs is connected to the nanostepper. The ardunio unit and the Newport controller are integrated using Matlab.
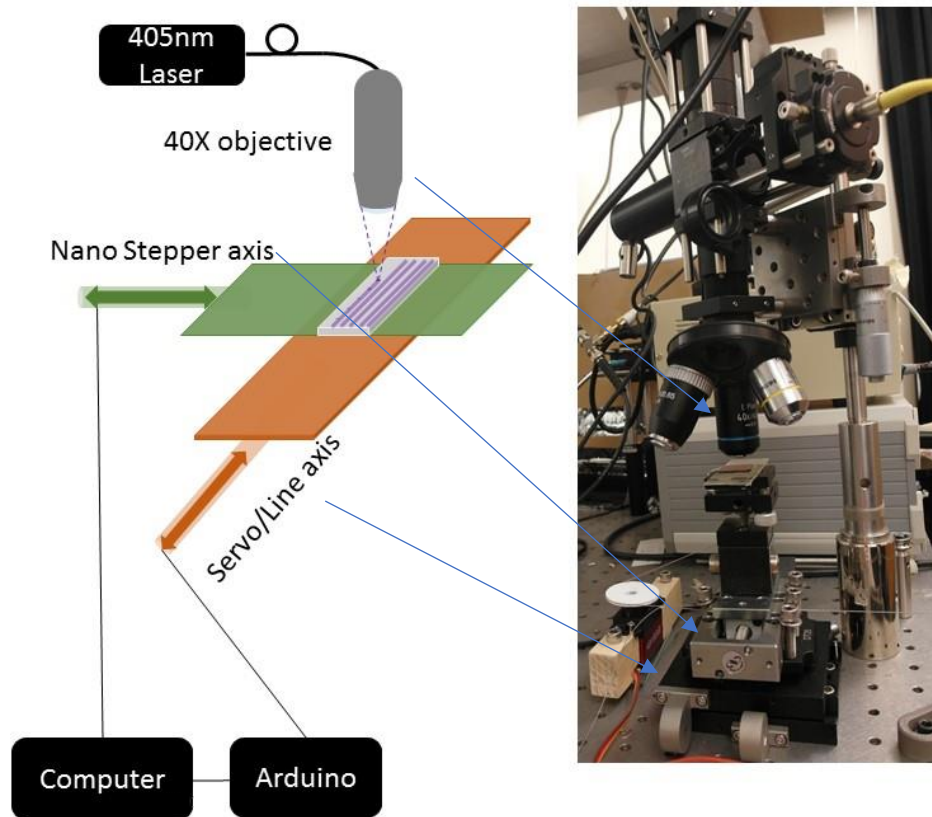
Figure 3.1 Direct Write Lithography System. Schematic showing the 40x objective focused onto a sample that is rastered by a Servo motor attached to an optical stage and a nanostepper to control line spacing. A photograph of the setup is included.

3.4.2 Chemical vapor deposition of multilayers

An Advanced Vacuum Vision 310 Plasma Enhanced Chemical Vapor Deposition (PECVD) System was used to deposit the MLs. Previously LPCVD was used to deposit the MLs, but control of the branch shape was desired so for this chapter, PECVD was chosen. LPCVD produces dense Si_3N_4 films that resist being etched by HF but with PECVD the density can be controlled by adjusting the deposition temperature. This allows for control of the "branch" shape.

3.4.3 Fabrication of hard master

Hard master fabrication differs slightly from that discussed in Chapter 3 due to the use of direct

write lithography. After deposition of the MLs, 100nm of Cr is deposited onto the ML substrate.
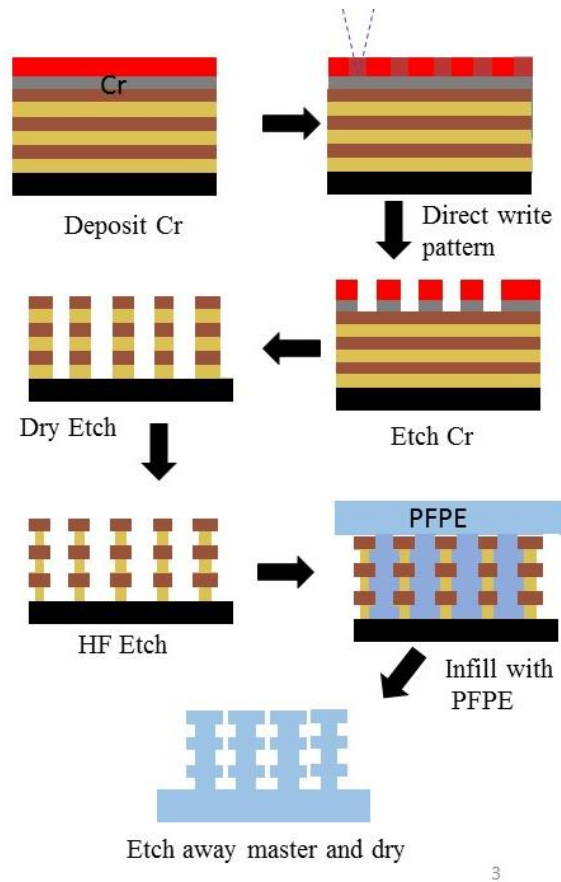
Figure 3.2 Direct write fabrication flow. MLs are first coated with Cr and photoresist. After exposure and development, the Cr is etched with a Cr etchant. The sample is then dried and wet etched. After hard master fabrication is complete the structures are infilled with PFPE-DMA and cured under UV light. The hard master is then etched away in 50% HF

After which, photoresist is spincast onto the substrate, using a 8:2dilution of S1811 photoresist

and thinner P (MicroChem Inc). The substrate is then leveled on the direct write system sample

stage. Each line is then written into the photo resist, the spacing between lines is determined by a

pre-generated matrix of distances. Line thickness was controlled by optimizing the line writing

speed, power, and development time. After development, the sample is cleaned via oxygen plasma to remove the resist residue from the exposed Cr. The sample is then dry etched in the DRIE with either the same recipe as in Section 2.4.2 or a low C4F8 (6 sccm) plasma. The DRIE recipe is altered between samples to either etch a straight or tapered trunk. After dry etching the non-periodic samples, fabrication continues in a similar fashion to Section 2.4.4.

3.4.4 Predetermining line spacing

Matrices of distances, representing the successive distance between laser written lines, were populated before writing onto each new sample. Line distributions were separated into two different groups. The first group was a normal distributions of random distance centered at 2.5 µm. The second group was populated with distances that were uniformly distributed and was also centered at 2.5 µm. Distribution with different standard deviations or maximum/minima were used to determine what level of randomization is required to completely disrupt the periodicity and destroy the diffraction. Uniform distribution maxima/minima increased by 500 nm from 2. 5 µm ±0.5 to 2.5 µm±1.5. For normal distributions, a standard deviation was chosen that would match the uniform distribution.

3.5 Results and Discussion

3.5.1 Disrupting the periodicity

Although the Morpho butterfly disrupts its periodicities through multiple features, a straight forward approach to mimicking this affect is by removing the periodicity completely. A major drawback to this direct approach, as I will show, is the need to have large gaps between nanostructures, thus decreasing the reflected intensity. It is important then to know the minimum randomness required to disrupt the periodicity and if how the structures are distributed matters.

3.5.2 Uniform random distribution
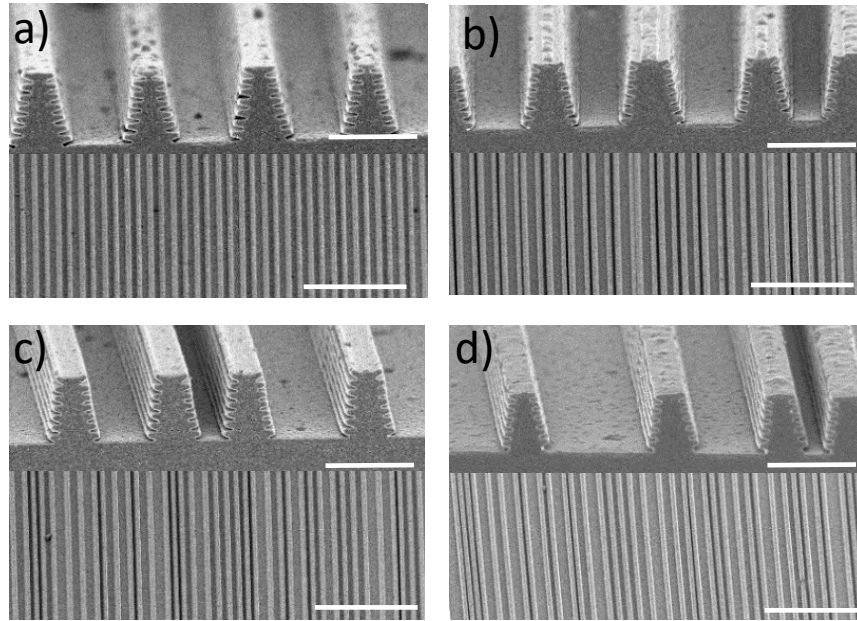
Figure 3.3 SEM aerial and cross-section micrographs, of samples with variously spaced structures. A perfectly periodic sample (a). Samples with structure lines that have been uniformly distributed, 2.5±0.5 μm (b), 2.5±1 μm (c), 2.5±0.5 μm (d) Scale bars: Cross-section 2 μm and Aerial: 25 μm

SEM micrographs of typical uniformly random nanostructures are shown in Figure 3.3. Aerial images of the different distributions help to visualize the difference in line spacing as the width of the distribution increases. Cross sections of the various distributions reveal a similar structure, with ~1 μm trunk bases, a 10 degree taper and 7 "branch" ML. The structure spacing ranged from perfectly periodic to 2.5 μm ± 1.5 μm.

Uniform distributions were produced within a set range. This range was increased until diffraction arcs could no longer be identified on the θ-ϕ graphs. Shown in Figure 4.4a-d periodic and uniformly random θ-ϕ graphs are compared. The introduction of only slight randomness (2.5±.5 microns) significantly destroys the diffraction, however the 1st order diffraction arc, near the specular reflection line is still visible. Increasing the randomness further only slightly

disruption the 1st order diffraction. A further increase to ±1.5um completely destroys any indication of diffraction arcs but the two high intensity lobs are still visible and are therefore not the results of diffraction.
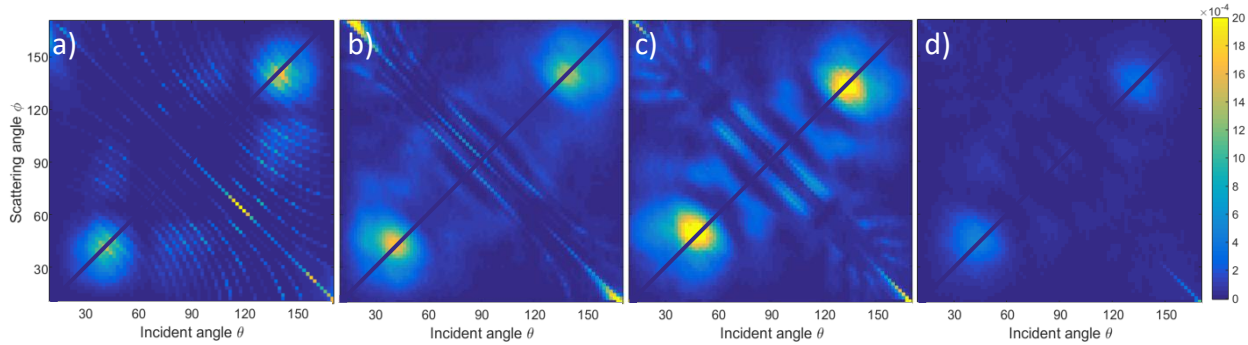
Figure 3.4 Double angle measurements for various uniform distribution periodicities.
(a) Periodic, 2.5 µm (b) uniform, 2.5 µm ±0.5 (c) uniform, 2.5 µm ±1 (d) uniform 2.5 µm ±1.5

Typically the two high intensity lobes observed from the butterfly have been associated with the slight off set between the branches on either side of the morpho nanostructure.[5,20] Here the two lobes are produced with a symmetrical biomimetic structures. Although a significant difference between reflection lobes produced by the butterfly and the lobes seen in Figure 3.4, is there location in angular space. The biomimetic structures produce lobes at angles far from normal incidence, while the butterfly produces two lobes just off of normal incidence line (Figure 3.4(b-d)). FDTD simulations indicate that the two-lobe reflection for the biomimetic structures results from the introduction of trunk in a multilayer structure. Figure 3.5 shows the progression of no trunk to a trunk and the appearance of the two-lobe reflection. Nanostructures in Chapter 3 showed no such reflections but this is due to the perfect periodicity produced by IL, whereas the periodic structures produced with DWL vary along each ridge and are not perfectly periodic. This allows for the θ-ϕ reflection to be less dominated by diffraction.
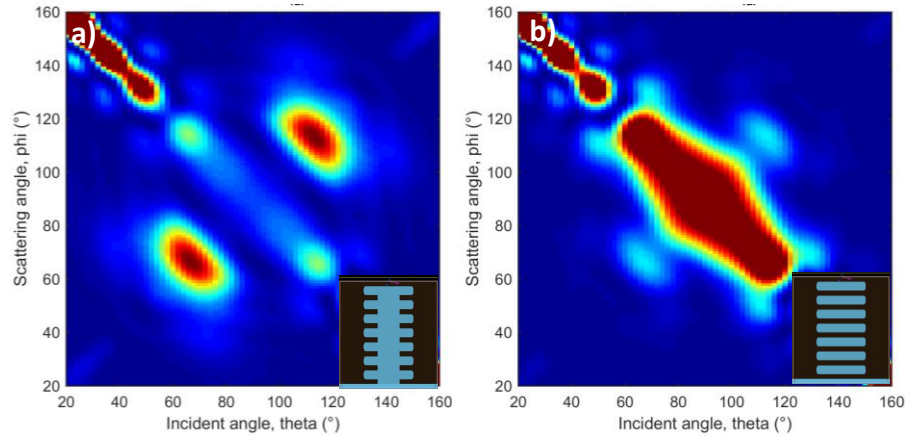
Figure 3.5 FDTD simulation of a multilayer stake with and without a "trunk". The presence of the trunk produces a two lobe back reflection.

3.5.3 Normal random Distribution

Normal distributed nanostructured lines were produced in similar fashion to the uniform distributed lines. In this case a standard deviation was chosen such that it would be similar to the uniform distribution ranges. Figure 3.6 shows the θ-ϕ measurements of the normally distributed lines of with distributions equivalent to 2.5 µm $\pm$ 0.5 and 2.5 µm $\pm$1.5 . These samples show a similar two lobe reflection at wide angles. Comparison of the θ-ϕ measurements between the uniformly and normally disturbed samples shows similar results but even with equivalent distribution to 2.5 µm $\pm$ 1.5 some diffraction still remains. For this reason, during the remainder of the chapter only uniformly distributed samples will be used.
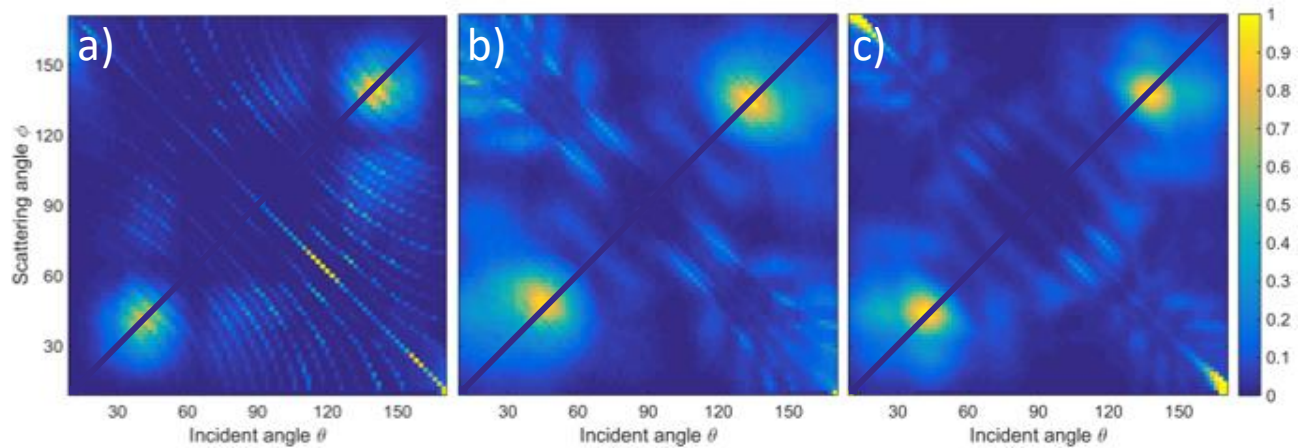
Figure 3.6 Normal distribution θ-ϕ graphs. Normal distributions with standard deviations equivalent to the variance of the uniform distribution. (a) periodic, (b) uniform, 2.5 μm ±0.5 (c) uniform 2.5 μm ±1.5

3.5.4 Addition of Chopper

The introduction of randomness over 50% of the median spacing can destroy the periodicity, it also results in a loss of reflection intensity (Figure 3.4d). However, the butterfly provides an answer for this. As seen in Figure 1.5a the height randomly changes and when viewed from above creates disruptions along the length of each row. Adding disruptions along the ridge has been shown to be beneficial for spreading light over a large angular range. [19]This can be mimicked with the laser writing setup by introducing an optical chopper in the path of the beam. The optical chopper blade will temporally block the writing beam creating disruption along the each line. Figure 3.6a shows the resultant structure and aerial SEM of a uniformly distribution lines. Figure 3.6b-d show the angular spread of light of a uniformly random sample (2.5um ±.05) with the addition of 1 kHz optical chopping using a 10 slot optical chopper blade. The addition of the optical chopping resulted in a complete loss of order and a similar θ-ϕ graph as the ±1.5 um sample (Figure 3.6d). The intensity of   the two lobes is as much as four times

the ±1.5 um sample. The use of a chopper blade with greater number of slots will result in a similar effect with an increased intensity. This has shown that the diffraction can be sufficiently disrupted by controlling the spacing between each line, however as carefully examination of the θ-ϕ graphs will indicate that these high intensity spots occur at large angles and are concentrated over a small angular range.
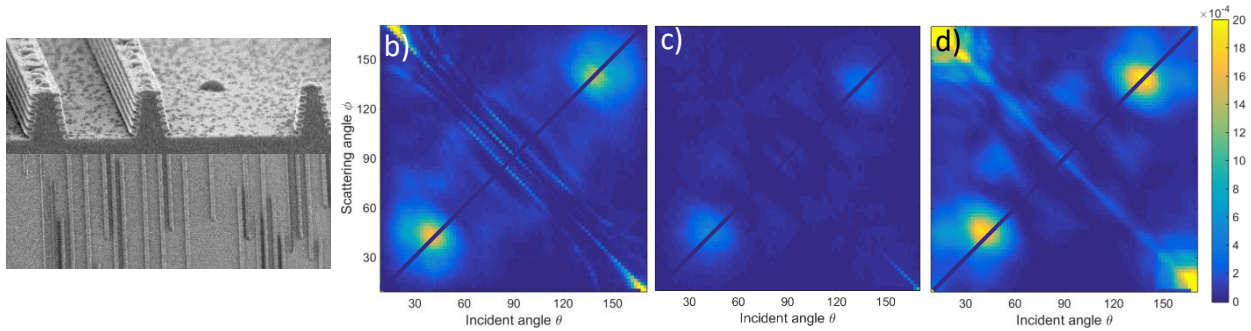
Figure 3.7 Uniform distributions with chopper. Uniformly distributed lines were fabricated with the addition of a chopper blade running at 1kHz to break up the nanostructured lines. (a) SEM cross section and aerial micrograph of a shopper fabricated sample. (b) uniform, 2.5 µm ±0.5 (c) uniform, 2.5 µm ±1.5 (d) uniform 2.5 µm ±0.5 plus chopper. The chopper sample is able to have high intensity reflection and destroy reflection without increase the spacing between lines.

3.5.5 FDTD Simulations: controlling the angular spread

Since fabricating asymmetric nanostructure would be difficult with traditional microfabrication techniques. FDTD simulations were used in conjunction with experimental results to guide the fabrication routes. Understanding what features can contribute to the unique reflection seen in the butterfly and biomimetic structures will aid in fabricating a biomimetic structure with similar optical properties.

3.5.5.1 Effects of branch asymmetry

It has been shown previously that the branch off set between the two sides of the Morpho nanostructure can produce a two lobe reflection in angular space.[5,6]In Figure 3.7 the θ-ϕ

58

reflections of a mulilayer structures sans a "trunk" , with "branches" that are increasingly off set.

Figure 4.7a shows the reflection of a multilayer ridge, with no offset, as it would be expected, the

light is primarily speculary reflected. Simulation over multiple wavelengths show that the

reflection shifts along the specular reflection line (mirror line), in an iridescent fashion. (See

appendix A3)   As the branches are offset by 50% of the branch thickness (Figure 3.7b) the

reflection begins to shift off the mirror line, continually increasing the offset (Figure 3.7c-d)

leads to complete back reflection and formation of the iconic two lobe signature produced by the

butterfly. Well this can be used to explain the observations from the butterfly, it fails to explain

the high intensity spot measured in the uniformly random sample in the previous sections.
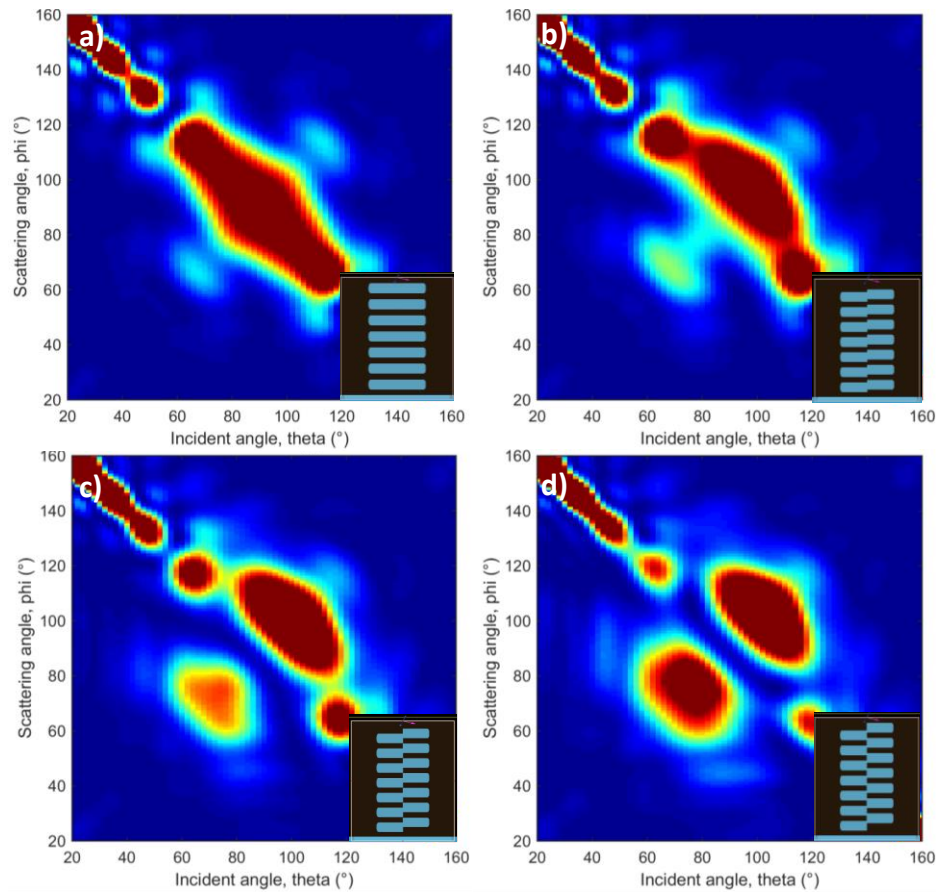
Figure 3.8 FDTD simulations comparing the effect of offset branches. The branch offset is
gradually increased from no offset (a) to 50 nm (b), 75 nm (c) and 100 nm (d). (d) represents the

offset found on the Morpho butterfly, the branch completely offset by the thickness of the branches.

3.5.5.2 Effects of branch shape

In order to understand the origin of the high intensity spots seen experimentally, a represented structure from the sample surface was simulated. A cross section of the structure was traced and simulated, revealing similar θ-ϕ graphs (Figure 4.8a) seen on the uniformly distribution samples (Figure 3.4). The structure seemingly has asymmetric features, testing to see if this was the source of the θ-ϕ signature, one half of the structure was mirrored to produce a symmetric structure (Figure 3.8b inset). This shows no significant change in the θ-ϕ measurement, besides balancing the intensities of the two lobes. The shape of the branches was then probed as a possible source by simulating a similar structure but with straight branches (Figure 3.8c Inset) instead of irregularly shape branches. Although the θ-ϕ signature shows a similar reflection. Further testing revealed that these lobes were resulting from having a multilayer structure separated by a "trunk" feature.
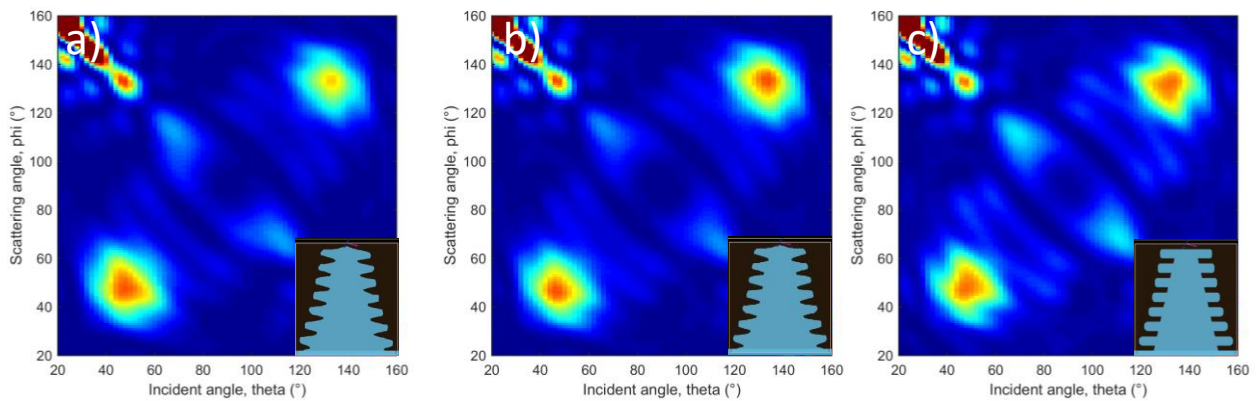
Figure 3.9 Simulation of original biomimetic structure and determination of the effect of branch shape. (a) the nanostructure found on the surface of the uniformly distributed samples. The theta-phi graph matches the experimental result. (b) A symmetrized structure, theta-phi intensities are balanced but the two-lobe feature is still present. (c) A straight branch model is simulated to determine if the branch shape is producing the reflection. The only difference is a slight increase in specular reflection.

3.5.5.3 Effect of trunk size

Well it is interesting that the two-lobe reflection can be produced by simply having a multilayer ridge structure, the lobes are at oblique angles and produces samples where the color is not easily viewed. The "trunk" thickness of the biomimetic structures (~1μm) is much thicker than the "trunk" of the Morpho nanostructures (~300nm).[1,12] θ-ϕ simulations were performed for a thick "trunk" and a thin trunk with similar branch lengths. Shown in Figure 3.9(a-b) the thick trunk has reflection lobes in similar angular location as the experimental, as well as the inward curving feature near the mirror line. While the thin "trunk" simulation shows a significant angular shift of the location of the two lobes, of approximately $25°$ in the scattering angle. Increasing the branch length of the thin trunk structure (Figure 3.9c) can further enhance this effect, while also spreading the lobe out over a wider angular range. Instead of decreasing the "trunk" thickness a taper was added, shown in Figure 3.9d, the base of the "trunk" remained at 1 μm while the top of the trunk is 300 nm. This results in a lower intensity by similar angular location of the two lobes. Multiple wavelength θ-ϕ simulations for each of the structures shown in figure 4.9 can be found in Appendix A2 and A4.
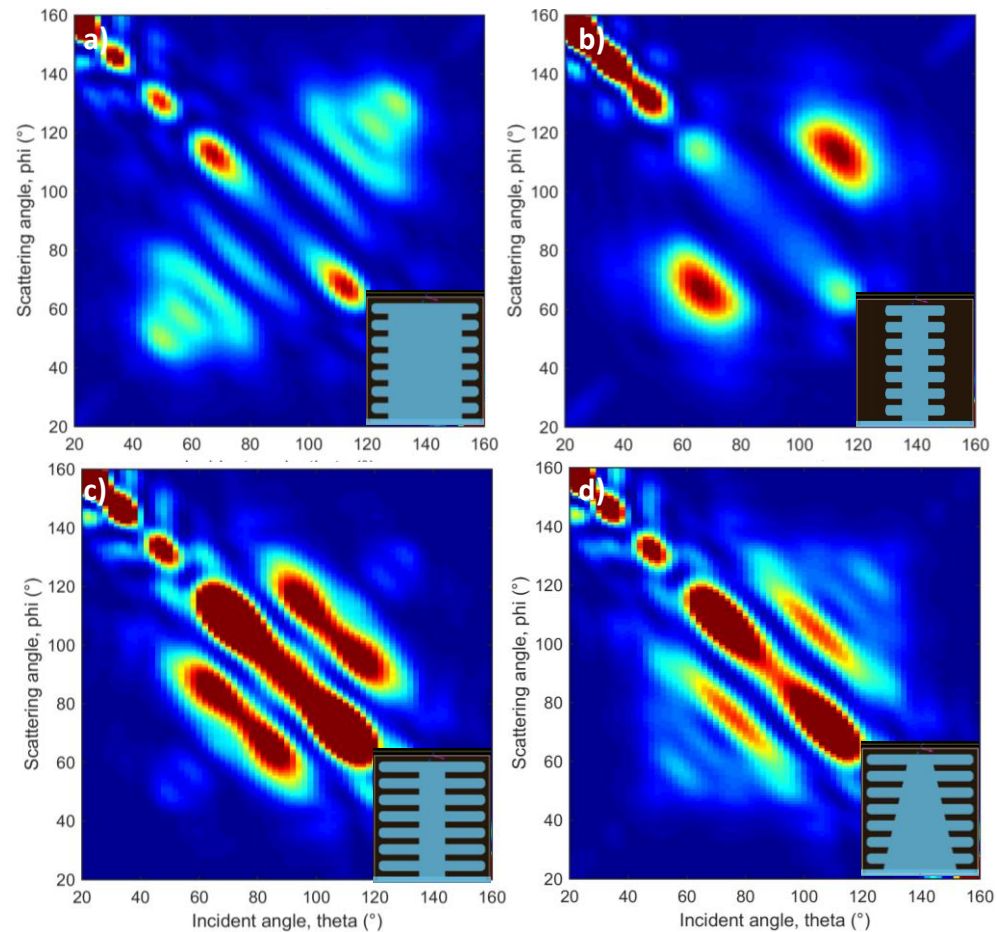
Figure 3.10 FDTD simulation exploring the effect of trunk shape and thickness. (a) and (b) show the difference in angular reflection of a fat and thin trunk. As the trunk thickness decreases the two-lobe reflection spots shift toward shallower angles. Increase branch length, with a thin trunk results in further shifting of the lobes location. Adding a 15˚ taper to the thick trunk results in similar reflections.

4.5.5.4 Effect of branch taper

Another approach that was explored, is tapering the length of the branches rather than the trunk, Shown in Figure 3.10 the "trunk" remains thin but the branches gradually decrease in length farther up the "trunk". θ-ϕ measurements revealed 480 nm wavelengths spreading out over a large angular range and then coalescing close to the mirror line. Before beginning to

dissipate after 520 nm. This structure shows similar angular features as the butterfly without the

need for staggered branches.
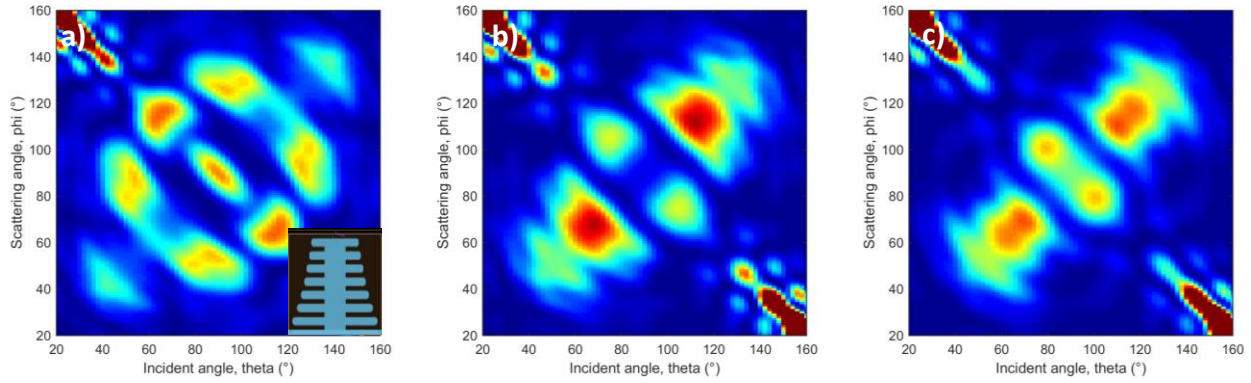
Figure 3.11 An ideal structure. FDTD simulations of a thin trunk structure with branches that taper off in length from the bottom branch to the top. θ-ϕ simulations show a strong two lobe reflation with light spreading over a large angular range. (a) 480 nm, (b) 500 nm, and (c) 520 nm. Inset: 2D structure used to simulate these θ-ϕ graphs

3.5 Conclusion

A direct write lithograph system was designed and built to facilitate the fabrication of

non-periodic biomimetic structures. The amount of randomness needed to disrupt the periodicity

was quantified. Uniform and normal spacing distributions theta-phi reflections were compared,

and found to differ slightly. The uniform distribution was able to destroy periodicity with 2.5 μm

± 1.5, although the intensity loss was measurable. While the normal distribution still showed

diffraction at comparable standard deviation. Interestingly, the samples showed two high

intensity lobes like the butterfly, but at oblique angles. The lobe were shown to be the result of

the multilayer ridge with a "trunk" feature. FDTD simulations were used to determine a

fabrication path that could shift the two lobe reflections to more shallow angles. Simulations

revealed that the "trunk" thickness and shape can affect the location of the lobed in angular.

Finally, a slight taper to the successive branches is able to produce a similar reflection to the

Morpho butterfly and is identified as the most ideal structure to fabricat

REFERENCES

[1]   Kinoshita S, Yoshioka S and Miyazaki J 2008 Physics of structural colors *Reports Prog. Phys.* **71** 76401

[2]   Kinoshita S, Yoshioka S and Kawagoe K 2002 Mechanisms of structural colour in the Morpho butterfly: cooperation of regularity and irregularity in an iridescent scale. *Proc. Biol. Sci.* **269** 1417–21

[3]   Vukusic P, Sambles J R, Lawrence C R and Wootton R J 1999 Quantified interference and diffraction in single Morpho butterfly scales *Proc. R. Soc. B Biol. Sci.* **266** 1403

[4]   Kinoshita S, Yoshioka S, Fujii Y and OKAMOTO N 2002 Photophysics of structural color in the Morpho butterflies *Forma* 103–21

[5]   Kambe M, Zhu D and Kinoshita S 2011 Origin of retroreflection from a wing of the morpho butterfly *J. Phys. Soc. Japan* **80** 1–10

[6]   Okada N, Zhu D, Cai D, Cole J B, Kambe M and Kinoshita S 2012 Rendering Morpho butterflies based on high accuracy nano-optical simulation *J. Opt.* **42** 25–36

[7]   Vukusic P and Stavenga D G 2009 Physical methods for investigating structural colours in biological systems. *J. R. Soc. Interface* **6 Suppl 2** S133-48

[8]   Steindorfer M a, Schmidt V, Belegratis M, Stadlober B and Krenn J R 2012 Detailed simulation of structural color generation inspired by the Morpho butterfly. *Opt. Express* **20** 21485–94

[9]   Siddique R H, Diewald S, Leuthold J and Hölscher H 2013 Theoretical and experimental analysis of the structural pattern responsible for the iridescence of Morpho butterflies *Opt. Express* **21** 14351–61

[10]   Saito A, Yonezawa M, Murase J, Juodkazis S, Mizeikis V, Akai-Kasaya M and Kuwahara Y 2011 Numerical analysis on the optical role of nano-randomness on the Morpho butterfly's scale. *J. Nanosci. Nanotechnol.* **11** 2785–92

[11]   Zhu D, Kinoshita S, Cai D and Cole J B 2009 Investigation of structural colors in Morpho butterflies using the nonstandard-finite-difference time-domain method: Effects of alternately stacked shelves and ridge density *Phys. Rev. E - Stat. Nonlinear, Soft Matter Phys.* **80** 1–12

[12]   Fu Y, Tippets C A, Donev E U and Lopez R 2016 Structural colors: from natural to artificial systems *Wiley Interdiscip. Rev. Nanomedicine Nanobiotechnology* **8** 758–75

[13]   Banerjee S, Cole J B and Yatagai T 2007 Colour characterization of a Morpho butterfly wing-scale using a high accuracy nonstandard finite-difference time-domain method. *Micron* **38** 97–103

[14]   Wang W, Zhang W, Gu J, Liu Q, Deng T, Zhang D and Lin H-Q 2013 Design of a structure with low incident and viewing angle dependence inspired by Morpho butterflies. *Sci. Rep.* **3** 3427

[15]   Siddique R H, Faisal A, Hünig R, Bartels C, Wacker I, Lemmer U and Hölscher H 2014 Utilizing laser interference lithography to fabricate hierarchical optical active nanostructures inspired by the blue Morpho butterfly *SPIE* vol 9187, ed R Liang and J A Shaw p 91870E

[16]   Tippets C a, Fu Y, Jackson A-M, Donev E U and Lopez R 2016 Reproduction and optical analysis of *Morpho* -inspired polymeric nanostructures *J. Opt.* **18** 65105

[17]   Aryal M, Ko D-H, Tumbleston J R, Gadisa A, Samulski E T and Lopez R 2012 Large area nanofabrication of butterfly wing's three dimensional ultrastructures *J. Vac. Sci. Technol. B Microelectron. Nanom. Struct.* **30** 61802

[18]   Chung K, Yu S, Heo C-J, Shim J W, Yang S-M, Han M G, Lee H-S, Jin Y, Lee S Y, Park N and Shin J H 2012 Flexible, angle-independent, structural color reflectors inspired by morpho butterfly wings. *Adv. Mater.* **24** 2375–9

[19]   Saito A, Miyamura Y, Ishikawa Y, Murase J, Akai-Kasaya M and Kuwahara Y 2009 Reproduction, Mass-production, and Control of the Morpho-butterfly's Blue *Advanced Fabrication Technologies for Micro/Nano Optics and Photonics II* vol 7205, ed T J Suleski, W V. Schoenfeld and J J Wang pp 720506-720506–9

[20]   Lee R T and Smith G S 2009 Detailed electromagnetic simulation for the structural color of butterfly wings. *Appl. Opt.* **48** 4177–90

Chapter 4

Dynamic Optical Grating Accessed by Shape Memory Polymers

4.1 Introduction

Reversible shape memory polymers offer an interesting route to fabricating active optical components. Photonic shapes that can shift freely between two or more other shapes could reduce the need for multiple optics inside a single apparatus. In this chapter I will discuss a proof of concept experiment using the Poly(octylene adipate) a polycrystalline polymer which has been shown to exhibit reversible shape memory.[1] Molding the polymer using soft lithography techniques and monitoring the diffraction signal provide evidence of the viability of a RSM optical element.

4.2 Introduction to Soft Lithography and Optical Applications

Soft lithography is a family of techniques where by polymeric stamps are used to transfer micro- or nano-sized patterns. Usually a elastomer stamp is used and applications include print transferring,[2] phase shifting lithography,[3] mechanical sectioning[4] and molding.[5] Molding offers an interesting approach to enhance traditional microfabrication techniques that tend to be laborious and expensive. Soft lithography allows for the rapid replication of a single

hard master, and the subsequent soft master can be used for additional replications, greatly reducing the time and cost of the nanofabrication and providing a quick transition to commercialization. A key advantage of soft lithography is that its resolution is limited only by van der Waals contact and the inherent roughness of matter.[6] Where as traditional fabrication techniques are scattering and diffraction limited. This opens up a wide varied of micro- and nanostructures that could be replicated by soft lithography but would not be achievable through traditional means

Polydimethylsiloxane (PDMS) is the most common material used for the elastomeric stamps, and offers several advantages.[6] However, depending on the application, other materials might be more beneficial. Within the last decade, perfluoropolyethes (PFPE) have gained interest as a soft lithography mold material. PFPE has several advantages such as, low Young's modulus, low surface energy, minimal swelling and low toxicity. First pioneered by DeSimone et al., pattering Replication in Nonwetting Templates (PRINT) ,[7] which uses PFPE molds, has been used in the fabrication of periodic grating on with various materials[8,9], organic solar cells[8], drug delivery[10], biomimicry of red blood cells[11] and for liquid crystal displays[12]. The successful use of PFPE as a soft lithography material, and its low surface energy make it a good candidate for replicating optical gratings from SMP materials.

4.2.1 Shape Active Optics via Soft Lithography

Soft lithography has been used to produce shape active photonic shapes, with polydimethylsiloxane (PDMS).[13–16] While these were able to show interesting optical response, they are limited by the need for continuous strain in order to maintain the optical response. Shape memory polymer offer the ability to transition between two or more shapes.[17]

68

Shape memory polymers have been shown to be able to replicate photonic structure.[18] In this study, optical blazed gratings and micro pyramids were able to switch between a flattened and structured states. Well this showed the applicability of shape memory polymers as optical components, the application is limited by the single use shapeshifting that requires the reprograming after each use. This limitation can be overcome through the use of RSM materials, which provides a pathway for application of these SMP optical components.

4.3 Experimental Methods

4.3.1 Materials

Poly(octylene adipate) (POA), a semi-crystaline polymer, was used as a representative RSM polymer and was first reported by Zhou et al.[1]. The chemical structure of end-functionalized POA is shown in Fig. 4.2. In order to utilize the best RSM behavior of POA, POA was synthesized with a number average degree of polymerization (DP) of $n = 13$ ($M_n = 3500$ g/mol), which is known to exhibit significant shape reversibility.[1] For this experiment, the synthesis was improved to decrease reaction times and allow for more accurate control of the molecular weight. Condensation polymerization between adipoyl chloride and octylene diol was used to produce POA instead of adipic acid and octylene diol as reported previously.[1] This resulted in a higher T_m 58 °C compared to previous synthesis which has T_m around 50 °C.
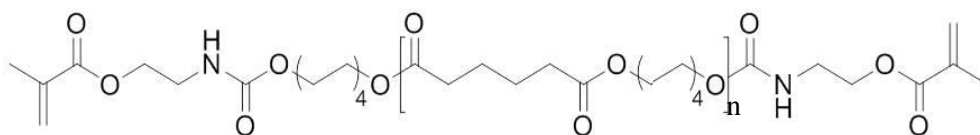
Figure 4.1 Chemical Structure of Poly(octylene adipate)

4.3.2 Synthesis of PFPE

1g (1 mmol) perfluoropolyether (PFPE) (Solvay Solexis) was dissolved in 50 mL dry methylene chloride. Triethylamine (2 mmol, 0.2 g) was dropwise added to the solution at 0 °C. 2-Isocyanatoethyl methacrylate (2.1 mmol, 0.33 g) (TCI America) was added to the solution and stirred overnight at room temperature. The solution was filtered, and remaining solvent was removed by rotary evaporation. The product was purified by washing with toluene, centrifugation and then drying *in vacuo* at room temperature

4.3.2 Fabrication of PFPE Soft Masters

The PFPE soft master was fabricated by first pouring liquid PFPE-DMA over a silicon grating that was fabricated using standard microfabrication techniques. A PET backing, treated with a proprietary coating for PFPE adhesion, is placed over the mold and all air bubbles are removed. The Si mold is then placed in an nitrogen atmosphere and cured under a 365 nm lamp. After curing the PFPE grating is peeled from the Si master (pitch 750 nm, ridge height 250 nm, ridge width 250 nm).

4.3.3 Fabrication of SMP gratings
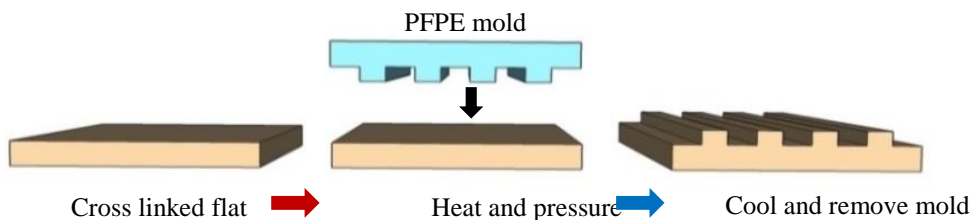
Figure 4.2 The SMP molding process: a glass slide is used to cure an optically flat surface of poly(octylene adipate). A 750 nm pitch perflouropolyether (PFPE) grating is used as a mold to emboss the heated flat surface. After cooling the mold is removed and the grating structure remains on the SMP surface

The two step procedure is shown in Figure 4.2. First, the POA is mixed with 10 wt% $CHCl_3$ and 1 wt% 2,2-diethoxyacetophenone (DEAP). The mixture was then injected into a Teflon mold, covered with a glass slide and crosslinked with 365 nm UV light for 5 minutes. This results in an optically flat RSM substrate as the primary shape. The substrate was annealed at 70 °C overnight to extract the remaining solvent and thermal history. Next, the substrate was heated to 70 °C and the optically flat surface was pressed against the perfluoropolyether (PFPE) grating followed by quenching in an ice bath. After separation of the substrate and the PFPE mold, the surface was in its secondary grating shape, which accurately replicated the PFPE grating.

5.3.4 Atomic Force Microscopy and Height Analysis

In situ Atomic Force Microscopy (AFM) was used to determine the change in surface topography as the RSM substrate was cycled. An Asylum Research MFP3D Atomic Force Microscope was used to monitor the sample.

The ridge height was calculated using ImageJ software package. A representative cross-sectional area was chosen to be averaged and from this area 180 line profiles were averaged and compiled, as shown in Figure 4.3a. The average cross-sectional graph was then baseline corrected, the resulting profile is shown in Figure 4.3b.
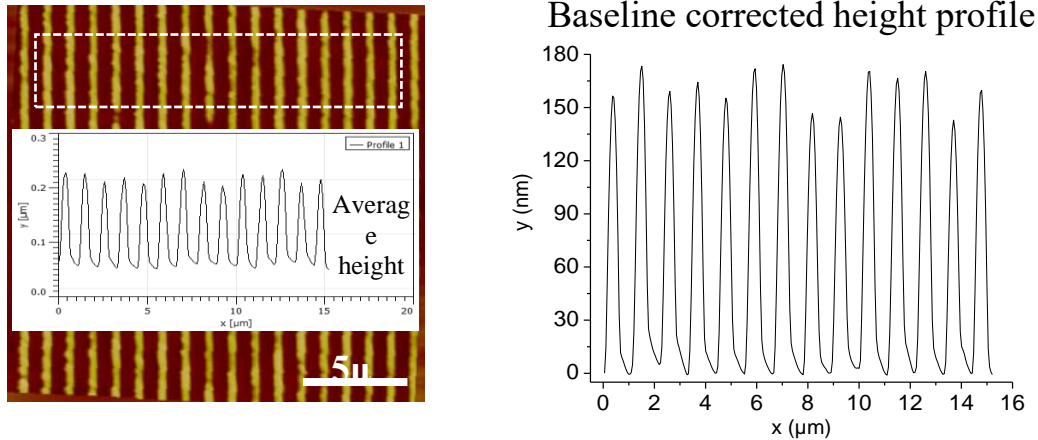
Figure 4.3 Average ridge height calculation. First a A cross-sectional area was chosen to be averaged and from this area 180 line profiles are averaged. Then the profile is baseline corrected

4.3.5 Optical measurement

Optical measurements of the grating diffraction intensity were taken using the set up in Figure 4.4. The RSM grating was illuminated by a 633 nm He-Ne laser, at an incident angle of 5° with respect to the sample normal. The 750 nm grating was specifically chosen, so that there would be sufficient angular space between the specular reflection (M = 0) and the M = +1 diffraction order. This allowed for the 1st order diffraction to be measured independently of the specular and 2nd order diffraction. For this measurement, a planar diffuse Silicon photodiode (United Detector Technologies) with a spectral sensitivity from 400-1100 nm and a responsivity of ~.4 A/W at 633 nm was used to monitor the intensity of the diffraction mode and the intensity of the incident beam in order to correct for power fluctuations. The temperature of the RSM sample was controlled using a thermoelectric stage. The relative intensity for each measurement was calculated by normalizing the diffracted beam intensity with the incident beam intensity.
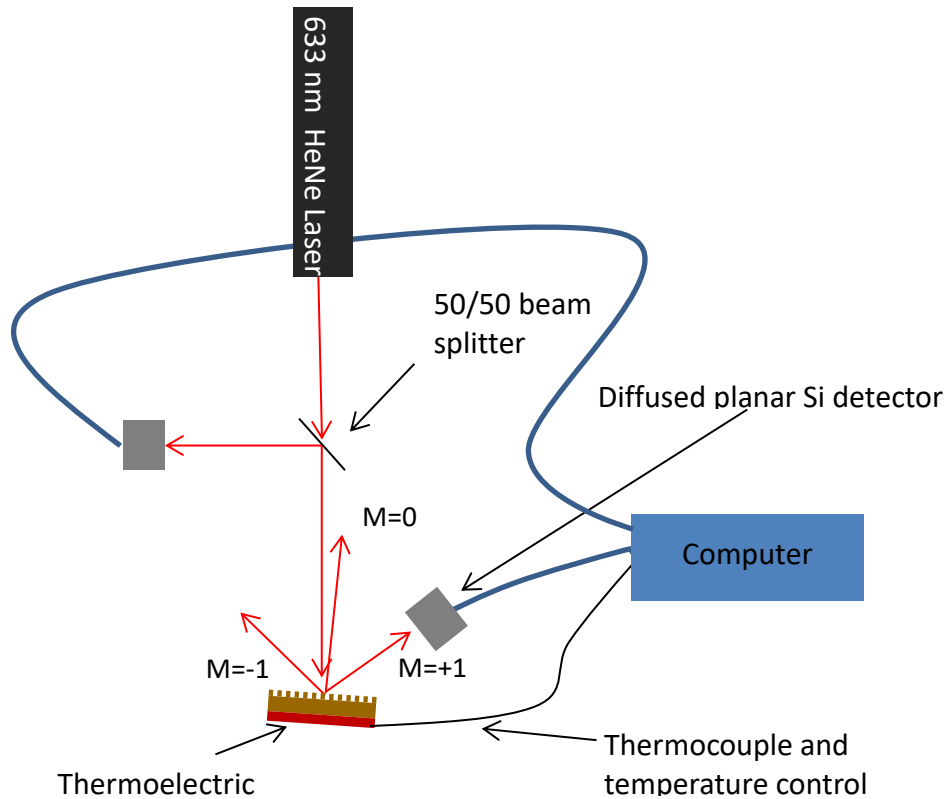
Figure 4.4 Optical measurement set up, for measuring the diffraction intensity. The incident beam is first, passed through a 50/50 beam splitter, in order to monitor the incident power. The beam then impinges on the surface of the SMP grating. The resultant first order diffraction intensity is monitored via a diffused planar Si detector. The SMP grating is placed in contact with the thermoelectric stage and the temperature of the sample was controlled via Labview and monitored with a thermocouple

4.4 Results and Discussion

4.4.1 POA Operational Temperature Range

If substrate temperature is increased beyond T_m, a sufficient amount of the crystalline scaffold will melt, which causes the grating to return toward its flat primary shape. Within the range of $T_p < T_m$ enough crystallites reaming to facilitate the recovery of the embossed secondary shape upon cooling, though self-seeded crystallization. The diffraction efficiency shows excellent reversibility and good repeatability over many cycles with in this range.

Therefore an optimal temperature regime is set forth, with T_m being the upper temperature limit and lowest grating height accessible. Referring to the regime, will allow for planning of the proper programing protocol to achieve the desired photonic actuation

The experimental temperature regime for the POA grating was determined by A differential scanning calorimetry. A thermogram of a POA sample is shown in Figure 4.5. The DSC indicates that the onset melting occurs at 38 ˚C and the melting peak (T_m) at 56 ˚C. The onset of crystallization occurs at 37 ˚C. As long as 50% of the crystallites remain the RSM process can occur. From this it can be concluded that the RSM temperature regime occurs between 37 ˚C and 56 ˚C.
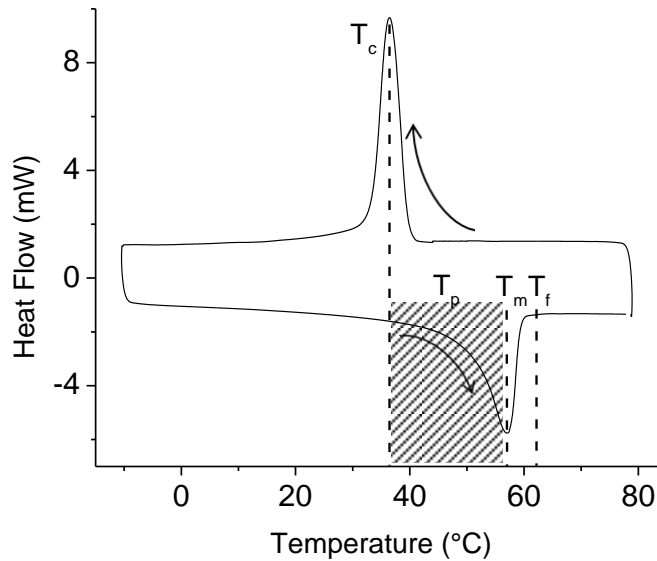
Figure 4.5 A differential scanning calorimetry (DSC) thermogram of a crosslinked POA sample indicates the temperature range of partial melting temperatures (T_p ,hatched region), the melting peak (T_m = 56 °C), the temperature of complete melting (T_f = 64 °C), and the crystallization peak (T_c = 37 °C) (arrows indicate ramping direction).

4.4.2 Bulk Reversibility

For this study the bulk reversibility was determined using experimental conditions rather the optimal conditions that would result in high reversibility. Figure 4.6 shows a tensile test using dynamic mechanical analysis (DMA) of poly(octylene adipate) as its heated and cooled under experimental conditions. The bulk reversibility under these conditions is 41%, as measured by the ratio of recovered strain over programed strain. Optimal conditions require that the sample be cooled to 10˚ C. However, this caused condensation to form on the surface of the samples which produced erroneous optical signals. Thus, experimental temperatures were changed so that samples were cooled room temperature.
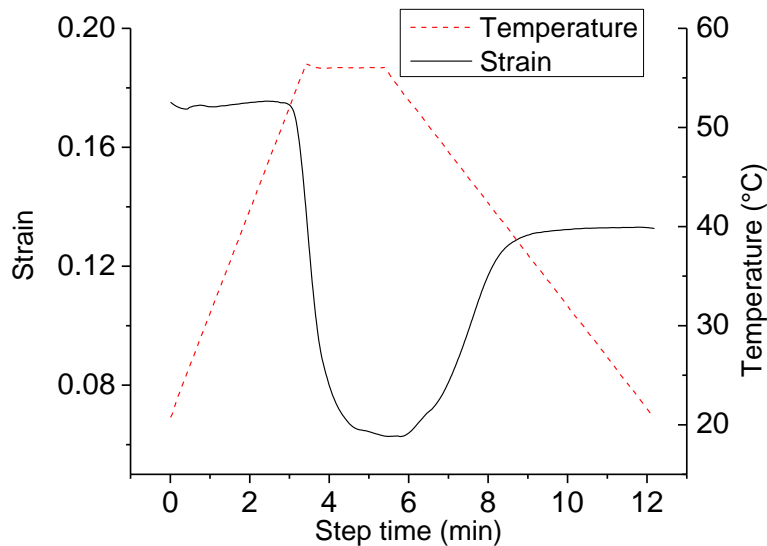
Figure 4.6 A dogbone bulk sample's maximum reversibility was characterized by DMA tensile test as 41%, where ε_p was defined as programmed strain and ε_r as recovered strain. Partial melting temperature Tp was near Tm = 56 °C. The temperature ramp has similar rate as the optical experimental set up: 1) Heat from 20 °C to 56 °C (10 °C/min); 2) Wait 2 min at 56 °C; 3) Cool from 54 °C to 20 °C (5 °C/min).

4.4.3 Theoretical Diffractive Intensity

Theoretical predictions can be determined from using classical grating equations and have been derived previously. Figure 4.8a-b shows the dynamic action that is expected to happen, the grating starting in its secondary shape (raised ridges) and then transitioning toward its primary shape with the ridges decreasing in height. As long as the SMP stays within the reversible temperature region, then the ridge height can be controlled. Theoretical calculations were performed to determine the best range of heights to be able to measure the greatest change
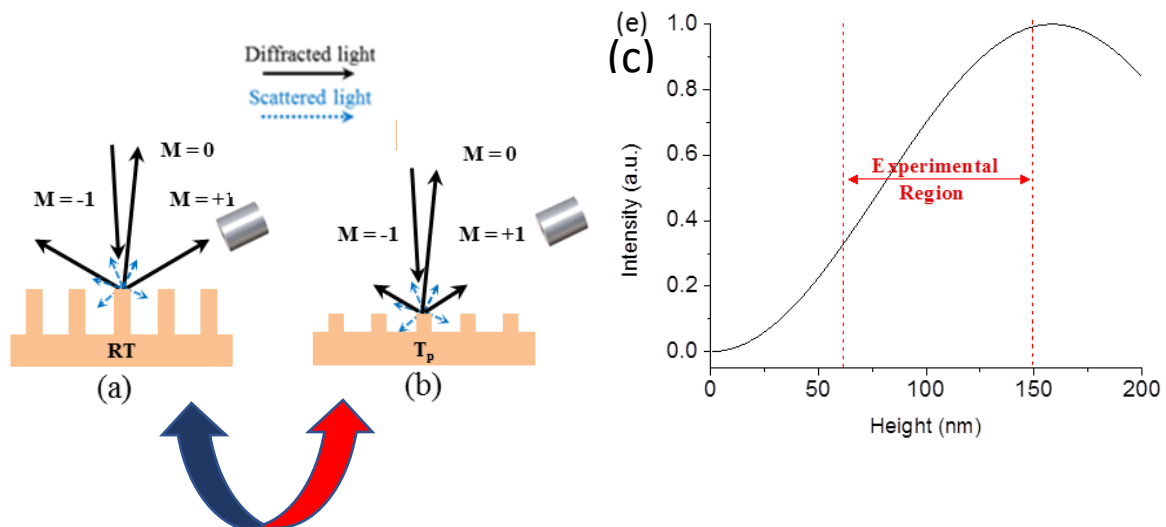
Figure 5.8 Theoretical expectation of the experimental results. (a) and (b) show the expected physical actuation. The secondary shape (a) is heated and the height decreases (b) as the SMP substrate will return to its primary shape (flat). After cooling the grating will return to its secondary shape (a). (c) Theoretical calculations for grating intensity indicate a sine-squared relationship between grating height and grating efficiency between 10 nm and 200 nm. As grating height decreases from ~150 nm to 60 nm, the measured intensity should decrease in a near linear fashion.

in diffraction intensity. For an ideal diffraction grating the intensity of the 0th order and 1st order diffraction modes can be calculated by equations (1) and (2).[19]

$$I_0 \propto \cos^2(2\pi\delta/\lambda) \qquad (1)$$

$$I_1 \propto \sin^2(2\pi\delta/\lambda) \qquad (2)$$

δ is the height of the grating, and λ is the wavelength of the laser beam. Figure 5.4b shows the relationship between grating height and 1st order diffraction efficiency. From a height of 50 nm to 150 nm the diffraction efficiency increase monotonically, which offers a wide experimental range to work in and provides a guide for interpreting the optical results. When the RSM grating is heated, it should begin to decrease in height, resulting in weaker 1st order diffraction intensity. During cooling the phase the SMP will recrystallize along the pathway dictated by the remaining crystallites and regain a portion of the original height.

4.4.4 Optical Reversibility

Figure 4.9 depicts the reversible change in diffraction intensity as the RSM grating is cycled through variation in substrate temperature (Figure 4.9a, Region 1). The grating is first heated to 42 °C, before reaching 40 °C there is minimal change in intensity. This result supports results found by Zhou et el, that indicated that the onset of shape recover occurs only after melting of at least ~10% wt/wt of the initial crystallinity.[1] Above 40 °C the intensity begins to decrease due to the onset of shapeshifting. As the substrate temperature is raised to 42 °C the

intensity continues to decrease. Upon cooling the intensity, slowly recovers toward its initial value at room temperature, indicating good optical reversibility. When this experiment is repeated at higher temperatures (52 °C and 56 °C) the observed intensity increases as well (Figure 4.9b). These experiments were performed multiple timed for each temperature, well only a single cycle is shown for clarity. Here it is shown that the maximum optical reversibility occurs at the same temperature as T_m. The optical reversibility, shown in Figure 4.9b is calculated using the following formula:

$$OR = \frac{I_{RT,end} - I_{T_p,partial\ melt}}{I_{RT,start}} \qquad (3)$$

Where $I_{RT,start}$ is the intensity of 1st order diffracted light by the RSM grating at room temperature before heating; $I_{T_p,partial\ melt}$ is the intensity of the diffracted light at a temperature of partial melting (T_p); $I_{RT,end}$ is the intensity after cooling back to room temperature.
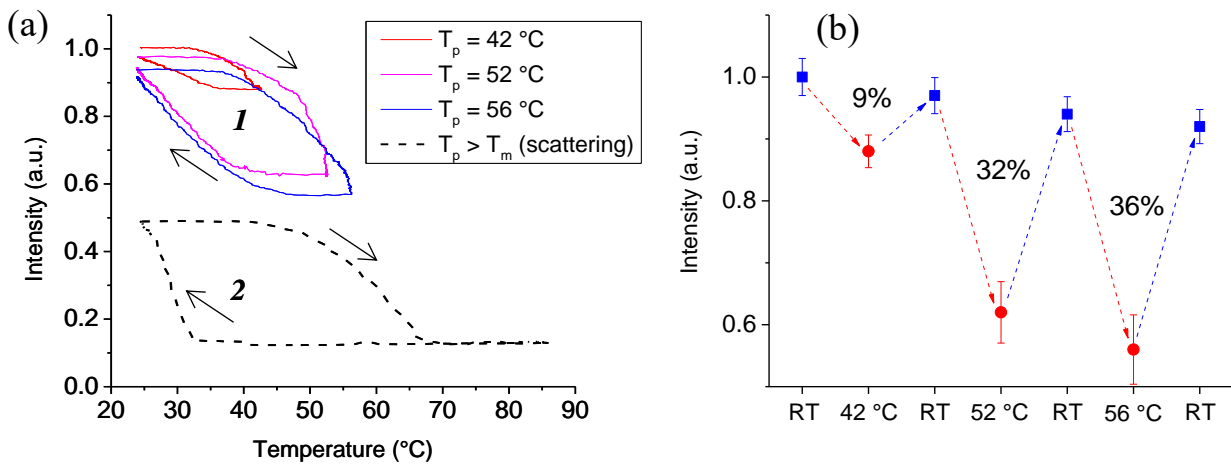
Figure 4.9 Optical modulation of a reversible SMP grating. a) Optical intensity of a diffraction spot as temperature was varied (arrows showing ramping direction). Region 1: Optical intensity can be reversibly controlled within different cycles with T_p kept below T_m. Region 2: When T_p is increased above T_m, the grating is greatly erased and non-recoverable. The intensity drops significantly as the temperature increases to T_f. Now the surface returns to its flat primary shape

and the intensity changes upon cycling are due to melting/crystallization-induced scattering. (b) Optical reversibility was calculated for three T_p cycles. A maximum optical reversibility of 36% was achieved when T_p was set at 56 °C, which is close to T_m.

When the RSM grating temperature is $T_p > T_m$, the behavior enters a new regime. The diffraction intensity decreases below Region 1 and enters the curve shown in Region 2. In this region a majority of the crystallites have melted, which allows the chemical network to relax to its thermodynamically preferred shape, dictated by the chemical crosslinks, thus causing the RSM to return to its flat, primary shape. The grating is now mostly destroyed and can no longer be recovered. On subsequent cycles the substrate temperature is raised to T = 85 °C. This is done in attempt to remove   any remaining gratings, eliminating its contribution to the detected light. As will be discussed in a later section, not all grating structures are destroyed, but small patches (less than 10 μm by 10 μm areas) of grating structure are scattered across the sample surface and will contribute little to the detected light when compared to the spot size (.5 cm) of the beam.

Although it appears that the optical response in Region 2 is comparable in intensity variation to Region 1, it is important to understand that these responses are due to completely different effects. In fact, the distribution of light changes dramatically between the two regions. On Region 2, the sample temperature has been raised above T_m, removing and polymer structures and resulting in a smooth flat surface. This surface reflects light in a specular fashion, which causes a majority of the reflected light to miss the detector, which is still positioned at the location of the 1st order diffraction spot. The sample is then cooled from its fully melted state, when T = 37 °C (T_c), the sample begins to randomly crystallize, without guidance from a shape memory scaffold. Random crystalline orientation causes a sharp increase in scattered light in all directions, essentially causing the sample surface to become optically rough. This is important

because now all incident light is undergoing scattering, whereas in region 1 light was undergoing

specular reflection, diffraction, and minimal scattering. Cartoon depictions of the two states with

in both regions is shown in Figure 4.10, the tall (Figure 4.10a) and short (Figure 4.10b) gratings

of region 1 with specular and diffracted light. With the smooth, flat substrate (Figure 4.10c) and

the optical rough substrate (Figure 4.10d) of region 2.
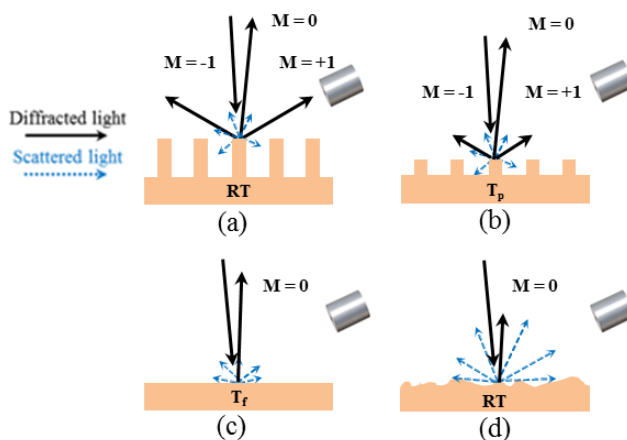
Figure 4.10 The diffraction and scattering intensity change with temperatures. The 1st diffraction
order was monitored as the grating was cooled to RT (a) and heated to a partial melting
temperature T_p (b). Length of arrow indicates relative intensity which relates with grating's
height. (c) At T_f the surface returns to optically flat, detector only picks up scattering signal and
when cooled back to RT (d), crystals form in an unrestricted fashion, resulting in an optically
rough surface that more readily scatters light.

4.4.5 Polymer Crystallization

The intensive scatting of region 2 is mainly due to the polymer crystallization yielding a

heterogeneous assembly of randomly oriented crystallites with a size distribution ranging from

10 to 1000 nm. Further testing indicated that the rough surface resulted in isotropic scattering,

with only small variances of 1-2%. This measurement has been proposed as an alternative

techniques to study crystallization induced surface roughness. [20]

4.4.6 Recovery of Intensity

The diffraction intensity never completely returns the original intensity. This is due to the physical shape not completely returning to the secondary programed shape due to the partial relaxation of the chemical networks during recrystallization after each heat-cool cycle. It has been shown that strained chemical networks tend to return to their equilibrium unperturbed state (the primary shape).[1,21] However, the natural trend of thermodynamic equilibration is reversed by the kinetics of biased recrystallization of the constrained network strands, which is biased by the remaining crystallites carrying the memory of the programmed secondary shape.

4.4.6 Separating scattering and diffraction

Although the high intensity scattered light of region 2 can be attributed to the random crystallization after the secondary shape has been erased, it highlights the need to separate the contribution of scattered light a diffracted light during shapeshifting. The RSM gratings often had a soft red glue while being measured, due to transmitted light being scattered by the crystallites in the bulk of the sample. To quantify this contribution an RSM grating was fabricated, but instead of a flat permanent shape, a grating mold was used to form a grating as the primary shape. The grating was fabricated by placing a PFPE grating on the bottom of No secondary shape was imbued on this sample. Instead the RSM grating was cycled through various temperature to determine the effect that melting and crystallization have on the scattering of light. Figure 4.7 illustrates the experiment, with the top curves showing the effect of melting when the diffraction spots are aligned with the detector and the lower intensity curves are when the grating has been rotated 90°.

When the diffraction spot is aligned with the detector we see minimal change in intensity until 53 °C. For 53 °C and especially once the sample reaches and surpasses T_m, a large increase in diffraction intensity occurs. This effect can be attributed to the melting of all the crystallites and the grating returning to a perfectly ordered primary shape. The efficiency of the grating if further enhanced by the optically smooth surface. Upon cooling the crystallization occurs and the diffraction returns to the same intensity. Since this effect is mainly seen above Tm, this would not contribute to the optical results in Figure 4.9, region 1. When the RSM grating is then tested again the grating is rotated 90° and the detector will now only measure scattered light. As can be seen in the lower curves of Figure 4.11, the intensity drops and a small modulation of ~10% is seen in for the scattered light at T_m

Therefore, the observed opticial reversibility, while a grating is present on the sample surface, can be attributed to the shape shifting of the grating and not the scattering from crystal melting and recrystallization.
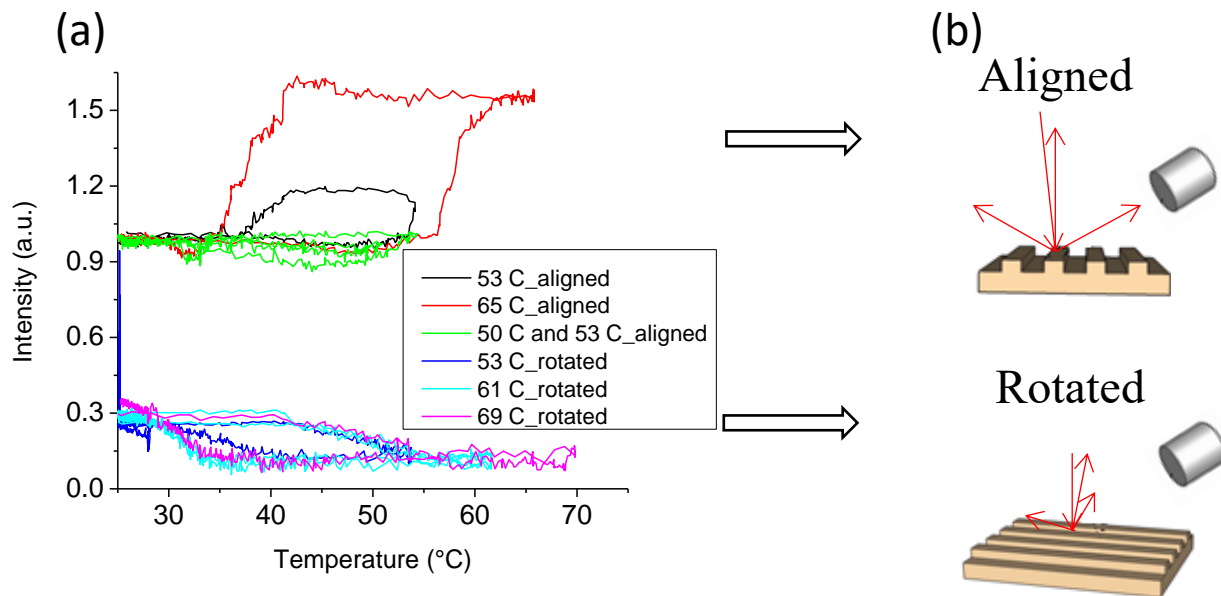
Figure 5.11 Optical measurements (a) of a permanent grating, with no programed secondary memory. When the 1st diffraction order is **(b)** aligned with the detector and the temperature is varied, the permanent grating undergoes an internal realignment as the crystals melt which smoothes the grating surface. This results in a more efficient grating, increasing the observed intensity. The permanent grating is then rotated 90° **(c)** and the detector only picks up scattered light as the grating is cycled. In this measurement the modulation in intensity is due to the crystallites melting and recrystallization during cycling.

4.4.7 Repeatability and Fatigue

In order for the optical application of shape memory polymers to be realistic, the optical results must be consistent from cycle to cycle and have minimal fatigue over many cycle. SMP fatigue has been reported on previously with some materials only able to withstand 20 cycles.[22] Typical experiments for this study included 2-3 cycles per temperature, with less than 5% variation in optical intensity. Further cycling at a single T_p resulted in a loss of ~10% of optical intensity over 25 cycles. A single grating run over hundreds of cycle showed an optical loss of ~25% but eventually settled into a repeatable cycle without further loss.

4.4.8 Physical reversibility

Variations in the surface topology of the RSM grating, were explored to further clarify the observed optical reversibility. Understanding process by which the shape changes for determine proper programing procedure. Three-way SMPs results have illustrated the importance of the programing procedure.[21] Stimulus triggered variations of the grating topography were analyzed *in situ* with the atomic force microscopy (AFM). Figure 5.8a-e show the AFM images during a standard cycling, with experimental conditions similar to the optical experiments. In order to determine maximum reversibility a similar procedure was followed as reported previously. The maximum reversibility was found to occur when the T_p was close to the melting peak T_m. Figure 5.8f shows the average topography of the grating at room temperature and close T_m. The grating was cycled several time to determine the robustness of the shape memory process at these scales. Figure 5.8e shows this cycling and indicates good repeatability.

AFM was able to confirm that the ridge height varied with temperature but all other geometric parameters remained constant. This shows that the optical response is isolated to the change in height of the grating. Height reversibility has been calculated using the follow formula:

$$HR = \frac{H_c - H_b}{H_a} \qquad (4)$$

Where H_c is the recovered height, H_b is the temporary height and H_a is the orginal height. The maximum height reversibility was determine to be 26%. The reversibility is significatly lower than than the bulk reversbility of 41% of a polymer fil subjected to 15% uniaxial strain deformation.
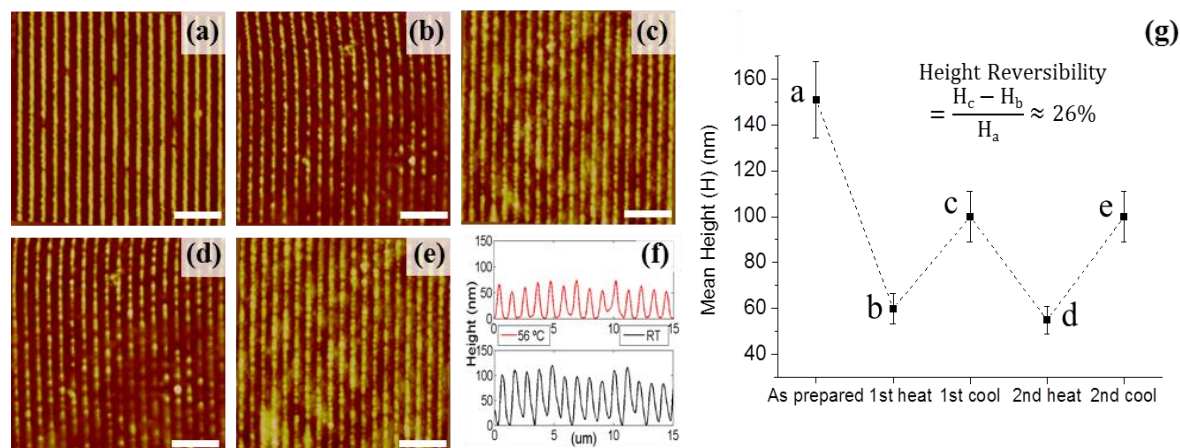
Figure 4.12 AFM images of (a) as prepared and at room temperature, (b) after heating to 56 °C at 1 °C/s and (c) after cooling back to room temperature. (d) Second heating to 56 °C at 1 °C/s (e) and after subsequent cooling back to room temperature. (all scale bars are 5 μm) (f) Height averaged line profile of the sample during one heating cycle, (top) at 56 °C and (bottom) cooled to RT. (g) The corresponding AFM mean ridge height was averaged over 180 line profiles per AFM image. The height reversibility is calculated using the mean heights of corresponding AFM images

4.4.9 Discrepancy between physical and optical reversibility

The discrepancy between the bulk and microscopic reversibility may be due to plastic deformation and crystallization. Figure 4.12 illustrates some remnants of the grating structure due to plastic deformation. Figure 4.12a illustrates that the small area of plastic deformation is found sporadic around the surface of the sample and would not have contributed significantly to the optical response after the grating has been erased. However, the plastic deformation can be attributed to the forces used to emboss the secondary shape. These forces may have been too large, resulting in the plastic deformation and potential limiting the reversibility and repeatability of the current sample.

Crystallization may have also played a role in limiting the physical reversibility. In has been shown previously by the Shieko et al. that freshly molten chains tend to recrystallize into large spherulites (~10um).[1]. This could potentially interfere with crystallization in the

nanoscale confinement of the grating structures and contribute to the non-flat surfaces after the

initial heating.
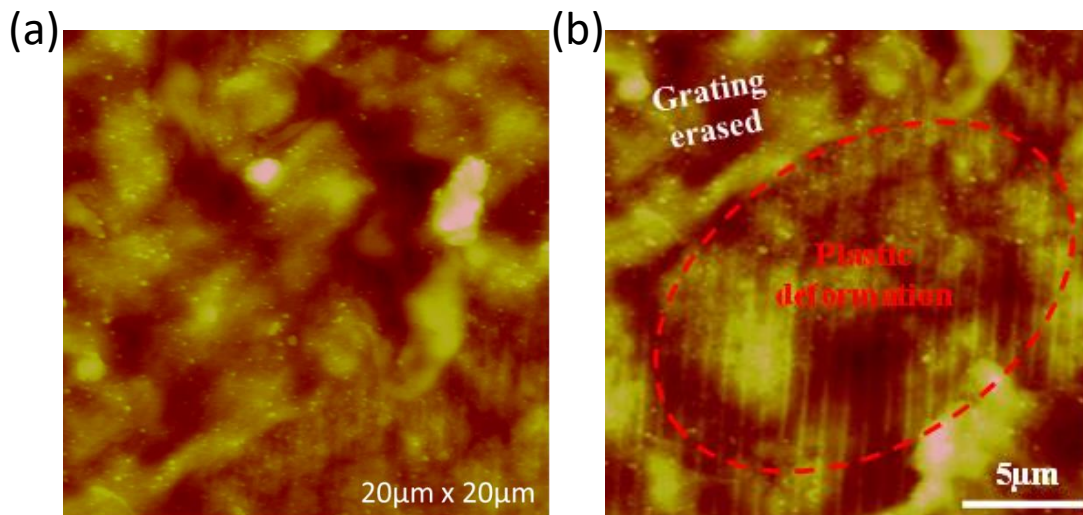
Figure 4.13 evidence of plastic deformation. An SMP piece was heated to 80°C, a complete melting temperature, then cooled back to RT. Most gratings structures were erased and surface returned to the original shape **(a)**, however a few spots turned out to remain grating structure due to plastic deformation **(b)**. The crystallization induced random roughness on the erased area was also observed.

4.5 Conclusion

In conclusion, a reversible shape memory optical grating has been demonstrated. POA, a

reversible shape memory polymer was able to precisely replicate and control sub-µm features. A

square grating was chosen for the proof of concept experiment, since only the height would be

actuated. Theoretical calculations showed that the diffraction efficiency of a square grating has a

near linear relationship to the height of the grating. Changes in grating height were determined

by monitoring the change in 1st order diffraction efficiency as the RSM grating was exposed to

multiple heat-cool cycles. Grating ridge height was actuated between multiple heights by adjusting the T_p of the substrate, within the range $T_p < T_m$. The optical response was shown to have two different regimes, the first region corresponding to the change in diffraction efficiency and the second related to the scattering of the erased substrate after T_m was surpassed. The optical reversibility of the grating's diffraction efficiency was shown to be as high as 39%. While the physical reversibility of the grating was shown to be only 26%. The discrepancy may be due to the formation of small spherulites during recrystallization. The AFM results provided further evidence that the mode in which the secondary shape is programed will be the route in which recrystallization occurs. From this study, a proper procedure for programing of photonic structures can be determined. Furthermore, these results lay the ground work for multifunctional SMP optical components.

REFERENCES

[1]   Zhou J, Turner S A, Brosnan S M, Li Q, Carrillo J Y, Nykypanchuk D, Gang O, Ashby V S, Dobrynin A V and Sheiko S S 2014 Shapeshifting: Reversible Shape Memory in Semicrystalline Elastomers ⊥

[2]   Biebuyck H, Larsen N, Delamarche E and Michel B 1997 Lithography beyond light: Microcontact printing with monolayer resists *IBM J. Res. Dev.* **41** 159–70

[3]   Li Z Y, Yin Y and Xia Y 2001 Optimization of elastomeric phase masks for near-field photolithography *Appl. Phys. Lett.* **78** 2431–3

[4]   Xu Q, Rioux R M and Whitesides G M 2007 Fabrication of complex metallic nanostructures by nanoskiving *ACS Nano* **1** 215–27

[5]   Xia Y, Kim E, Zhao X, Rogers J A, Prentiss M, Whitesides G M, Xia Y, Kim E, Zhao X, Rogers J A, Prentiss M and Whitesides G M 2017 Complex Optical Surfaces Formed by Replica Molding Against Elastomeric Masters Published by : American Association for the Advancement of Science Stable URL : http://www.jstor.org/stable/2889746 Complex Optical Surfaces Formed by Replica Molding Against E **273** 347–9

[6]   Lipomi D J, Martinez R V., Cademartiri L and Whitesides G M 2012 *Soft Lithographic Approaches to Nanofabrication* vol 7(Elsevier B.V.)

[7]   Rolland J P, Maynor B W, Euliss L E, Exner A E, Denison G M, Desimone J M and Nanobiomaterials S 2005 Direct Fabrication and Harvesting of Direct Fabrication and Harvesting of Monodisperse *J. Am. Chem. Soc.* **127** 10096–100

[8]   Tumbleston J R, Ko D-H, Lopez R and Samulski E T 2008 Characterizing Enhanced Performance of Nanopatterned Bulk Heterojunction Organic Photovoltaics *Nanoscale Photonic Cell Technol. Photovoltaics* **7047** 70470S–70470S–9

[9]   Hampton M J, Williams S S, Zhou Z, Nunes J, Ko D H, Templeton J L, Samulski E T and DeSimone J M 2008 The patterning of sub-500 nm inorganic oxide structures *Adv. Mater.* **20** 2667–73

[10]   DeSimone J M 2016 Co-opting Moore's law: Therapeutics, vaccines and interfacially active particles manufactured via PRINT® *J. Control. Release* **240** 541–3

[11]   Merkel T J, Jones S W, Herlihy K P, Kersey F R, Shields A R, Napier M, Luft J C, Wu H, Zamboni W C, Wang A Z, Bear J E and DeSimone J M 2011 Using mechanobiological mimicry of red blood cells to extend circulation times of hydrogel microparticles *Proc. Natl. Acad. Sci.* **108** 586–91

[12]   Schenck W, Ko D H and Samulski E 2011 Liquid crystal alignment on polymer line gratings *J. Appl. Phys.* **109** 1–5

[13]   Werber A and Zappe H 2005 Tunable microfluidic microlenses. *Appl. Opt.* **44** 3238–45

[14]   Truxal S C, Tung Y-C and Kurabayashi K 2007 A PDMS-on-Silicon Deformable Grating for Spectral Differentiation of Mixed Wavelength Signals *TRANSDUCERS 2007 - 2007 International Solid-State Sensors, Actuators and Microsystems Conference* (IEEE) pp

1087–90

[15]   Ouyang G, Wang K, Henriksen L, Akram M N and Chen X Y 2010 A novel tunable grating fabricated with viscoelastic polymer (PDMS) and conductive polymer (PEDOT) *Sensors Actuators A Phys.* **158** 313–9

[16]   Aschwanden M, Beck M and Stemmer a. 2007 Diffractive Transmission Grating Tuned by Dielectric Elastomer Actuator *IEEE Photonics Technol. Lett.* **19** 1090–2

[17]   Zhao Q, Qi H J and Xie T 2014 Recent progress in shape memory polymer: New behavior, enabling materials, and mechanistic understanding *Prog. Polym. Sci.* **49–50** 79–120

[18]   Xu H, Yu C, Wang S, Malyarchuk V, Xie T and Rogers J a. 2013 Deformable, Programmable, and Shape-Memorizing Micro-Optics *Adv. Funct. Mater.* **23** 3299–306

[19]   Chang C-L, Acharya G and Savran C a. 2007 In situ assembled diffraction grating for biomolecular detection *Appl. Phys. Lett.* **90** 233901

[20]   Tippets C a., Li Q, Fu Y, Donev E U, Zhou J, Turner S a., Jackson A-M S, Ashby V S, Sheiko S S and Lopez R 2015 Dynamic Optical Gratings Accessed by Reversible Shape Memory *ACS Appl. Mater. Interfaces* **7** 14288–93

[21]   Behl M, Razzaq M Y and Lendlein A 2010 Multifunctional shape-memory polymers. *Adv. Mater.* **22** 3388–410

[22]   Schmidt, C., Neuking, K., Eggeler G 2009 Functional Fatigue of Shape-Memory Polymers *MRS Proc.*

Chapter 5

Dynamic Optical Lens for Augmented Reality

5.1 Introduction

The vergence-accommodation conflict (VAC) presents an interesting challenge for developers of NEDs. The lack of accommodation cues for users of AR and VR system can lead to serious visual discomfort. One proposed solutions to this problem is the use of varifocal mirrors using deformable membranes [1], but to date varifocal AR systems have shown limited FOV and typically employ complicated optics.   In this chapter I will review my collaborative work with Henry Fuchs group at UNC to combine the idea of half silvered mirrors [2] with deformable membranes[3–5]. The use of a single dynamic lens and pneumatic actuation, allows for this approach to address the VAC and to increase the FOV. My contribution to the works lies solely the fabrication and implementation of the half-silvered membrane mirrors. I will focus this chapter on the fabrication and characterization of the membrane. However, this chapter would not be complete without briefly discussing the optical design and the perceptual experiment used to validate this prototype.   Information on the computation efforts can be found in the publication.[6]

5.2 Review of approaches to overcoming limitations in NEDs

Varifocal lens are one of several possible solutions to VAC.[1] Approaches to overcome come VAC include light field technologies [7,8], always-in-focus techniques[9,10], and varifocal techniques[11–13]. Each of these techniques addresses VAC but come with their own draw backs. Light field displays tend to be computationally intensive and limited in angular resolution. Always-in-focus can imitate accommodative cues by computational means, while also providing a large field-of-view (FOV) but are limited in angular resolution. Varifocal techniques provide high angular resolution and accommodative cues, but have only shown limited FOV.[11,12] Studies have shown that supporting accommodative cues through varifocal systems improves visual comfort[14] and use performance[12] while decreasing the required computational load.

5.3 Experimental methods

5.3.1 Optical Design

The goal of a varifocal see-through NED is to place a virtual image at a variable focal distance from a human subject's eyes. The optical design for a see-through NED shown in Figure 6.1. A display located above a user's eye is reflected from a deformable membrane mirror towards the user. Assuming a mechanism causing a uniform deflection of the membrane, the deformable membrane mirror approximates a spherical concave reflective surface.
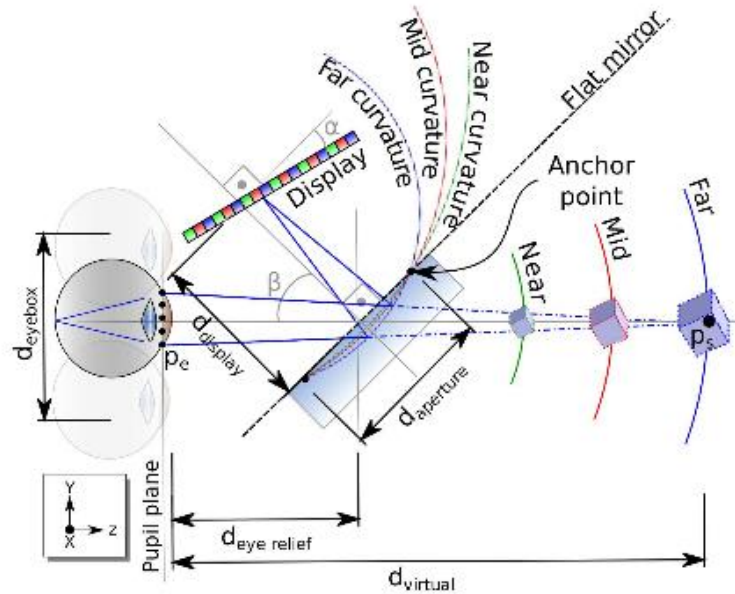
Figure 5.1 A sketch showing the varifocal optical layout with parameters for the single eye case. An image on a display above the user's eye reflects from our deformable membrane mirror toward the eye. A virtual image can be created at a desired position in space by varying the curvature of our deformable membrane mirror.

The design (Figure 5.1) starts by placing a flat membrane in front of an eye with a certain eye relief $d_{eye\ relief}$ and aperture sized $d_{aperture}$. The membrane is titled with an angle β around the X axis. The display is placed at a distance $d_{display}$ from the membrane, and tilt it with an angle α

Desired eye-box size, $d_{eye\ box}$, and $d_{aperture}$; $d_{eye\ relief}$; α; β; $d_{display}$ are parameters of our design. These parameters were used to simulate the FOV for various parameters.[6] The maximum FOV determined the parameters used for this prototype.

5.3.2 Membrane requirements and materials

In order to accomplish the optical design described in the previous section, the varifocal membrane must satisfy several requirements. The membrane must be transparent to all visible wavelength, distortion free, have low surface roughness to avoid scattering and freely transition between different shapes without undergoing plastic deformation. A transparent viscoelastic

92

polymer should satisfy each of these requirements. For this application, Polydimethylsiloxane (PDMS) was chosen because it is outstanding transparency in visible wavelengths, high elasticity, and excellent temperature stability and is easily accessible. Previous attempts included using a polyvinylidene chloride, however polyvinylidene chloride is susceptible to plastic deformation, which would be unacceptable for long term use.

5.3.3 Fabrication of membrane

Sylgard 184 PDMS kit was purchased from Dow Corning. Sylgard 184 is a two-part elastomer kit, with PDMS pre-polymer and a cross-linking agent. The prepolymer was mixed with cross-linking agent at a ratio of 10 : 1 and mixed vigorously for 3 minutes. The mixture was then degassed for 15 minutes, to remove bubbles incorporated during mixing. 6" Silicon wafers were purchased from University Wafers. The Wafer was silanized, to ease membrane release, by being placed in a desiccator, with 20 ul of trichloro (1H,1H,2H,2Hperfluorooctyl) silane and evacuated for 30 minutes and left under vacuum for 1 hour. Mixed and degassed PDMS prepolymer was spincast on the Si wafer for 1 min at 300 RPMs to obtain a PDMS membrane of approximately 240 um. The membrane is placed in an oven at 100 ˚C for 24 hours to produce a repeatable Young's modulus [37]. The membrane was then placed in a commercial physical vapor deposition unit (Kurt Lesker PVD 75) and a 20 nm Ag film is sputtered on the membrane. After metalization the film is carefully peeled and stretched taut across the vacuum housing to form the deformable membrane mirror.
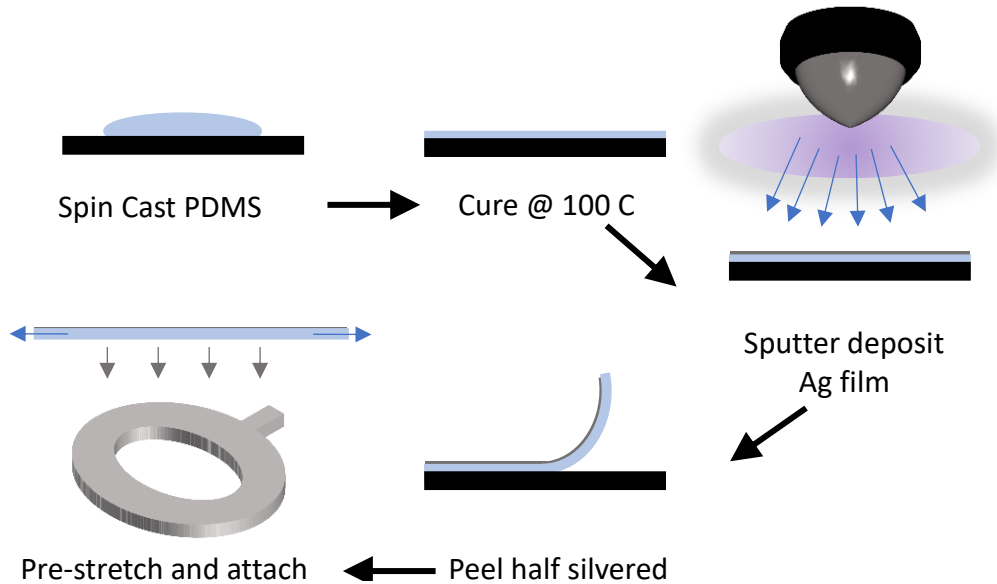
Figure 5.2 Membrane fabrication process. PDMS is first spin cast to 240 μm film and cured at 100 ˚C. Next, a 20nm Ag film is sputter deposited, and then the film is carefully peeled form the Si wafer. Before attaching to vacuum housing the membrane is stretched taut, to remove any stress induced diffraction. After attachment, the membrane is secured to the housing.

5.3.5 Housing Design

Vacuum tight housing was designed in house and 3D printed. Fused deposition modeling based 3d printing was proven to be inadequate in producing vacuum tight housings. For this project the housings were printed using a Formlabs 2 3D printer, which uses a stereolithographic technique with liquid photopolymer resins. To ensure a vacuum tight seal, gasket grooves were printed into the 3d housing, and custom gaskets were used to seal around the membrane and back enclosure.

5.3.6 Actuation method

Membrane shape was control by decreasing the air pressure behind the membrane using a vacuum pump. Pneumatic actuation allows for the deformed shape of the membrane to be

dictated by the shape of the aperture and the tension in the membrane. Individual membrane

shape (and thus focal distances) were controlled and maintained using solenoid valves.

5.4 Results and Discussion

5.4.1 Implementation
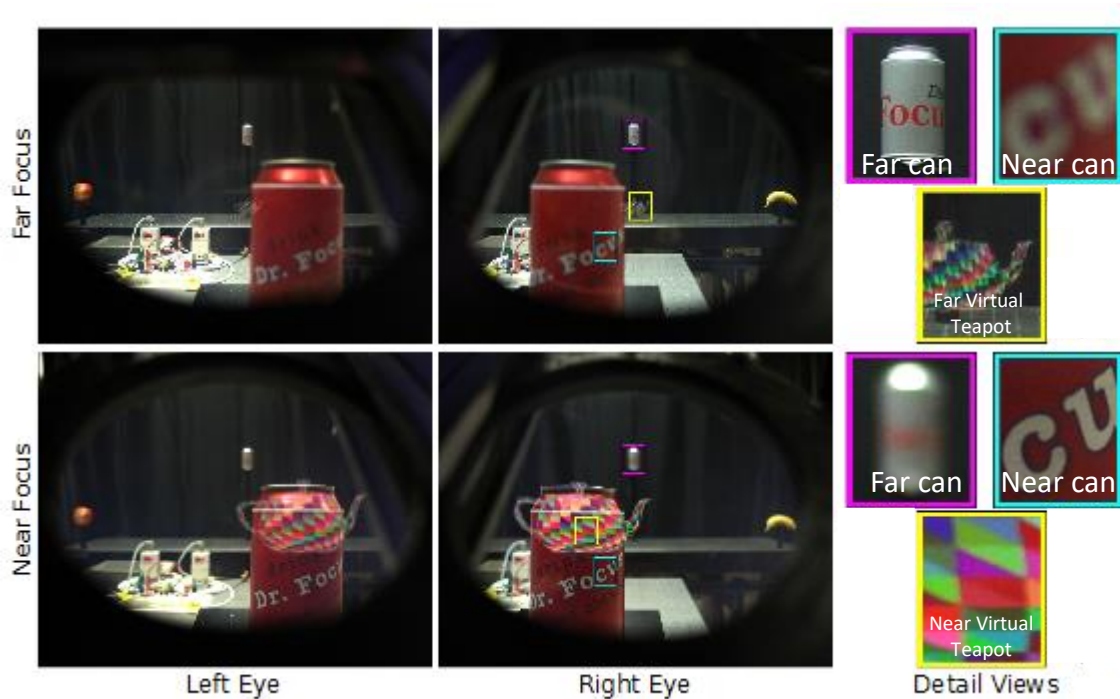
Figure 5.3 AR Implementation. Wide field of view augmented reality display showing virtual
teapot at far and near distance together with real objects, soda cans, at near and far. Photos
through display system left and right eyes with focus at far (top row), focus near (bottom row),
and overhead view (right) of the system. Details from right eye views showing focus of near and
far soda cans and virtual teapot (middle).

Demonstration of the dynamic membrane lens is shown in Figure 5.3. The top row

shows the membrane lens deformed to focus reflected light from the membrane at a far distance,

and the camera is focused at the far distance as well. As can be observed by the insets, the far

real world object is in focus and so is the virtual teapot. When the membrane is focused to a near

distance (25cm) the teapot comes into focus when the camera focus is adjusted to the appropriate

distance. The combination of pneumatic actuation and the mechanical properties of the membrane, resulted in an actuation time of 300ms. Video demonstration of the system can be seen at this link.

5.4.2 Effects of pre-stretching membrane

Pre-stretching of PDMS membranes is required due to surface rippling on the metalized surface after release form the Si substrate. The rippling is easily discernable as the ripples are periodic and cause diffraction, which is a result of stretching of the film when its being peeled from the Si substrate. When the film compresses again, the Ag thin film and PDMS interface will undergo a buckling transition in order to relieve stress.[15] To minimize elastic energy the Ag/PDMS surface will wrinkle into a periodic pattern.[15]
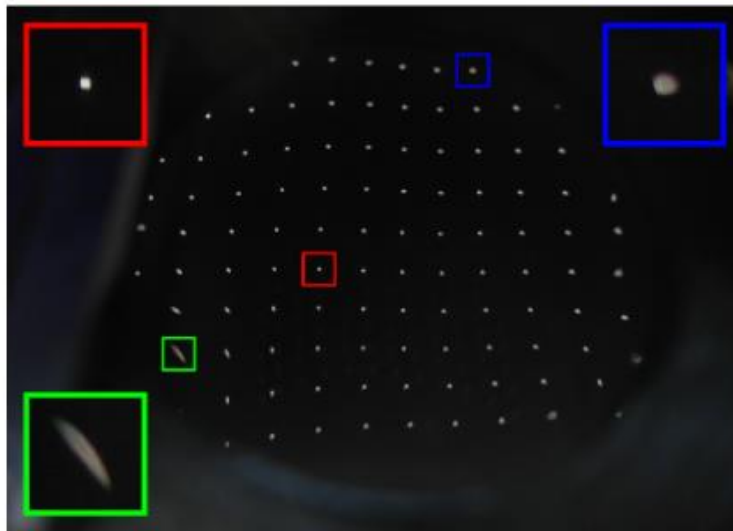
Figure 5.4 A view approximating the point spread function across the membrane. Squares of 3x3 pixels are illuminated in a grid pattern to show the degradation of focus across the membrane. Central region shows minimal point spread (red inset), while periphery shows a much larger point spread (blue inset). Severe defocus in lower left region (green inset) is caused by inadequate tension on membrane.

The resultant diffraction would interfere with viewing properties when used in the AR system. To overcome this the membrane is pre-stretched until no diffraction is visible and then placed on the vacuum housing. Although every effort is made to maintain a uniform stretch, additional stretching is typically required at the edges and results in non-uniform stress across the membrane. An example of this can be seen in Figure 5.4, here a focus test is performed to determine how well the focus is maintained across the membrane. If focus is consistent the spot size of the reflected light should remain unchanged. However, due to uneven pre-stretching of the membrane the spot size varies, and in some instances, are extremely out of focus.

The effect of prestretching becomes more obvious as the membrane changes shape. Shown in Figure 5.5 are black and white grids projected on to the membrane as the focal depth is changed. At each focal depth with grid is misshapened beyound what would be expected from a parabolic membrane, at one meter and beyound the distortion becomes large enough that only the central vertical region is usuable. Although this can typically be accounted for computationally, the pre-stretch induces a astigmatism in the membrane as its actuated, which forces the need for additional optics to account for the astigmatism.

| Flat membrane | 25cm focus | 1m focus |
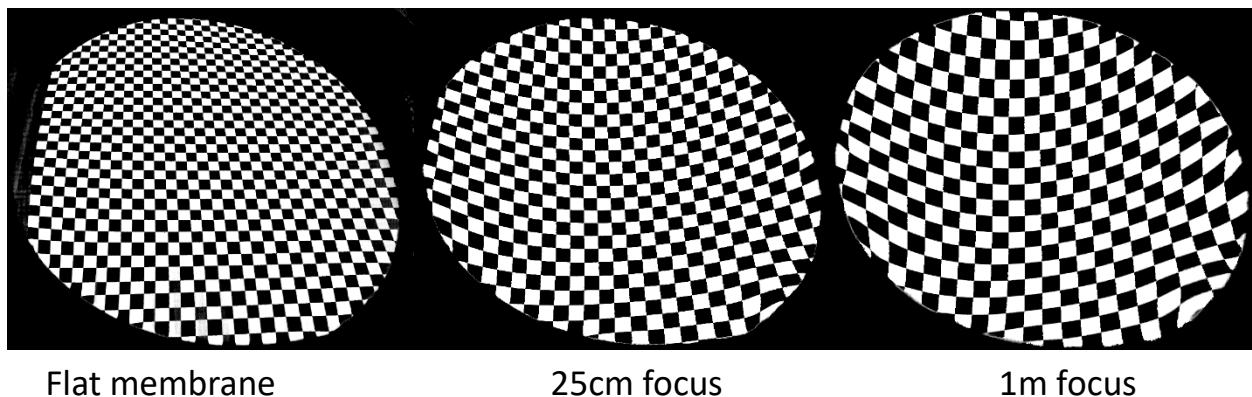
Figure 5.5 Black and white grid projection on to the membrane as the focal depth is changed. The flat membrane shows no focus distortion across the membrane. When the membrane is focused to 25cm the majority of the image remains undistorted except on the outer edges. When

focused at 1m the central region remains generally undistorted along the central vertical axis but major distortions appear

5.4.3 Wavelength dependent reflection

Deposition of a thin film of Ag onto the silver membrane increases the reflectance of the membrane and its 20nm thickness allows it to be more mechanically forgiving when deformed. However, thin films are subject to wavelength dependent reflection and transmission. Transmission and reflection spectra were measured using a J. A. Woollam variable angle spectroscopic ellipsometer. The deformable membrane mirror was aligned and the incident angle was set to 40 degrees to match β (housing angle) and α (incident angle form display) for both the transmission and reflection measurements. Shown in Figure 5.6 the reflection of the membrane changes by as much as 20% between 400 nm and 700 nm. The discrepancy can be slightly compensated for by adjusting the brightness of the red and green display pixels but will not eliminate this problem. Thin film simulations show that the variation in reflectance could be reduced to below 10% by depositing an Al thin film instead of Ag.
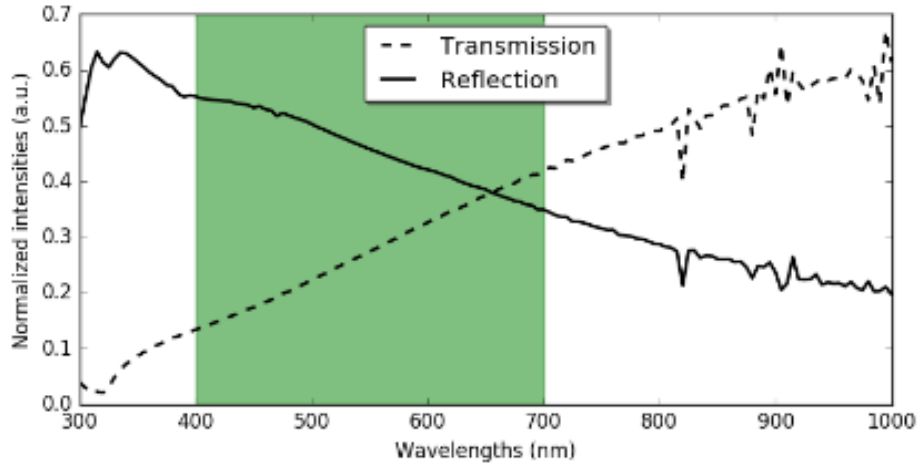
Figure 5.6 Reflectance and Transmission of coated membrane. The wavelength dependent transmission and reflection characteristics of the in-house manufactured deformable membrane. Green highlighted region corresponds to visible wavelengths.

5.4.4 Loss of resolution due to focal depth

During normal operation of the varifocal system, the membrane exhibited a loss of resolution for far focal depth (greater than 5m). The loss in resolvable pixels can be partially attributable to the stress induced astigmatism, while a majority can be attributed scattering. During pre-stretching the metal film cracks, then as the film is deformed islands break apart inducing scattering and decreasing resolution. A possible solution to the loss in resolution is to deposit the metal film after pre-stretching the film and securing it to the vacuum housing.

5.4.5 Membrane durability

As this prototype is proposed as a possible system for commercial application, the mechanical and optical durability of the PDMS membrane and Ag film were tested. For this test, the membrane was deformed 10x beyond normal operation and then allowed to return to flat. This test was repeated more than 25 thousand times. The optical results can be seen in Figure

5.7, with the numbers at the top left corner representing the number of iterative actuations that

have occurred. Before any actuation, the membrane reflects crisp images, after nearly 10

thousand actuations the reflection is slightly muddled by scattering but remains generally the

same. After 25 thousand actuations, the scattering becomes more prominent, and begins to

saturate the reflected image. The major distortions in the final image of Figure 5.7 are not a

mechanical failure but rather it is due to the membrane detaching from the housing. This test was

performed with an early prototype and was attach only with double sided tape.
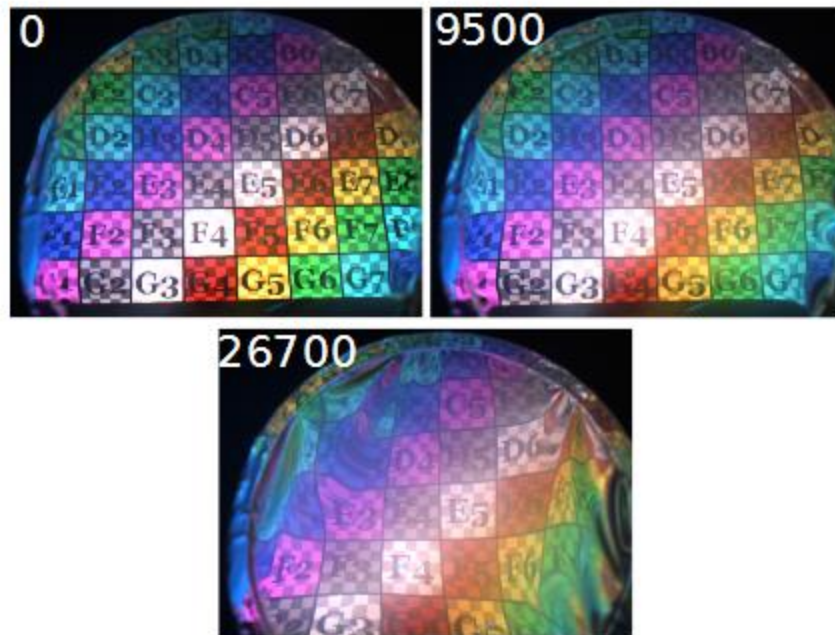
Figure 5.7 Photographs showing the result of the deformation test to estimate usability over lifetime for the in-house built deformable membrane mirror. The deformable membrane mirror was iteratively stretched back and forth with 10 times larger deformations than during normal operation. Each photograph shows a counter that represents number of iterations.

Further improvements in the housing and membrane attachment, resulted in the membrane being

more secure. Standard use of an AR system would require hundreds to thousands of focal

changes in a day and should be reliable for years. Well this test shows the reflection becoming distorted sometime between 10 and 25 thousand iterations, it was performed with extreme actuations conditions, it was able to demonstrate that the membrane and metal film are robust enough to remain usable for thousands of iterations. Further reliability test will be needed under normal operation.

5.4.6 Perception test results

In order to determine if this novel varifocal membrane approach would provide accommodative support and if users can benefit from it while performing monocular visual acuity tasks. A user study was performed on twelve subjects (20 to 34 years of age) that had normal or corrected-to-normal vision.

The stimulus for this test was a pair of white Landolt C shapes shown in Figure 5.8. The location of the gaps was either on the top or bottom side corresponding to the up and down orientation of the shape. The shapes were separated by 2 visual degrees, and each of them spanned 30 arcmin which imposes the gap size of 6 arcmin, where the normal 20/20 eye can resolve 1 arcmin. Since through the NED calibration its focus state has been precisely setup for each trial, the larger gap size was chosen so that the user response is immediate and effortless, as well as it is not affected by lower display contrast, limited spatial resolution, and possibly imperfect luminance adaptation with respect to the requirements of standard visual acuity test One shape was presented on one of two physical screens located at 0:25m and 5m from the viewer. The other Landolt shape was presented on our NED with a focal distance either matching the distance to the physical screen or a modified one to simulate a lack of a correct accommodation cue. The range of considered focal distance offsets was 0.2 to 5 diopters (1/focal

distance). For the screen located at 0:25 m, the virtual object was moved further from the observer, while for the screen located at 5:0 m, the virtual image was moved closer to the observer.
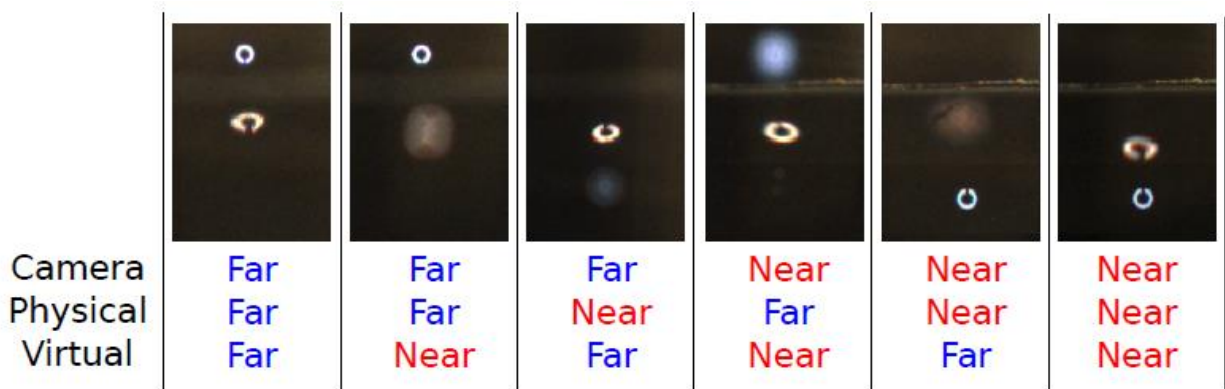
Figure 5.8 Series of photographs showing example stimulus as seen by a participant during the experiment. Labels below each photograph indicates focal state of our camera, physical location of the display, and the depth of the virtual image.

At each trial, a participant was asked to monocularly fixate at one of the physical screens. To this end, a simple math equation was displayed on the screen using a font of height 15 arcmin, while nothing was displayed on our NED. The user was asked to push one button if the equation was true and another if it was false. This math task was introduced to control the user fixation and give him enough time to correctly accommodate to the distance at which the physical screen was located. Immediately after responding, the stimulus appeared on the reference and the NED at a location central to the equation. The presentation time of the stimulus was set to 300 ms. The time was chosen such that it was just-enough to perform the visual acuity task, and it was determined during a pilot experiment. Next, the participant was presented with a blank screen and asked to press a button selecting whether the two patterns were of equal or different orientation. Afterwards, the study continued with a next trial. In total, two physical

displays and six focus distances for the NED were used in random order which after 20

repetitions gave the total of 240 trials per participant. Each participant took on average 30

minutes to complete the task.
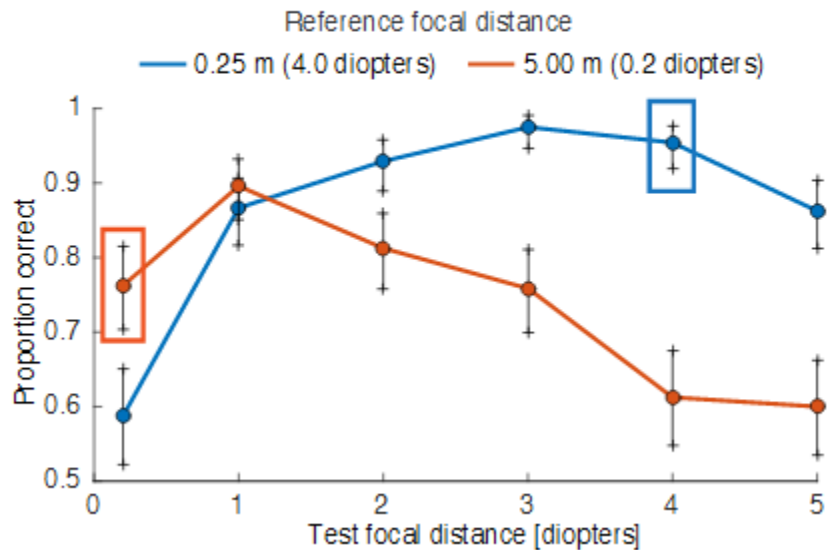
Figure 5.9 Perception test. The proportion correct as a function of test focal distance of the NED. Two points marked by rectangles are points where the reference and the test distances matched. For such conditions, the performance is expected to be the best. The error bars denote Clopper-Pearson binomial confidence intervals.

The graph in Figure 5.9 shows the relation of the NED focal distance and the proportion

of correct responses for each of the reference displays. Analysis shows differences between

different conditions and found a significance influence of the test focal distance on the

proportion correct for both 0.2 diopters and 4.0 diopters. In general, as the test focal distance

approached the reference depth, i.e., both stimuli were presented at the same focal distance, the

participants were able to correctly perform the task more often maxing out at 97.5% and 89.6%

for stimuli at 0.25m (4 diopters) and 5.0 m(0.2 diopters), respectively. The best performance

should be located at the points corresponding to the cases where the test and the references focal

distances match (see rectangles in Figure 5.9). This can be observed well for the closer physical display. For the further screen, the drop of the performance for the focal condition can be explained by a degradation of the image quality due to a strong membrane distortion compensation required for such an extreme focus depth. This made the comparison of relatively small shapes difficult. Except for this particular case, the trend in the measured data follows the expectation, i.e., the participant performance drops with increasing optical focus difference between both displays. For the reference display at 0. 25m distance (4 diopters, blue) and our NED set up to focus at 1.00m (1 diopter) participants had to compare two shapes at focal distances differing by 3.0 diopters and had a mean performance of 86.7%. As the analysis shows, this is a significant drop from the optimal performance when the focus for NED matches the physical screen. Similar observations can be made for the reference display at distance of 5.00m (0.2 diopters, red), where the performance significantly drops to 75.8% for the NED focused at 0.33m (3 diopters) when compared to the case of focusing it at 1.0m (1 diopters). Situations like these occur while using current AR displays with fixed focus distance. From these results, we conclude that the varifocal properties of our device allow improving the user performance in tasks that require simultaneous observation of the virtual and the real worlds,

5.5 Conclusion

For high quality AR experiences, it is critical that AR systems are cable of reproducing all visual cue across the visual field. Accommodative cues are the most challenging to reproduce. To this end, a novel varifocal system was proposed, and an elastomeric membrane was designed and developed to reproduces the accommodative cues. The PDMS membrane with Ag coating showed good mechanical and optical qualities, which were robust enough to with stand everyday use. The system was tested and users showed a significant increase in

104

accommodative performance. Further development is necessary to reduce the effects of internal stress on the membrane and cracking of the reflective film.

REFRENCES

[1]   Kramida G and Varshney A 2015 Resolving the Vergence-Accommodation Conflict in Head Mounted Displays *IEEE Trans. Vis. Comput. Graph.* **22** 1–16

[2]   Kiyokawa K 2007 A wide field-of-view head mounted projective display using hyperbolic half-silvered mirrors *2007 6th IEEE ACM Int. Symp. Mix. Augment. Reality, ISMAR* 2–5

[3]   McKay S, Mair G, Mason S and Revie K 2000 Membrane-Mirrorbased Autostereoscopic Display for Teleoperation and Telepresence Applications *Stereosc. Displays Virtual Real. Syst. VII* **3957** 198–207

[4]   Mckay S, Mairb L S, Waddella P and Frasera S M 1999 MEMBRANE MIRROR BASED DISPLAY FOR VIEWING 2D AND 3D IMAGES **3634** 144–55

[5]   Rawson E G 1969 Vibrating varifocal mirrors for 3-D imaging *IEEE Spectr.* **6** 37–43

[6]   Dunn D, Tippets C, Torell K, Kellnhofer P, Aksit K, Didyk P, Myszkowski K, Luebke D and Fuchs H 2017 Wide Field Of View Varifocal Near-Eye Display Using See-Through Deformable Membrane Mirrors *IEEE Trans. Vis. Comput. Graph.*

[7]   Stereoscope L F, Chen K and Wetzstein G 2001 Light Field Stereoscope

[8]   Lanman D and Luebke D 2013 Near-eye light field displays *ACM SIGGRAPH 2013 Emerg. Technol. - SIGGRAPH '13* **32** 1–1

[9]   Akşit K, Kautz J and Luebke D 2015 Slim near-eye display using pinhole aperture arrays *Appl. Opt.* **54** 3422

[10]   Maimone A, Lanman D, Rathinavel K, Keller K, Luebke D and Fuchs H 2014 Pinlight displays: wide field of view augmented reality eyeglasses using defocused point light sources *ACM Trans. Graph.* **33** 89:1----89:11

[11]   Liu S, Cheng D and Hua H 2008 An optical see-through head mounted display with addressable focal planes *Proc. - 7th IEEE Int. Symp. Mix. Augment. Real. 2008, ISMAR 2008* 33–42

[12]   Konrad R, Cooper E A and Wetzstein G 2016 Novel Optical Configurations for Virtual Reality: Evaluating User Preference and Performance with Focus-tunable and Monovision Near-eye Displays *Proc. 2016 CHI Conf. Hum. Factors Comput. Syst.* 1211–20

[13]   P. V. Johnson, J. A. Parnell, J. Kim, M. S. Banks G D L 2016 Assessing visual discomfort using dynamic lens and monovision display *3D Image Acquis. Disp. Technol. Percept. Appl.* pages TT4A–1

[14]   Johnson P V, Parnell J A Q, Kim J, Saunter C D, Love G D and Banks M S 2016
        Dynamic lens and monovision 3D displays to improve viewer comfort *Opt. Express* **24**
        11808–27

[15]   Schweikart A, Horn A, Böker A and Fery A 2009 Controlled Wrinkling as a Novel
        Method for the Fabrication of Patterned Surfaces pp 75–99

Chapter 6

Conclusion

6.1 Thesis Contribution

This dissertation investigated the applicability of soft polymers in various optical applications, by exploiting polymeric properties I was able to show fabrication methods and systems with increased functionality, that are inaccessible without the use of soft polymers. PFPE, a low surface energy polymer, was used to fabricate complex nanostructures similar to those found on the surface of the Morpho butterfly. The optical response was measured and compared to the natural butterfly and showed the ability to mimic the angular response of the natural nanostructure, through controlled fabrication of randomized nanostructures Then I described two cases in which polymers were used to create multifunctional adaptive optics, where the shape of the optical element was controlled, and thus so was the optical response. I showed the use of shape active optical elements with shape memory optical gratings and varifocal membranes. These projects show that optical structures can be used to manipulate structure on a wide range of length scales, with various applications.

6.2 Looking Forward

6.2.1 Biomimetic Structures

Biomimicry of complex nanostructures capable of reproducing similar optical effects seen in nature continues to be of interest to researcher. Use of innovative technologies has shown to be able to access these structures. Using 3D DWL has been shown to produce similar structures to the blue tarantula. As these technologies advance, wide area fabrication may be possible. Applications using the nanostructure of the Morpho butterfly have shown promise in producing sensitive sensors and security labels. The potential still remains for these have an impact on the technologies in their respective fields. In order for this to happen more focus needs to be placed on incorporating randomness into Morpho-like structures when developing new fabrication routes. As has been shown in this dissertation, without the various modes of randomness the structures will never respond optically in a similar fashion to their biological models.

6.2.2 Shape active gratings

Production of a shape active optical elements remains an intriguing idea. However, the main road block for their realization is further improvement in the polymer attributes. For SMPs polymer fatigue must be addressed when developing new polymers or else these can never become applicable to standard systems.

Investigation into the optical response into more complex photonic shapes needs to be explored. For example, RSM blazed gratings would be immediately applicable, if the blaze angle could be actively tuned. For more complex shapes a broader understanding of how the shape memory polymer is transitioning at these scales is need to interpret the optical response.

6.2.3 Varifocal membranes mirror

Varifocal see through membrane mirrors are far from the only proposed solution to VAC but it is among the most mechanically simple approaches. Use of a vacuum system for actuation, is obviously incompatible with a headset for everyday use. Development of compact actuation system is needed to transition the current prototype to a head mounted system,

Beyond engineering and computer programing, there still remains several interesting materials science questions that need to be resolved. In order to improve angular resolution, a lens capable of different amounts of stretching along the lens, needs to be developed. Through gradual change in membrane thickness or Young's modulus. For both the current membrane design and any future designs detailed shape analyses as the membrane switches will be needed to further optimize the membrane.

Development of the reflective film, is needed to overcome the wavelength dependence of the current film. Wavelength dependence can be reduced to 10% over the visible region by incorporating an Al in place of Ag. Color neutral reflection will decrease the constraints on the computational side of the system.

6.2.4 Moon Shot

Each of the projects presented in this dissertation contributed to the ultimate goal of fabricating of a flexible shapeshifting biomimetic butterfly nanostructure. Determining a suitable fabrication route to create biomimetic structures that can optically imitate the Morpho butterfly. Understanding of how nanostructures shift when an external stimulus is applied and dynamic actuation over large areas, set forth the building blocks to this new structure.

Fabrication of an elastomeric soft polymer ultrastructure would allow for total control of the optical response. When such a structure is actuated, the spacing between "branches" would increase or decrease and elicit a change in the color of reflected light. Such structures would have wide application, from dynamic structural color displays to dynamically colored clothing. Dynamic clothing could be used for military camouflage that is able to actively tune to its surrounding and would be inherently responsive to the ambient lighting
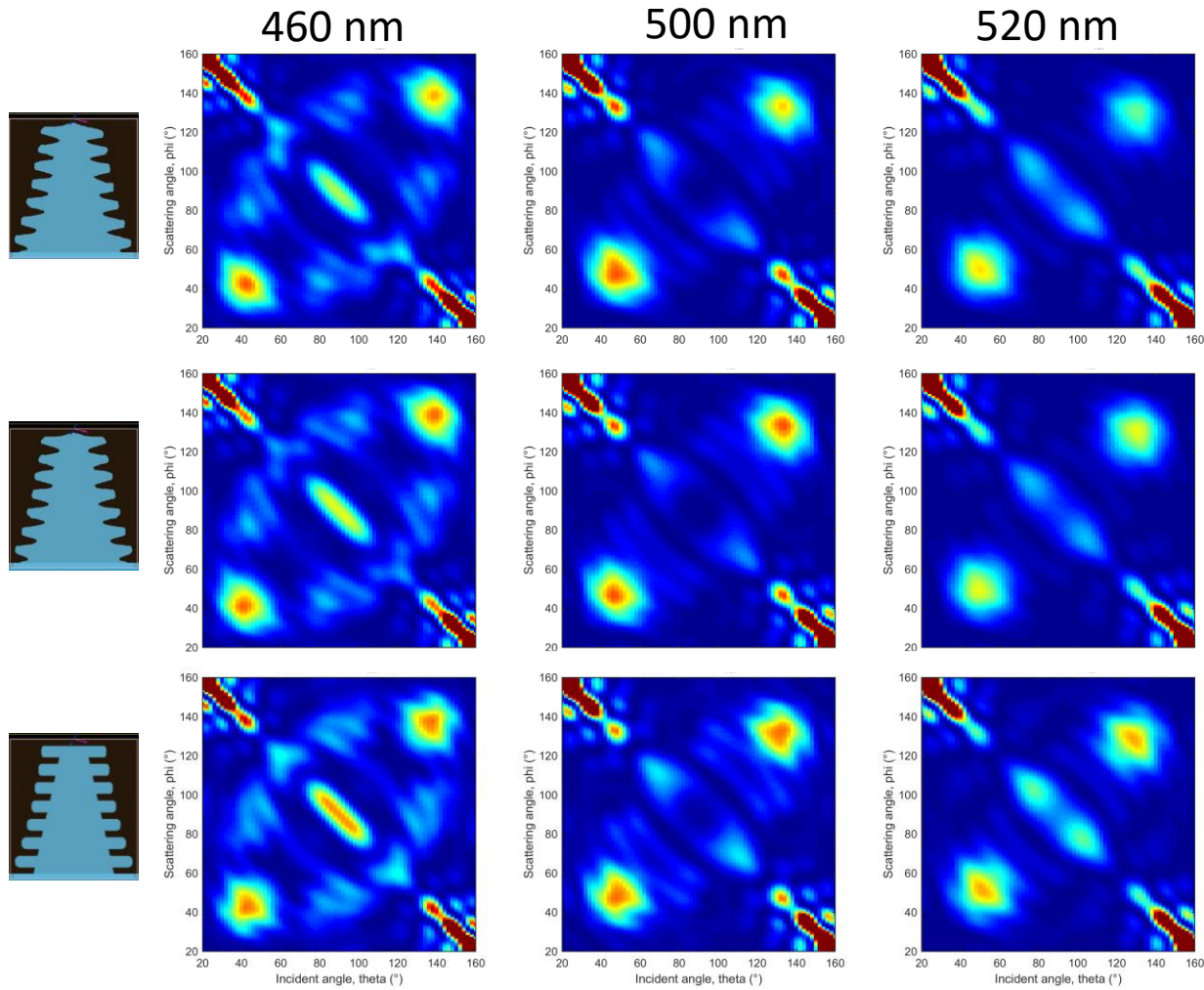
Figure A1 Full Simulation branch shape. (a) the nanostructure found on the surface of the uniformly distributed samples. The theta-phi graph matches the experimental result. (b) A symmetrized structure, (c) A straight branch model. θ-φ plots for wavelength 460 nm, 500 nm 520 nm.
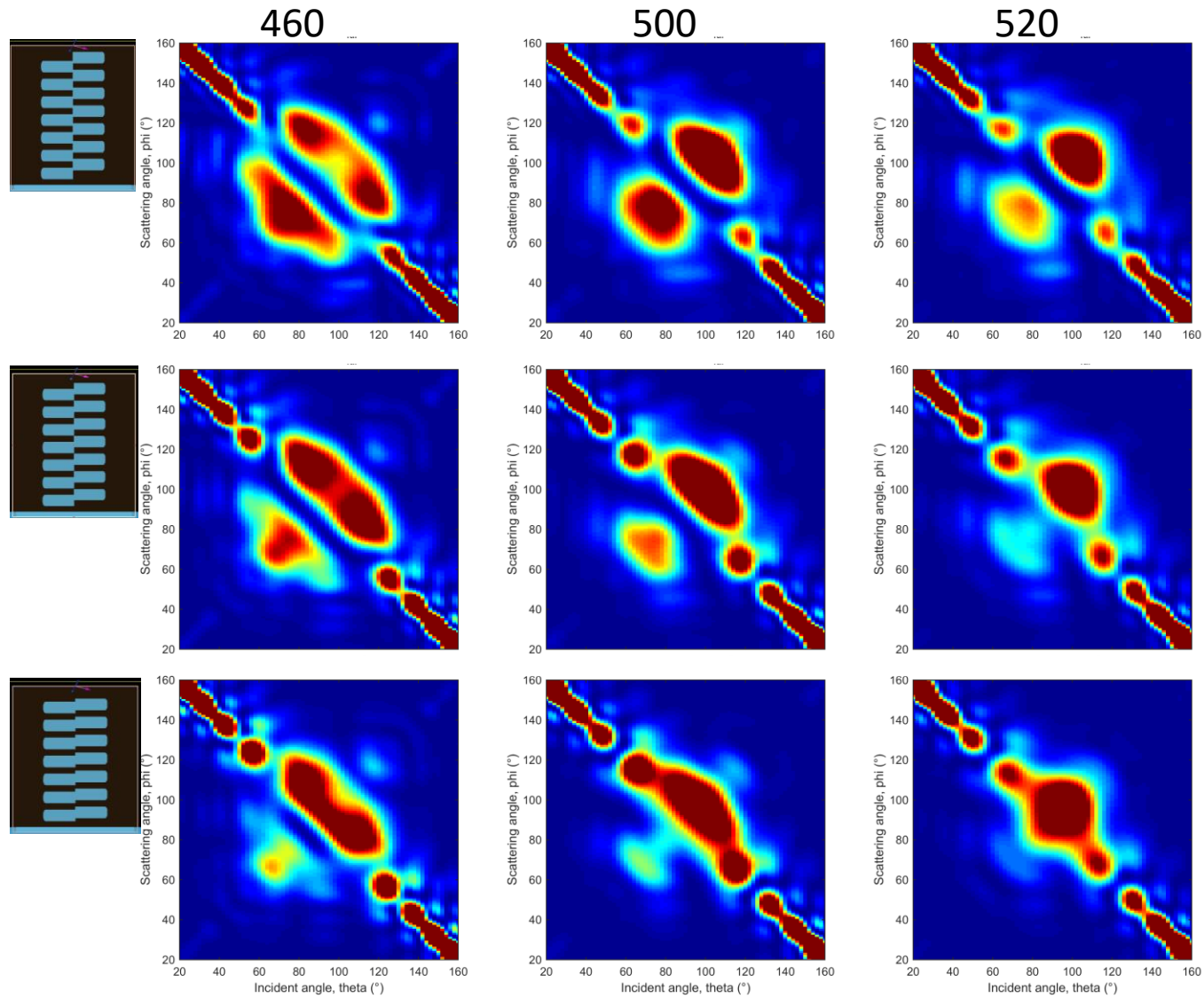
Figure A2 Full FDTD simulations comparing the effect of offset branches. The branch offset is gradually increased from no offset (a) to 50 nm (b), 75 nm (c) and 100 nm (d). . θ-ϕ plots for wavelength 460 nm, 500 nm 520 nm are
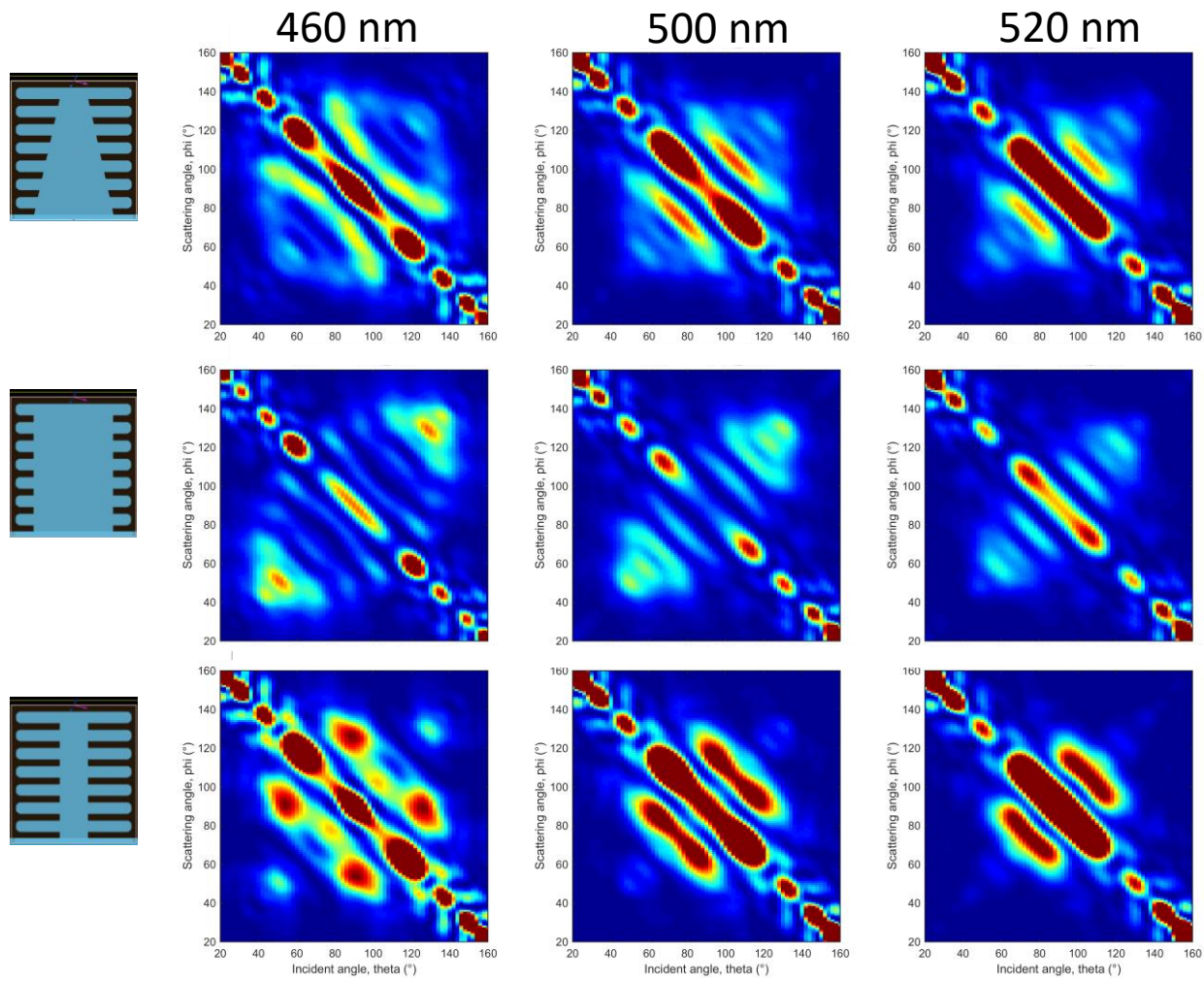
Figure A3 Full FDTD simulation exploring the effect of trunk shape and thickness. (a) Tapered trunk(b) fat trunk (c) thin trunk. θ-ϕ plots for wavelength 460 nm, 500 nm 520 nm.
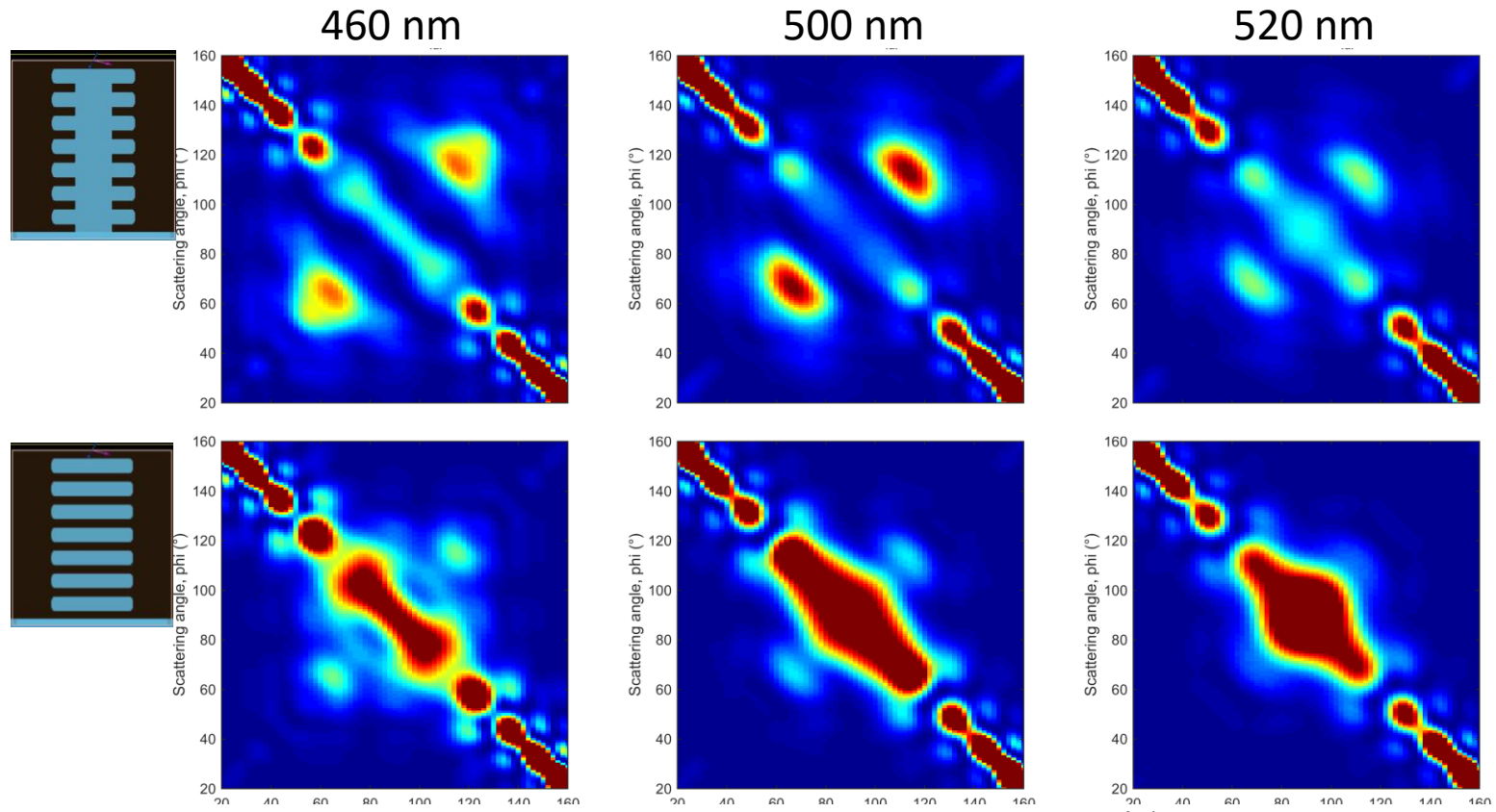
Figure A4 Full FDTD simulation showing the effects of having a trunk verses a multilayer. θ-ϕ plots for wavelength 460 nm, 500 nm 520 nm.